Title

Engineering the Intracellular Micro- and Nano-environment via Magnetic Nanoparticles

Author

Tseng, Peter

Publication Date

2012

University of California

Los Angeles

Engineering the Intracellular Micro- and Nano-environment via Magnetic Nanoparticles

A dissertation submitted in partial satisfaction of the
requirements for the degree Doctor of Philosophy
in Electrical Engineering

by

Peter Tseng

2012

Abstract of the Dissertation

Engineering the Intracellular Micro- and Nano-environment via Magnetic Nanoparticles

by

Peter Tseng

Doctor of Philosophy in Electrical Engineering
University of California, Los Angeles, 2012
Professor Jack W. Judy, Chair

Single cells, despite being the base unit of living organisms, possess a high degree of hierarchical structure and functional compartmentalization. This complexity exists for good reason: cells must respond efficiently and effectively to its surrounding environment by differentiating, moving, interacting, and more in order to survive or inhabit its role in the larger biological system. At the core of these responses is cellular decision-making. Cells process cues internally and externally from the environment and effect intracellular asymmetry in biochemistry and structure in order to carry out the proper biological responses.

Functionalized magnetic particles have shown to be a powerful tool in interacting with biological matter, through either cell or biomolecule sorting, and the activation of biological processes. This dissertation reports on techniques utilizing manipulated magnetic nanoparticles (internalized by cells) to spatially and temporally localize intracellular cues, and examines the resulting asymmetry in biological processes generated by our methods. We first examine patterned micromagnetic elements as a simple strategy of rapidly manipulating magnetic nanoparticles throughout the intracellular space. Silicon or silicon dioxide substrates form the base for electroplated NiFe rods, which are repeated at varying size and pitch. A planarizing resin, initially SU-8, is used as the substrate layer for cellular adhesion. We demonstrate that through the manipulations of a simple external magnet, these micro-fabricated substrates can mediate rapid (under 2 s) and precise (submicron), reversible translation of magnetic nanoparticles through cellular space. Seeding cells on substrates composed of these elements allows simultaneous control of ensembles of nanoparticles over thousands of cells at a time. We believe such substrates could form the basis of magnetically based tools for the activation of biological matter.

We further utilize these strategies to generate user-controllable (time-varying and localizable), massively parallel forces on arrays of cells mediated by coalesced ensembles of magnetic nanoparticles. The above process is simplified and adapted for single cell analysis by precisely aligning fibronectin patterned cells to a single flanking micromagnet. The cells are loaded with magnetic-fluorescent nanoparticles, which are then localized to uniform positions at the internal edge of the cell membrane over huge arrays of cells using large external fields, allowing us to conduct composed studies on cellular response to force. By applying forces approaching the yield tension (5 nN/μm) of single cells, we are able to generate highly coordinated responses in cellular behavior. We discover that increasing tension generates highly directed, PAK-dependent leading-edge type filopodia that increase in intensity with rising tension. In addition, we find that our generated forces can simulate cues created during cellular mitosis, as we are consistently able to generate significant (45 to 90 degree) biasing of the metaphase plate during cell division. Large sample size and rapid sample generation also allow us to analyze cells at an unprecedented rate–a single sample can simultaneously stimulate thousands of cells for high statistical accuracy in measurements.

We believe these approaches have potential not just as a tool to study single-cell response, but as a means of cell control, potentially through modifying cell movement, division, or differentiation. More generally, once approaches to release nanoparticles from endosomes are implemented, the technique provides a platform to dynamically apply a range of localized stimuli arbitrarily within cells. Through the bioconjugation of proteins, nucleic acids, small molecules, or whole organelles a broad range of questions should be accessible concerning molecular localization and its importance in cell function.

The dissertation of Peter Tseng is approved.

Robert Candler

Ayogdan Ozcan

Dino Di Carlo

Jack W. Judy, Committee Chair

University of California, Los Angeles
2012

To my family

Table of Contents

LIST OF FIGURES

List of Tables

ACKNOWLEDGMENTS

First and foremost, I would like to thank my family for their endless emotional and financial support during my graduate studies. I would not have been able to pursue my research dreams without their gracious support.

I am hugely indebted to Professor Jack Judy, who gave me a position in his lab, and provided endless technical support through all the ups and downs of our initial magnetic switch project, and ultimately allowing me to pursue my pie-in-the-sky research vision.

Of course, this project is a long way from the microfabricated MEMS switches of my master's work. Along the way a bevy of people were there to provide support in this work. The members of Judylab: Ira Goldberg, who gave great advice on the limitations and capabilities of the fields and forces of magnetic micromagnets; Brian Matthews and Joe Zendejas, who acted as Mr. Fixits for random project troubles, and Hyowon Lee, whose support during the begining of the project had a huge influence on both me and my research.

I thank the members of Di Carlo Lab, for letting me take up space and add to the entropy of the lab. Special thanks to Westbrook Weaver for helpful discussions on the biological side of this project.

Finally, I thank Professor Dino Di Carlo, who took in a student without a home for his research, gave our project his full financial support in a time when money wasn't as free flowing as it is now, and guided it to where it is today. What was initially a mass of ideas without form and function has been fleshed out to project that it is now, and one that has produced results and images of which we can all be immensely proud of.

Vita

1983	Born, San Jose, California, USA.
2005	B.S. Electrical Engineering, University of California, Berkeley.
2007	Teaching Assistant, Electrical Engineering Department, UCLA. Taught sections of EE150/EE250, Microfabrication.
2008	M.S. Electrical Engineering, University of California, Los Angeles.

Publications

Glickman, M., Tseng, P., Harrison, J., Niblock, T., Goldberg, I. B., and Judy, J. W. High-performance lateral-actuating magnetic MEMS switch. Journal of Microelectromechanical Systems 20, 842-851 (2011).

Tseng, P., Judy, J. W., and Di Carlo, D. Method and device for dynamic modification of localised cellular environments. US Provisional Patent no.61/360,400, 2011

Tseng, P., Di Carlo, D., and Judy, J. W. Rapid and dynamic intracellular patterning of cell-internalized magnetic fluorescent nanoparticles. Nano Letters 9, 3053-3059 (2009).

Tseng, P., Di Carlo, D., and Judy, J. W. Intracellular Patterning of Internalized Magnetic Fluorescent Nanoparticles," presented at EMBC conference 2009, Minneapolis, Minnesota.

Glickman, M., Peter Tseng, P., et al., CMOS compatible Back-end process for In-plane actuating ferromagnetic MEMS," presented at Transducers 2009, Denver, Co.

Tseng, P., Towards a CMOS compatible micromagnetic switch," Master's Thesis, University of California, Los Angeles.

Tseng, P., Judy, J. W., and Di Carlo, D. "Microfabricated Substrates for the Remote Generation of Precision Forces on Single Cells via Intracellular Magnetic Fluorescent Nanoparticles," presented at Hilton Head 2010, Hilton Head, SC.

Glickman, M., Harrison, J., Niblock, T., Goldberg, I., Tseng, P., and Judy, J.W. "High Permeability Permalloy for MEMS," presented at Hilton Head 2010, Hilton Head, SC.

Tseng, P., Judy, J. W., and Di Carlo, D. "Massively Parallel, High Force Interrogation of Single Cell Mechanics via Localized Magnetic Nanoparticles," presented at Microtas 2010, Groningen, Netherlands.

CHAPTER 1

Introduction

The single cell forms the base unit of many biological systems, and is fundamentally comprised of a complex network of organelles, biomolecules, lipid membranes, protein channels, and more, each fine tuned to work in harmony with one another to accomplish an inordinate number of intricate tasks at high efficiency. While there is base organizational, and relatively robust general biochemical knowledge for chemical pathways and biomolecule content, significant details of cellular function remain as of yet unknown. In particular the effect of localization of chemical signaling and mechanical perturbation on cellular development and decisions are relatively unknown and has been difficult to explore. Localization appears particularly important in cell behavior given the re-use of signaling molecules for different signals within cells.

The importance of localization is fundamentally rooted in cellular decision making. Cells process cues internally and externally from the environment and effect intracellular asymmetry in biochemistry and structure in order to carry out the proper biological responses, such as movement, differentiation, morphogenesis, division, and more. Understanding and controlling these localized intra and extracellular cues could not only further our understanding of the ways cells parse and interpret their surroundings to form a decision, but could also give us a tangible method of controlling cellular response.

Recent development in micro and nanotechnologies has taken large steps in attempting to develop tools to interface with single cells. Electrical probes comprising patch clamps, electrode probes, and nanotube / nanoneedles [1, 2, 3, 4, 5], are able to stimulate cells through locally applied electrical fields and current. Electric field and light-based mechanical manipulation (dielectrophoresis, laser trapping, etc) rely on the inherent dielectric differences between individual particles and its surroundings to generate forces [6, 7, 8, 9, 10]. Magnetic manipulation typically comprises of the tagging biomolecules to a magnetically active particle, which can then be selectively manipulated by permanent magnets or electromagnets [11, 12, 13, 14, 15, 16, 17, 18, 19].

While the electrical and chemical probing techniques have been feasibly integrated with standard biological probe setups and microfluidic environments, the ability to selectively modify the chemical or mechanical environment with nanoscale precision is lacking. Arguably, this encompasses the most interesting possibilities for single cell interrogation, as active spatial control of chemical and mechanical signals remains of active interest in cell biology and to more quantitatively probe cellular behavior.

1.1 Cell Interfacing

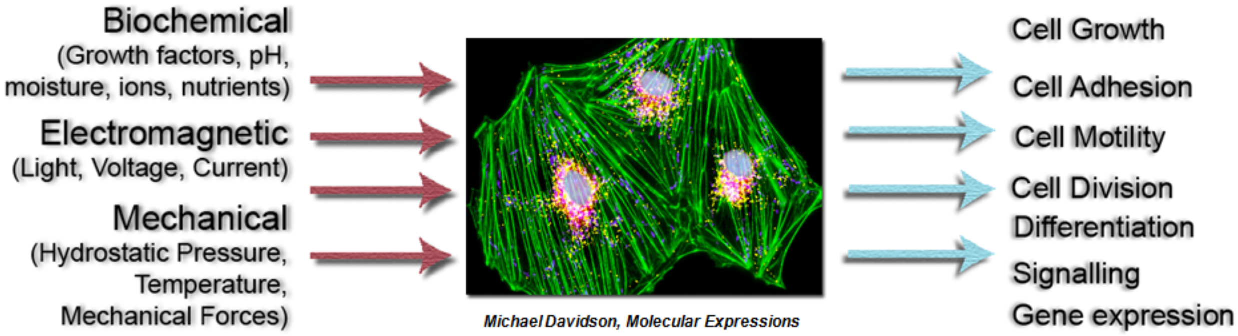

Figure 1.1: Biological systems, in very simplistic terms, take in a variety of inputs (from the chemical to the physical), and generate a variety of outputs in terms of response. Single cell interfaces are engineered tools that attempt to operate on this input-output system in order to effect cellular response.

Engineers have envisioned many inclusive systems to probe living cells. The ideal is to operate on the input-output stream of cellular systems [20, 21]. Various cues (mechanical, biochemical, light, etc), generate different cellular responses (growth, differentiation, movement, expression, etc). By engineering tools to simulate these stimuli, it is hoped to be able to both better understand, and conceivably control cellular behavior. Ultimately, the single cell could be flanked by a multitude of engineered surfaces and devices to interact with the single cell environment (Figure 1.2). Nanoneedles would continuously feed the cells desired chemicals, while fibrous carpets would supply chemicals, and patch clamps would control channels. Rarely included, however, are means of mechanical manipulation of particles, as the field is underdeveloped, and many of such methods are difficult to integrate on single chips, or simply do not possess the desired resolution. There also remains a dearth of methods to activate and probe cellular function at the nanoscale, important for understanding the temporal or spatial aspects of single cell machinery. Included here is a short, general review of common probing and activation methods in microtechnologies.

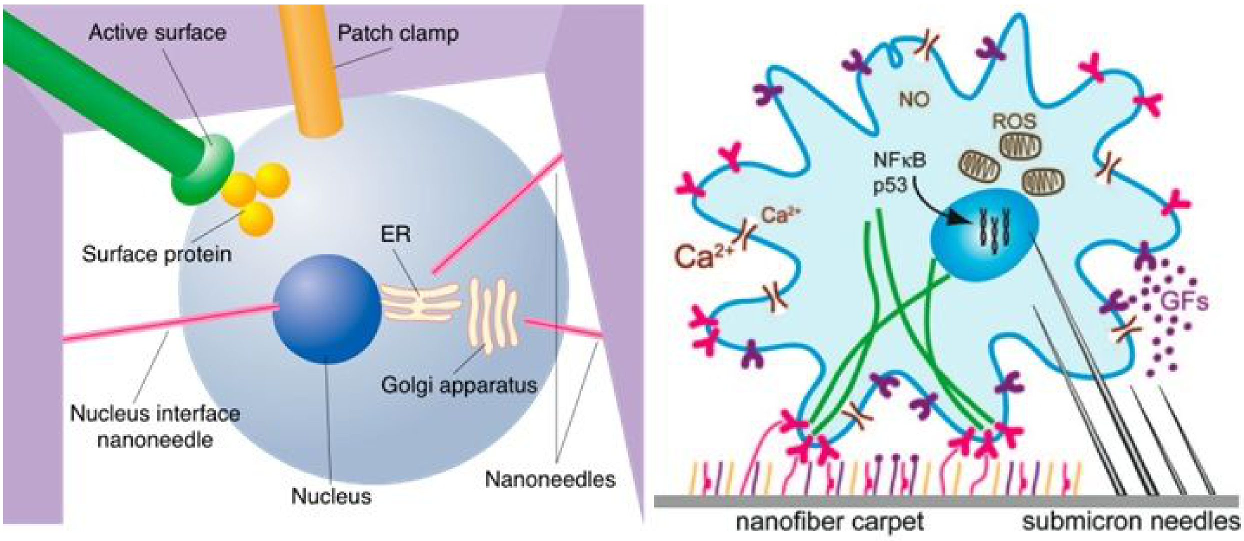

Figure 1.2: Envisioned, integrated subsystems for single cell analysis are typically comprised of nanoneedles, patch clamps, and biologically active surfaces that flank the cell to generate controlled cellular activity and record responses [20, 21].

1.1.1 Voltaic Probes

Traditional voltage probes operate on the action potential of neurons, muscle, or endocrine cells to either excite or probe cellular response. Generated voltages operate on specific voltages-gated ion channels to effect a variety of cellular responses, for example the transfer of impulses in neuronal tissue, the contraction of muscles, or the release of biochemicals. These probes have further been expanded to include those that measure the ionic response of ion-channels.

1.1.1.1 Wire-based Electrical Stimulation

Wire-based electrical probes are among the very first objects used to interface with single cells, having been initially discovered by Luigi Galvani more than two centuries ago when he stimulated the contraction of frog muscles with electricity. In more modern terms, these consist primarly of lines of wire and use electric fields and applied current to activate cell activity. These are used to stimulate either 2 dimensional networks of cells or skin (surface electrodes), or integrated with needles for implantation into into living tissues, whether muscle or nervous tissue. These devices are typically brute force and operates on cell action potentials, and there is little specificity beyond generating activity at single cell resolution. Recent research in nanotechnology utilize nanotubes and nanowires. Due to their thin size and biocompatibility, these devices are anticipated as low physical impact interfaces between cells and electrical probes for application of electrical stimulus. Their prevalence, however, is relatively limited, and direct use with cells is under development as control over nanomaterials (size, location, orientaton) is still under active research [3, 4, 5].

1.1.1.2 Patch Clamps

Patch clamping systems have been under research by both academic and commercial institutions for well over a decade (itself, the technique has been known for three decades), and gives users a method of measuring the potential and current through single or multiple channels. The base technique consists of applying a flanking micropipette and electrodes(or in more modern settings, flanking microfabricated orifices and transmission lines), and forming a seal around a portion of the cell. This sealed area is isolated, and thus can then be probed by the electrode. Isolating single channels can give experimentalists direct knowledge of transfering specific ionic-exchange occuring during cellular process. While this technique is still in common use, the quality of the result is heavily dependent on the patch clamp seal, and the specificity of the channel control is dependent purely on the physical location of the clamp and the cell [1, 2].

1.1.2 Engineered Biochemical and Environmental Interfacing

Biochemical approaches are a rather broad descriptor to encompass engineered interfaces for local application of analyte.

1.1.2.1 Nanoneedles

Similar to carbon nanotubes or metallic nanowires, nanoneedles are believed to be a low impact approach for delivery of analyte either directly into cells, or locally in the cellular environment (Figure 1.3). These have been used to perform micro-scale "operation," and the delivery of analyte such as DNA. These typically exist as either a "bed" above a substrate, or are integrated with AFM tips which can direct the location of the needle and apply the penetrating force required [22, 23, 24, 25]. Examples of nanoneedle concepts are shown in Figure 1.3.

1.1.2.2 Scaffold-based Interfaces

Creating 3-dimensional scaffolding for cellular systems allows engineers to better replicate the in-vivo environment of single cells. The most popular of these, including hydrogels / matrigels, have been under active research as a means of controlling cellular environment through their temporal and spatial modification. Degradation of local matrix via chemical, pH, or light means can be used to either mechanically modulate cellular environment or release drugs into biological systems [26, 27, 28, 29, 30, 31, 32].

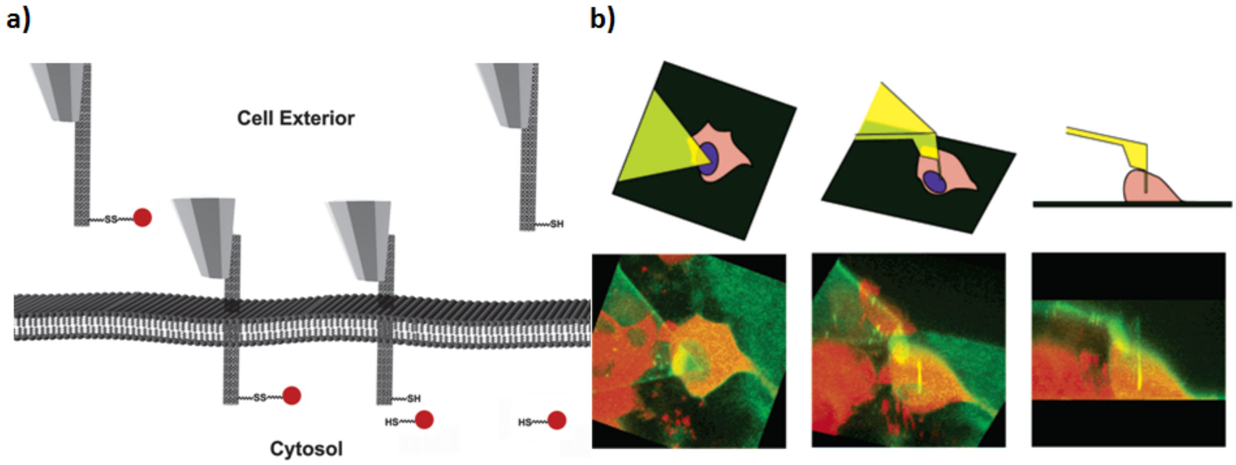

Figure 1.3: Varying executions of the nano-needle concept: a) Disulfide bonds stabilized on needles are broken upon entrance into the celliular environment. Cargo is delivered by chemical means. b) Nanoneedle operation on a single cell showing confocal microscopy of a penetrated sample [25, 22].

1.1.2.3 Genetic Engineering

The direct modification of proteins of interest by genetic modification is commonly used by biologists to study and modify localized cell response. Fusion proteins have been created that re-localize proteins to other locations based on the fused proteins binding partner. For example, the kinase, PI3K was localized to membranes by fusion with a peptide sequence that is normally post-translationally modified with the fatty acid myristic acid. Gene knockouts are the most common, in which proteins are completely delocalized from any location within a cell. These techniques have been successful in beginning to understand the role of biomolecule localization in cell function. Limitations of current techniques include: (1) technical difficulty of conducting experiments, (2) a limited number of proteins that can be knocked out, modified, or made photoactivatable, and (3) limits on the absolute location control to only predefined locations (specified by fused binding partners) or no locations (knockouts) [33].

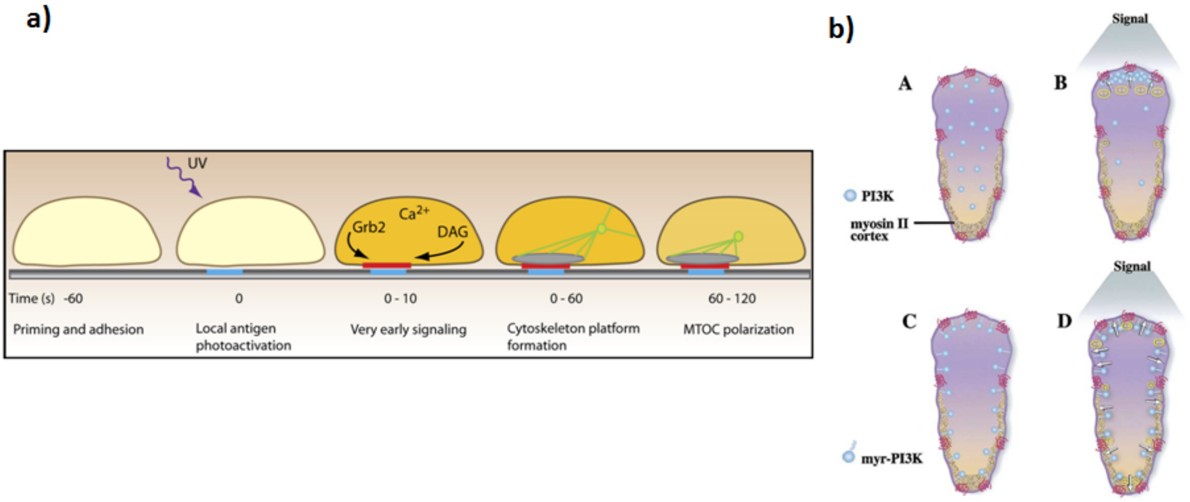

Figure 1.4: a) Light from an exterior source shines on a substrate and activates antigen formation. b) PI3K localized by protein fusion enforces localization points in the cell [26, 33].

1.1.3 Mechanical Manipulation

While the previous section refers to quantifying and applying voltages and current, this section refers primarly to using electromagnetic fields as a means of physical manipulation, where energy from fields are translated into mechanical motion rather than electrical.

1.1.3.1 Fluidic Shear

Applying a fluid flow to cellular systems is among the simplest methods of generating a mechanical stimulus, and is commonly used by biologists. These methods have been used in conjunction with knock-out and inhibition experiments to indentify mechanotransductive components, such as focal adhesion kinase, integrins, RAC, and PAK [34, 35, 36]. The technique is not particularly directed, as all cells experience the same stimulus, and the shear operates over entire cells (Figure 1.5). This approach is thus used for broader, multicellular experiments.

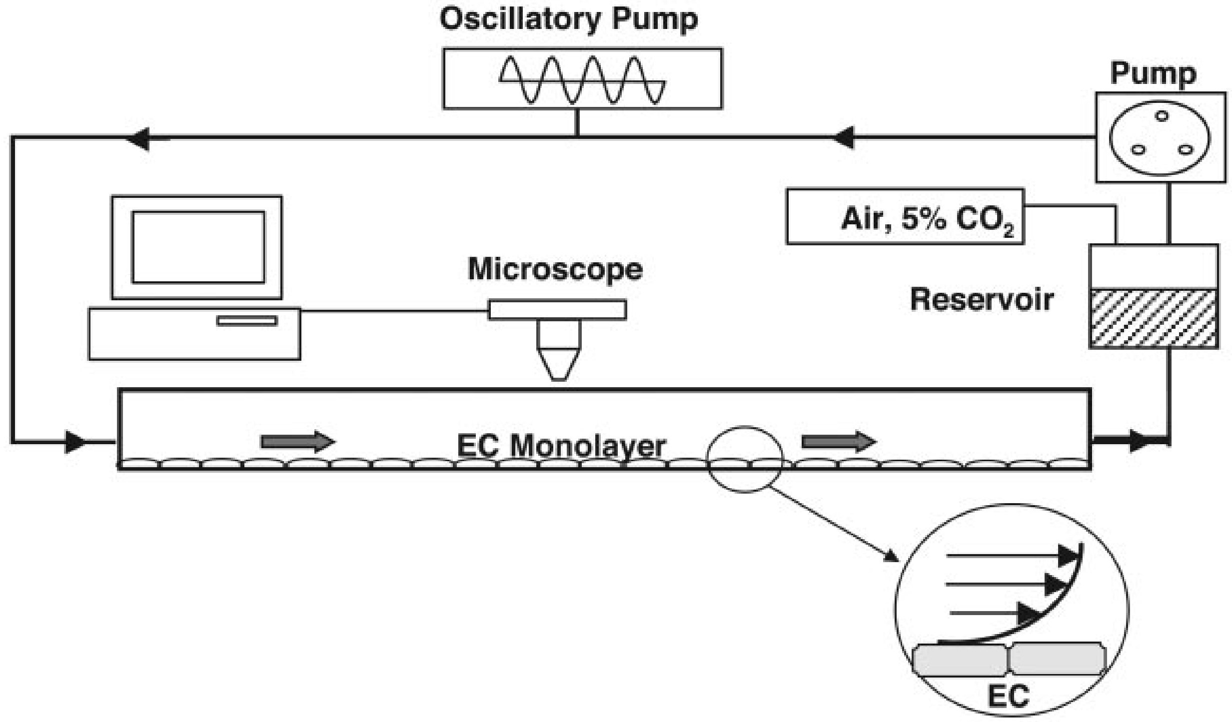

Figure 1.5: A pump forms a closed loop around a cellular substrate, applying a constant stimulus to the biological material [35].

1.1.3.2 Polymer Stretching

Similar in vein to fluidic methods, cell stretching is a broad approach to generally apply diffuse force over a large number of cells. The primary approach of this method is the ability to time-vary stimulus, and as such, experimentalists commonly use this technique to determine the response of biological systems to cyclical deformations [37, 38, 39, 40]. In addition, due to the high integretability of this method with long-term studies, these substrate types have been used to stimulate the differentiation of stem cells.

1.1.3.3 Electro / Dielectrophoresis

Electrophoretic methods rely on the inherent electrical polarizability and its subtle differences between materials to apply differing forces. These forces are generated by electric field gradients that ultimately drive particles one place to another. While these devices are

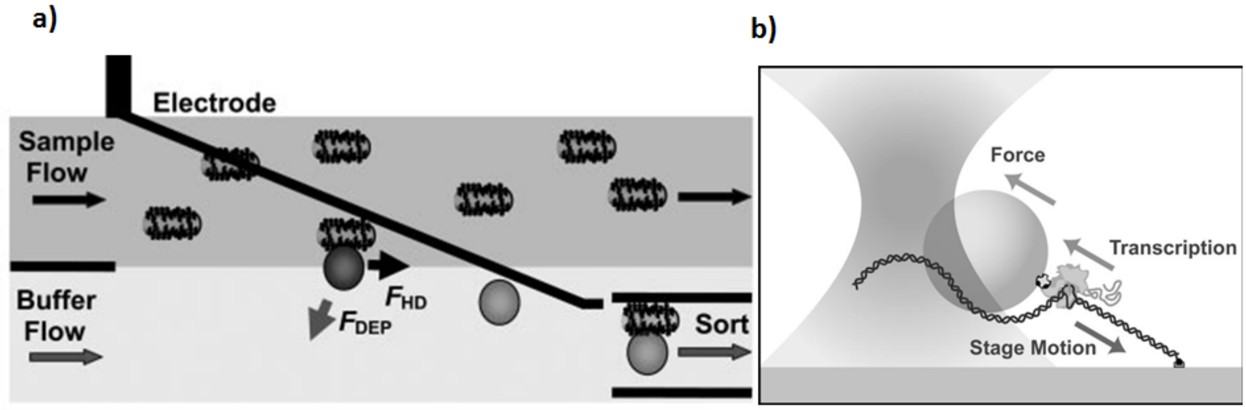

Figure 1.6: a) Dielectrophoresis of particles in a fluidic channel. Particles are under a net force towards the bottom of the channel, and end up being sorted. b) Optical trapping of a single bead. The gradient in the electric field forces the particles to the center of the focal plane. Particles end up being trapped, and the stage and substrate must be moved to manipulate the particle [41, 44].

excellent for manipulating a suspension of single objects in another object (ie. cells in water), complex suspensions with particles of a multitude of sizes and polarizabilities would yield a myriad of different outcomes [41, 42, 43]. However, these methods have become a method of cell sorting, and cell translation (Figure 1.6).

In terms of applying force to single cells, latex beads are typically attached to cells, and subsequently pulled by electric field. A single 15 μm latex bead will generate piconewtons of force [42].

1.1.3.4 Laser Trapping

Laser trapping offers one of the more powerful methods of particle control. In this method, the tiny momentum carried by light traps particles into the focal point of a laser beam. Due to the ability to modify the focal point and its size (by objective location and magnification), this technique can handle a large number of varying sizes and shapes of particles. The ultimate drawback of such techniques, and why it is rarely included in chip subsystems, is the need for complex objectives, a large external setup, precision mechanical translation of objectives, and difficulty in controlling large batches or multiple groups of particles. In addition, this technique suffers from the same selectivity concerns as dielectrophoretic methods, as any particle in the focal point is trapped [44, 45].

Laser trapping, similar to with dielectrophoretic methods, has been used to apply forces to single cells [45]. Due to higher power output, these lasers typically generate significantly higher forces than its dielectrophoretic counterparts. With single powerful lasers (up to 1 W power, Nd:YAG lasers), experimentalists typically generate up to 200 pN of force on particles 2 μm to 3 μm in diameters [45]. Particles at different locations can be controlled by beam splitting, however, as power is split, this significantly reduces the force at different locations.

1.1.3.5 Micropipette Suction

This technique utilizes flanking micropipettes where the cell surface is aspirated into a pipette tip (1 to 10 μm). This methodology is primarily used to measure the elasticity and model the single cell cytoplasm. This approach is typically not trivial to execute, as it requires fine alignment and mechanical control of the pipette tip, however, this technique can apply extremely high forces and stresses (theoretical limit of 100 nN / μm^2), as shown in Figure 1.7. Forces applied in experiments typically range from 10 pN to 1 nN [46, 47].

1.1.3.6 AFM tip

AFM utilize microfabricated tips and cantilevers to indent and deform cells mechanically. The AFM possesses high resolution and can output high forces (even beyond those of micropipette tips), however it is fundamentally a limited process. AFM tips can only indent surfaces and cannot pull on the cell, which is the most physiologically relevant mechanism [48, 49]. Water-viable AFM machines are also relatively costly, and AFM indentation is a serial process. Execution and setup of the procedure are similarly difficult and time-consuming, and interpretation of the resulting data is typically not trivial.

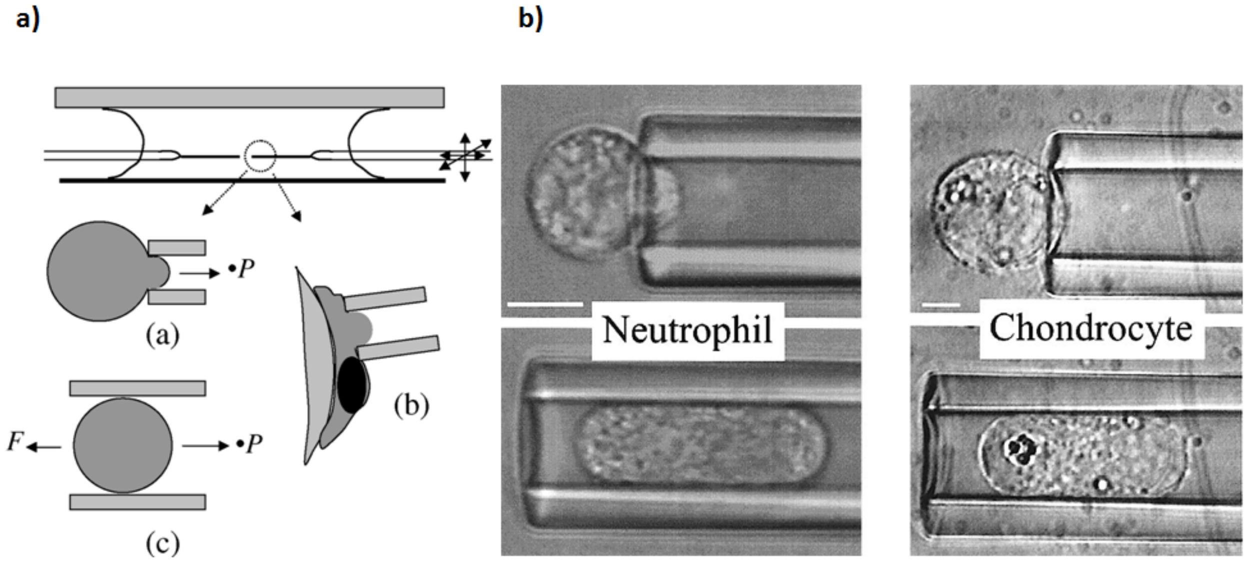

Figure 1.7: a) Schematic of micropipette suction technique. An aligned micropipette is incident onto a single cell and either pinches the cell, or directly apsirates the cell into the pipette tip. b) Images of cells being deformed and aspirated by pipette tips [46, 47].

1.1.4 Magnetic Manipulation

As the focus of this dissertation, we review magnetic manipulation methods more extensively here.

1.1.4.1 External Source-Driven

Magnetic particles provide powerful, selective control over environment, and as such have been under active research, although primarily as a means to control cells and trap certain biomolecules in-vivo. Simple setups use a permanent magnet to apply forces to drag the particles to one side of the channel, while more complex setups integrate fairly large ferromagnets to act as flux funnels to stabilize floating particles to a side of the channel.

1.1.4.2 On-chip coil-driven fields

There has been research to develop integrated methods of manipulating particles. For the most part simple lines or loops of wire flank the fluidic channel to provide an addressable means of controlling particle location. In addition, arrays of circular loops, and multiple lines of wire have also been utilized to translate particle position. These devices tend to be power hungry and possess low manipulation range and poor batch handling due to the limited fields that such devices are able to generate. Ideally, ferromagnetic material would be integrated with such devices to generate larger field gradients and improve the efficiency of such devices. As of yet, however, such integration has be relatively basic, and include the generation of simple pole tips flanking a channel (using a process that plants the coil on the wafer backside) and small pillars integrated with spiral coils [12, 13, 14].

1.1.4.3 Magnetic Particle-based cellular activation

Nanoparticle cellular activation is often based on the transfer of physical forces mediated by magnetic particles into a desired chemical action (Figure 1.8). These forces either create a collection and interaction of groups of particles, or generate twisting and torques to force open channels and porate membranes.

1.1.4.4 Magnetic Intracellular Localization Methods

Intracellular localization of particles is as of yet a fairly underdeveloped area of research. The one addressable method utilizes standard magnetic tweezing geometry (three to four pole tips flanking an area) and large exterior bulk coil setups to manipulate a single micron sized particle [18]. While the standard tweezing is useful for generating precision forces on single particles, it has trouble handling groups of particles, and developing large enough gradients to localize groups to highly defined locations. As such, the demonstrated manipulation occurred with a single particle, injected into the cell. The setup is also large, bulky, and incredibly power hungry, as the coils must drive field through a large amount of material. Magnetic-fluorescent particles have so far seen even more limited use, however they are

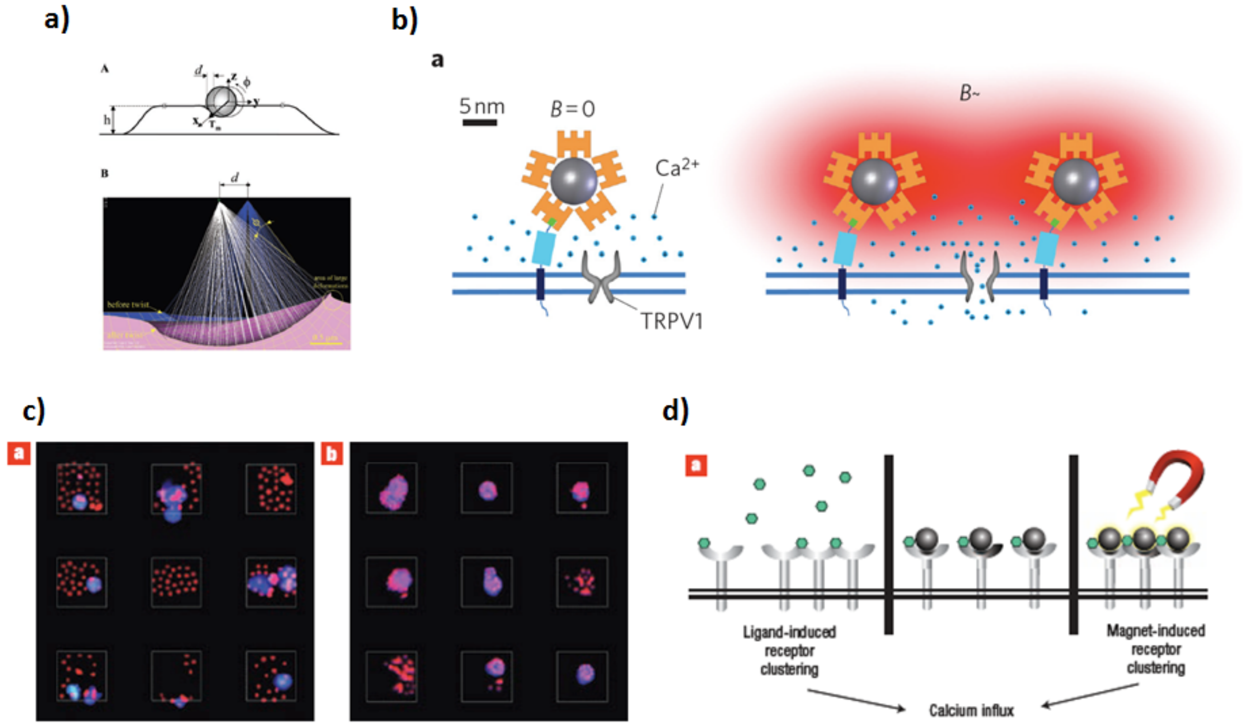

Figure 1.8: Various existing methods of cell control by magnetism. a) Magnetic deformation of single cells for determination of cellular rheology [50]. b) Magnetic nanoparticles attached nearby mechanosensitive calcium channels induce activation by magnetic nanoparticle heating [51]. c) Magnetically induced cell death whereby cells attached to particles die upon release of the underlying magnetic field [52]. d) Calcium influx generated by clustering of receptors under magnetic field [16].

particularly useful for visualization, especially for sub-100 nanometer sized particles (Figure 1.9). Biological setups are similarly equipped to handle the visualization of multiple fluorescence bands, meaning such particles could be tracked easily in standard tools. Intracellular manipulation of these has so far only been demonstrated with a single magnet, localizing the particles to one side of the cell [53].

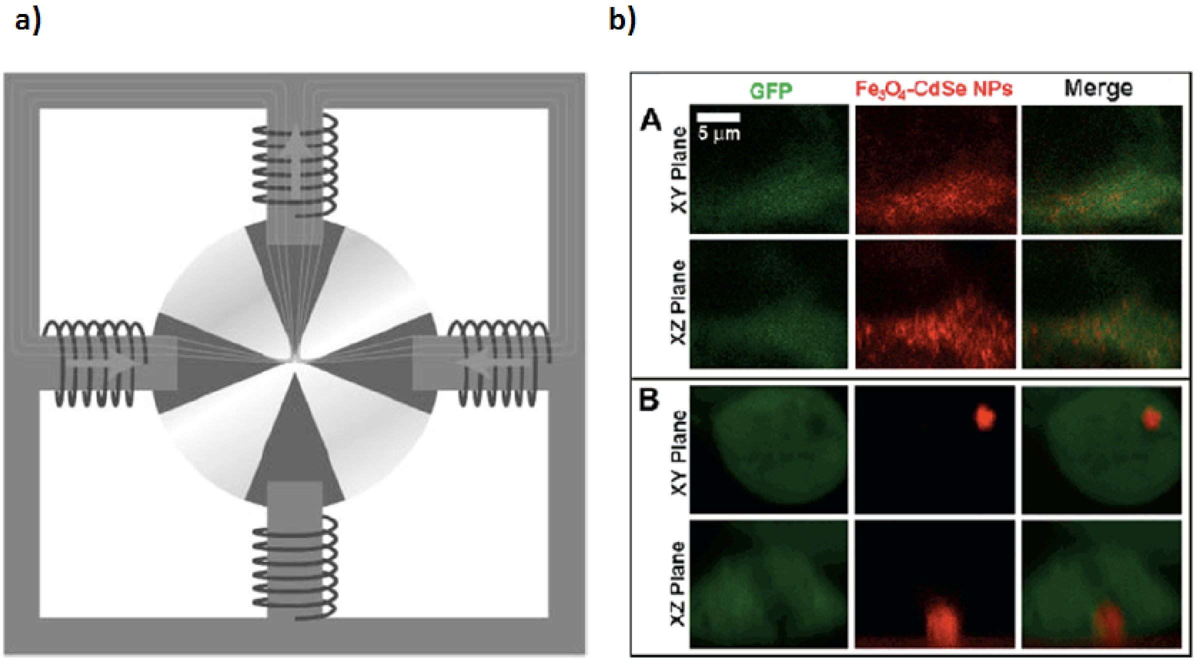

Figure 1.9: Methods used to manipulate particles inside of cells include a) giant electromagnet setups to drive magnetic tweezers, and b) coalesced magnetic-fluorescent nanoparticles under magnetic stimulus [18, 53].

1.1.5 Summary of Existing Mechanical Approaches

In general, the existing approaches to apply forces have limitations. While approaches such as cell stretching and fluidic shear can operate on many cells at a time, they are inherently limited in terms of applying an equivalent force over all cells, and being unable to probe localization of forces. Optical trapping and dielectrophoretic methods are able to apply more versatile forces (at various points around the cell), however have scalability limits. In table 1.1 is listed a variety of parameters for existing incarnations of approaches.

Table 1.1: Comparison of Mechanical Techniques

Method	**Force** [nN]	**Serial vs. Batch**	**Length of Force** [μ**m**]	**experimental constraints**
micropipette	1 (up to 100 theoretically)	Serial	1 to 10	alignment difficulties, slow process
dielectrophoresis	.001	Batch	5 to 15	unwanted crosstalk
optical trap	.2	Serial (Batch by sacrificing force)	2 to 6	optical alignment
AFM	N/A	Serial	2 to 20	expensive liquid-AFM, integration with fluorescent microscopy, slow
Our magnetic platform	100	Batch	2 to 25 (adjustible)	proximity to magnet, bright-field microscopy for inverted microscopes

1.2 Interfacing with the Intracellular Environment with Magnetic Nanoparticles

As shown there remains a dearth of methods to activate and probe cellular function at the nanoscale, important for understanding these processes. Magnetic particles have gained wide acceptance in biological and medical research as a method of selectively controlling biological environments. Antibody or DNA-conjugated particles have been used for highly specific methods of sorting cells, proteins and DNA, and they have been used in conjunction with detectors to determine particle conjugation and size [55, 56, 57, 58]. More recently, researchers have integrated particles with additional characteristics [19], including conjugating

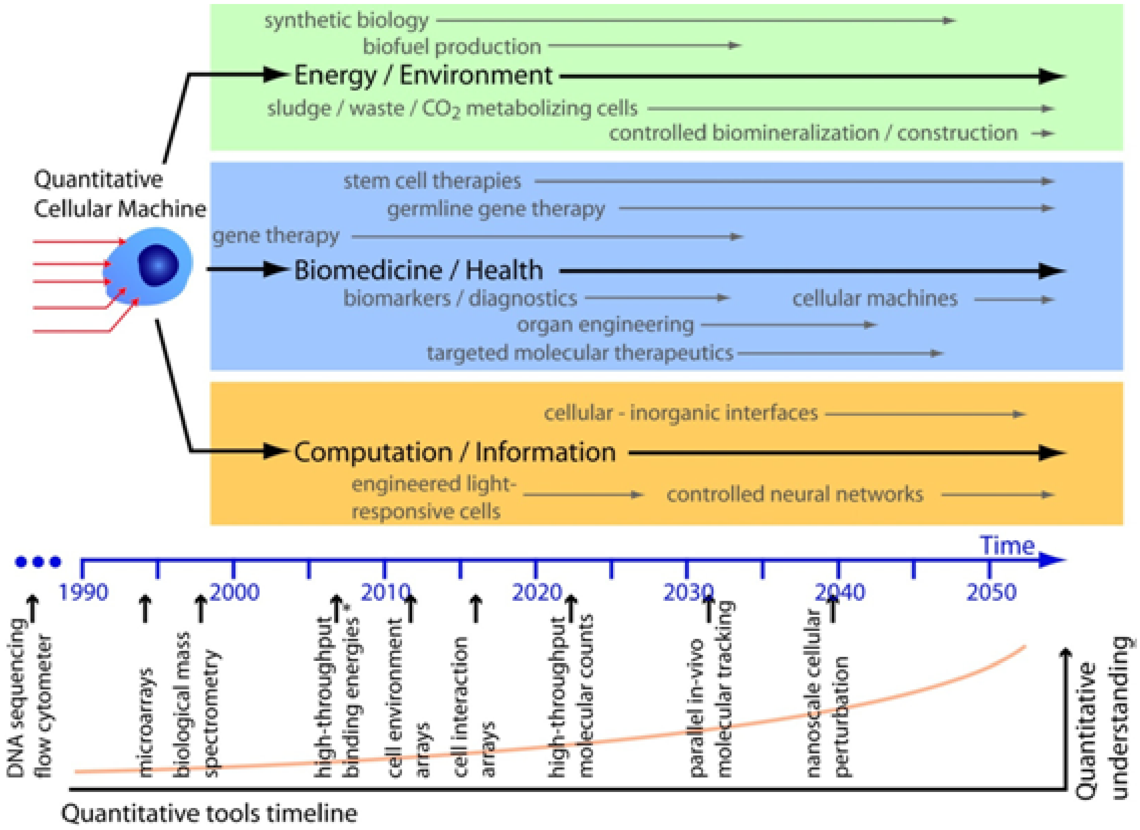

Figure 1.10: Past tools such as DNA sequencers, flow cytometers, and microarrays have allowed improved quantitative understanding of biological systems. A variety of new high-throughput tools will be necessary in the coming decades (example break-through instruments include high-throughput binding energy measurements (Maerkl and Quake [54]), and proposed work for micro to nanoscale cellular perturbation). These new tools are poised to allow breakthroughs in fields from biofuel production, gene therapy, to cell-computer interfaces.

particles with quantum dots for ease of detection, and fabricating porous particlesconjugated to enzymesto be used as highly active reaction templates [58, 59]. Magnetic beads have been used to remotely generate heat [17], control ion channels, mediate signaling, and probe cell mechanics [50, 16, 17]. Even with these advances, the potential for this technology and its use for the cellular localization of signals remains largely untapped [60]. This is especially important given the high level of localization and compartmentalization important for cellular function.

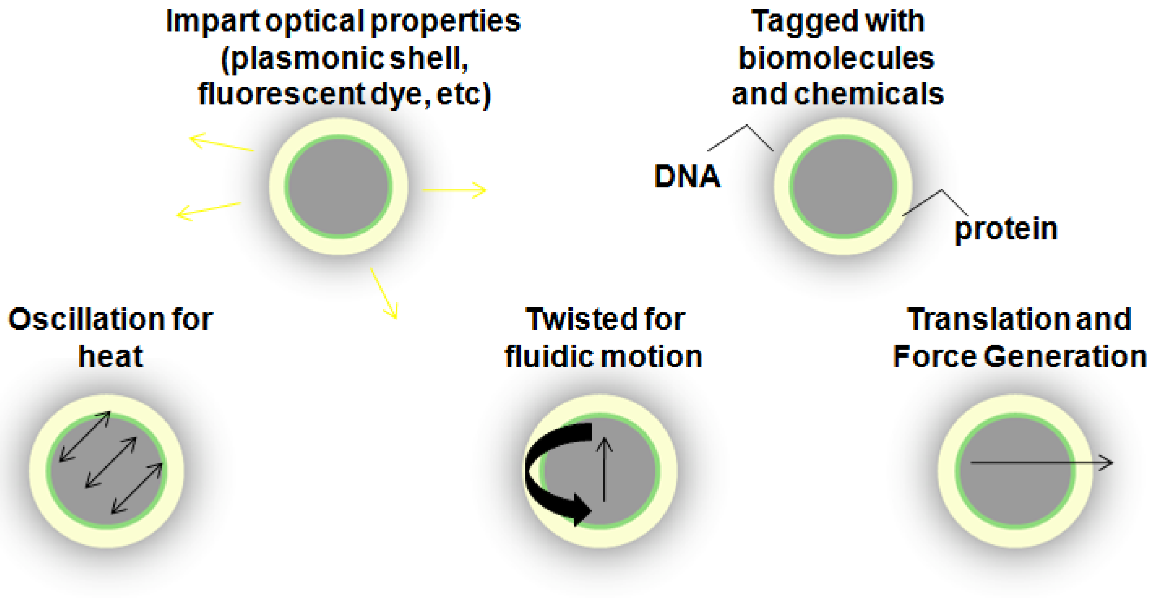

Figure 1.11: Magnetic particles transduce a variety of signals. Conjugation with fluorophores and plating with metals can impart optical properties, while conjugation with biomolecules can impart biochemical activity. Magnetic particles by default can be oscillated to generate heat, rotated, or directly translated mechanically.

Micro-Electro-Mechanical Systems (MEMS) technology, and its ability to interface with microenvironments is well suited as a means of interaction with magnetically coupled biological matter. While there has been ample investigation into microfabrication as a means of sorting and manipulation of biological material, its use in generating magnetically-mediated, single cell biological activity is scarce. The capability of generating, in a simple fashion, highly localized chemical and mechanical effects could give biologists a simple method of probing cellular architecture and biochemistry, as well as providing a unique method of studying highly localized cellular signaling.

Techniques for magnetic actuation of paramagnetic and super-paramagnetic particles usually follow simple setups to manipulate particles using a permanent magnet to apply

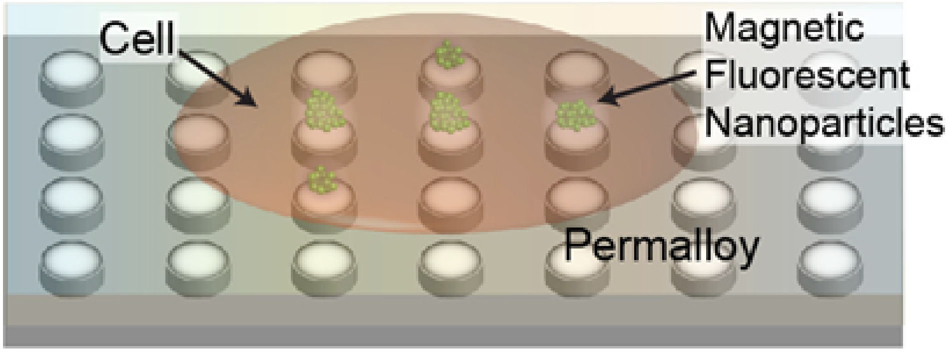

Figure 1.12: Schematic representations of our technique. a) A single cell with internalized magnetic fluorescent nanoparticles is adhered above our substrate, and whose magnetic particles are assembled by a magnetic field.

forces to drag the particles to one side of a container or channel, while more complex setups integrate fairly large ferromagnets to act as flux funnels to stabilize floating particles to a side of the channel [11, 12]. There has also been research to develop integrated methods of actively manipulating particle localization. For the most part, these devices are comprised of simple lines or loops of wire flanking the fluidic channel to provide an addressable means of controlling particle location. In addition, arrays of circular loops, and multiple lines of wire have also been utilized to translate particle position. These devices tend to be power hungry and possess low manipulation range due to the limited fields that such devices are able to generate. Ideally, ferromagnetic material would be integrated with such devices to generate larger field gradients and improve the efficiency of such devices. As of yet, however, such integration has been relatively basic, and includes the generation of simple pole tips flanking a channel (using a process that plants the coil on the wafer backside) and small pillars integrated with spiral coils [13, 14, 15], not approaching nanoscale localization control, and not control internal to cells.

1.2.1 Summary of Approach

We separate our approach into two general types.

Approach 1

A magnetically active substrate that can dynamically manipulate magnetic nanoparticles in real-time, to dynamically alter the intracellular landscape (Figure 1.12). To achieve this we propose to use a substrate composed of periodic ferromagnetic lines and tips, combinations of which, in an incident magnetic field, will generate unique, repeating magnetic-flux-density maxima. Within a cell, these maxima attract and coalesce particles, generating designed patterns of ensembles of nanoparticles at high speed. Importantly, the device is engineered for controllable localization (Figure 1a), as the magnetic potential minima can controllably span nearly all x-y points of the substrate depending on orientation of an external permanent magnet. The incident fields can be ultimately decomposed into two base modes: normal and tangential fields, combinations of which can be generated by a simple flanking magnet. The approach massively improves on existing methodologies by 1) allowing simultaneous control of multiple ensembles of particles, 2) allowing ultra-precise manipulations corresponding to shifts in the external magnet, and 3) generates massive forces all along the manipulation pathways, as ensembles are always close to the neighboring, excited tip.

Approach 2

Utilizing a simple magneto-substrates for more composed studies on many single cells. These substrates are composed of single ferromagnetic elements flanking single protein-patterned and shaped cells, and are meant to study constant localized stimulus (for example, force) at a constant location. Strong magnetic field gradients generated by magnetizing micro-elements in close proximity to patterned cells allows for the remote generation of large forces or amplify biochemical response of the nanoparticles via the coalescence of cell-internalized magnetic nanoparticle ensembles (Figure 1.13). At the core of this platform is a micromagnetic substrate composed of: i) electroplated soft magnetic (Nickel-Iron) elements, ii) a biocompatible, planarized resin layer, and iii) lithographically patterned cell-adhesion and cell-blocking layers to precisely align magnetic-nanoparticle-dosed cells adjacent to micro-magnets. Magnetizing the micro-magnetic elements with a permanent magnet generates large, arrayed magnetic potential minima that rapidly and precisely localize nanoparticles inside of cells, ultimately yielding highly consistent, force-generating nanoparticle ensembles over arrays of uniformly shaped cells. The uniform shape of patterned cells

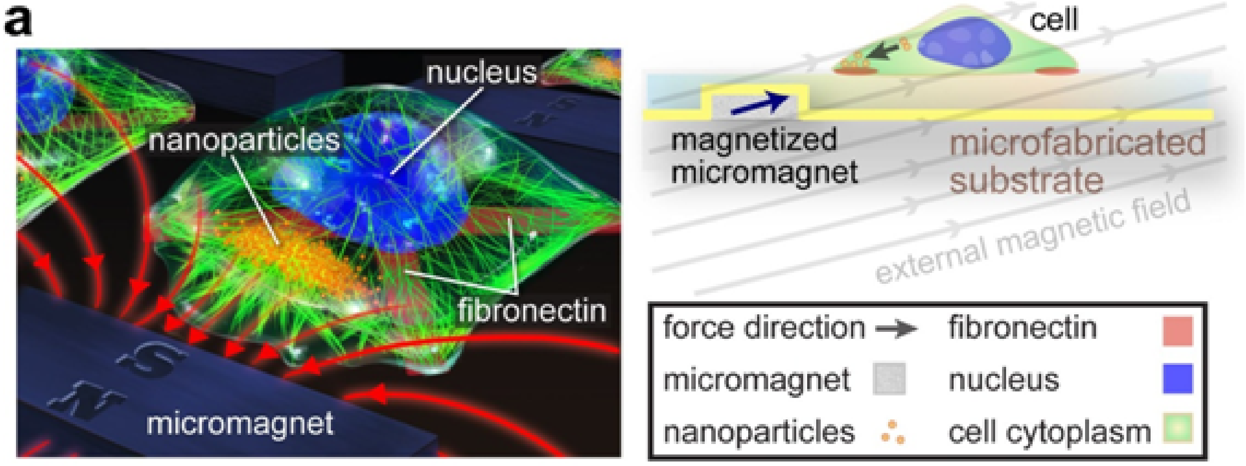

Figure 1.13: a) Artists schematic and diagram of the major components of our force-generating platform. A large permanent magnet remotely magnetizes micromagnetic elements in proximity to fibronectin-patterned cells, coalescing magnetic nanoparticles into force-generating clusters within each cell.

allows for a reduction in cell-to-cell variation and eases image processing when analyzing responses. The high field gradients created by local micro-magnets lead to a short timescale for localized assembly of nanoparticles.

1.3 Scope of Thesis

This dissertation will begin by introducing the important elements of the magnetic physics involved in our approach. We will begin by describing the functionality of our periodic substrates before deriving the force experienced on the magnetic particles used in our various experiments. Finite-element simulations of our various substrates acheived through ANSYS and COMSOL Multiphysics will be analyzed. From this, we will estimate the coalescing and manipulation time for our periodic substrates. Moving outo our force-generating substrates, we will then model the forces experienced by coalesced particles inside a cell under the stimulus of our magnetic particles, and verify and compare our results with a fluidic approach.

Chapter 3 will outline the fabrication process for our substrates, decomposing each critical section, and the fabrication pitfills which had to be avoided, and our methods in detail. We will then examine the chemistry to synthesize our magnetic-fluorescent, high internalization rate nanoparticles.

Chapter 4 will explain both experimental and numerical methods used in our papers.

Chapter 5 will report on the core results of our substrates, including the dynamic manipulation capabilities, patterning consistency, and manipulation speed of our periodic substrate. For our force-based substrates will reveal the resuling asymmetry in biology generated by magnetic stimulus.

Chapter 6 will conclude this dissertation by examining future possibilities of these magnetic approaches, including the integration of different input-outputs to the general system.

CHAPTER 2

Aspects of Physics and Design

We will attempt to describe the manipulation of the force on magnetic particles by introducing a fairly simple derivation, and subsequently modelling and comparing the fields generated by fabricated micro-magnetic elements.

2.1 Energy of a Magnetic Dipole in a Magnetic Field

In this section we will derive the force on magnetic particles. As with all electromagnetic problems, we begin with Maxwell's Equations, although they are not needed explicitly to derive our result:

$$\begin{gathered}
\nabla \times \overrightarrow{E} = \frac{-\partial \overrightarrow{B}}{\partial t} - \overrightarrow{M}, \\
\nabla \times \overrightarrow{H} = \frac{-\partial \overrightarrow{D}}{\partial t} + \overrightarrow{J}, \\
\nabla \cdot \overrightarrow{D} = \rho, \text{and} \\
\nabla \cdot \overrightarrow{B} = 0,
\end{gathered} \tag{2.1}$$

with electric field E, magnetic field H, electric flux density D, magnetic flux density B, magnetic current density M, current desnity J, and charge density ρ.

Typically in micro-electro-mechanical systems, we attempt to derive quantities that describe the energy of the system — the only conserved quantity throughout the interleaving physics of a MEMS system. This is true in our cases here, as we attempt to transfer energy from magnetic particles into mechanical force on biological material. Once we have described the energy of the system, we can directly derive the force on particles by taking the gradient.

The force experienced on an electrically charged particle moving through a constant magnetic field is traditionally known as:

$$F = qV \times \overrightarrow{B} \tag{2.2}$$

This quantity can be transformed quickly into a torque acting over space to yield the following equation:

$$T = m \times \overrightarrow{B} \tag{2.3}$$

with magnetic moment m, where m is traditionally known in terms of loops of current, I, over some area, A.

Through direct mathematical manipulation, we can express this value as energy:

$$\begin{gathered} U = \int\limits_{\theta} m \cdot \left|\overrightarrow{B}\right| \cdot \cos(\theta) \cdot \partial\theta, \\ U = -Bm\cos(\theta) + C \end{gathered} \tag{2.4}$$

This value is equivalent to the dot product of the magnetization and magnetic induction values, and yields the final equation:

$$U = -\overrightarrow{m} \cdot \overrightarrow{B} \tag{2.5}$$

This value is canonically known as the energy of a magnetic moment in an incident magnetic field. The magnetization of paramagnetic particles follows the incident field at low frequencies, and thus the dot product can be replaced with a simple multiplication factor. We can use the above modified equation to derive force under a changing magnetic field by taking the gradient:

$$\begin{gathered} F = (m \cdot \nabla)\overrightarrow{B}, \\ m = V\frac{\overrightarrow{B}\chi}{\mu_o} \end{gathered} \tag{2.6}$$

This is the equation to describe force in the vast majority of texts, and assumes non-saturating conditions whereby the magnetization of the particle is still linearly dependent on the incident magnetic field. For our cases, due to our high incident magnetic field, the particle is assumed saturated, upon which we can assume the magnetization as a constant. Indeed, this both simplifies the calculation, and reduces the error of our calculation, as it reduces the dependency on the incident field from a square term to a linear term. Our final used equation is:

$$F = VB_{\mathrm{sat}}\frac{\overrightarrow{B}}{\mu_{\mathrm{o}}} \tag{2.7}$$

To simplify our analysis, we will try to portray everything in terms of the magnetic induction, B (Tesla).

2.2 Magnetization of Nanoparticles Used

The first particle we used was purchased from Chemicell (Germany), and from data sheets given by the supplier, report a saturation of .01 Tesla.

For Dynabead MyONE - streptavidin bound particles used to verify the behavior of our magnetic elements [61], it has been calculated in literature to have a saturation magnetization of 23.5 Am^2/kg. Streptavidin MyOne particles have a density of 1.8 g / cm^3.

$$\begin{gathered} 23.5\frac{emu}{g}(\frac{1.8g}{cm^3}) = 42.3\frac{emu}{cm^3}, \\ 1\frac{A}{m} = 10^{-3}\frac{emu}{cm^3}, \\ 42.3\frac{emu}{cm^3} = 42300\frac{A}{m} \end{gathered} \tag{2.8}$$

This value can be converted to the Tesla required in our equation by multiplication with μ_{o}, and yields a saturation magnetization of .0532 Tesla.

For nanomag-D particles from micromod (Germany), the saturation magnetization is reported as greater than 75 emu/g iron for particles with a density of 3.0 g/cm^3. As reported from the company, particles are approximately 50 percent iron, and thus possess 75 emu/g for

1.5 $g(Fe)/cm^3$. Undergoing similar mathematical manipulations as above for the dynabead particles, this yields a saturation magnetization of close to .15 Tesla. For purposes of our paper, we used a magnetization of .12 Tesla in accordance with the saturation magnetization the company reported for earlier batches of nanoparticles.

2.3 Operation of Magneto-active Substrates

In this section we explore the general operation principles for our two magnetic manipulation approaches.

2.3.1 Dynamic Manipulation of Magnetic Fields with Ferromagnetic Dots

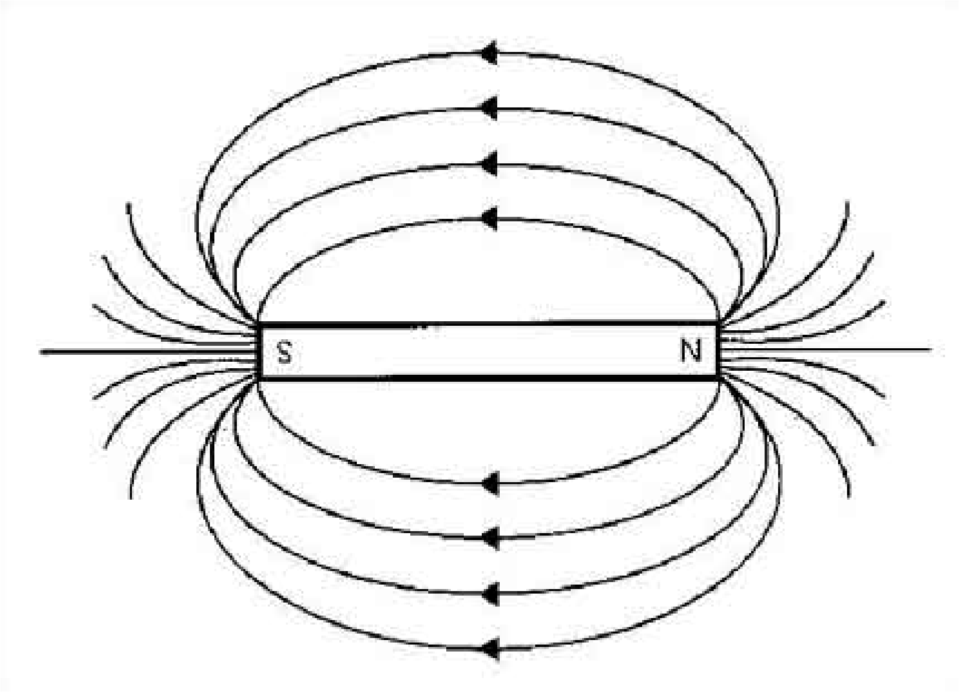

Figure 2.1: A larger proportion of the magnetic flux routes through the edges of the magnet, as this provides the path of least resistance (or reluctance, more specifically).

Under non-saturating conditions, ferromagnetic elements will invariably carry high magnetic fields nearly exclusively at the edges of the magnetic dot, as this minimizes the induced energy of the system, while satisfying the bounding magnetic field conditions. This is shown in Figure 2.1, where the majority of the magnetic field lines will route through the corners of the magnet, yielding a locally higher field at these points. This consistency in field response can be avoided in high fields, as the magnetic moment at each point begins to align directly with the incident field as the field supplies enough energy to realign and reorient the magnetic domains directly. This alignment of all the magnetic dipoles throughout the magnetic medium yields vastly different response than the non-saturating condition. It is this realignment that is exploited in our ferromagnetic substrates to generate manipulation capabilities of these substrates.

Shown in Figure 2.2 is a diagram of magnetic response under high fields. The response can generally be decoupled into two major modes, a tangential mode and a normal mode. For the tangential response, the magnetic dipoles align on their side, in plane of the substrates, and the potential energy minima for particles occupy points in between the ferromagnetic dots. For a normal magnetic field, the magnetic dipoles in the ferromagnetic dot will point out of plane of the substrate, and at a reasonable height above the substrate, generate potential energy minima for particles directly in the center of the dot. This creates two starkly different positioning points for particles at these two different incident fields.

It is this varying response that is exploited to form tunable patterns of magnetic nanoparticles. Generating purely normal and purely tangential fields are difficult, but we can closely approximate these modes, and all combinations in between, through the use of a single strong permanent magnet. As show by Figure 2.1, the centers of magnets must generate close to normal magnetic fields, while at distances displaced from the edge of the magnet, tangential fields will be generated. By simply shifting the magnet across the substrate, as shown in Figure 2.2, we can acheive high precision manipulation of magnetic particles. Essentially, the position of the magnet in relation to the micromagnetic substrate controls precisely the location of the magnetic nanoparticles in relation to the micromagnets.

This ratcheting mechanism gives engineers the ability to either hold particles at distinct patterns, or to manipulate them actively and continuously through modification of the external field.

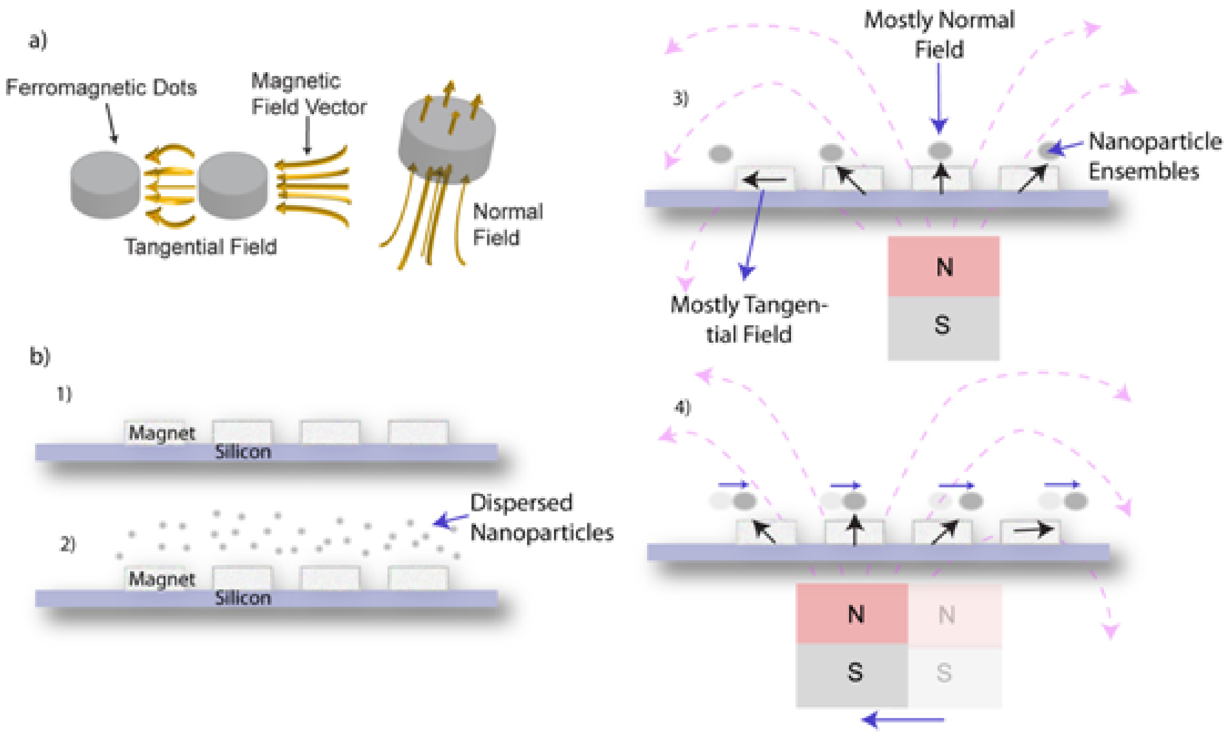

Figure 2.2: A larger proportion of the magnetic flux routes through the edges of the magnet, as this provides the path of least resistance (or reluctance, more specifically).

2.3.2 Stimulating Living cells with Force

We utilize simpler magneto-substrates for more composed studies on many single cells. These substrates are composed of single ferromagnetic elements flanking single protein-patterned and shaped cells, and are meant to study constant localized stimulus (for example, force) at a constant location. Strong magnetic field gradients generated by magnetizing micro-elements in close proximity to patterned cells allows for the remote generation of large forces or amplify biochemical response of the nanoparticles via the coalescence of cell-internalized magnetic nanoparticle ensembles.

2.4 Simulating Magnetic Response

Our samples are simulated using both ANSYS FEM and COMSOL Multiphysics.

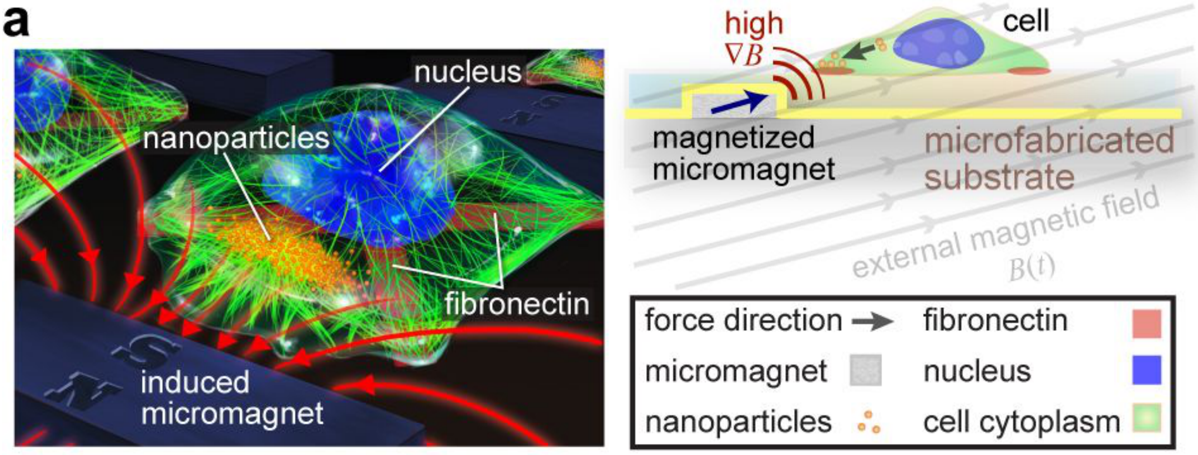

Figure 2.3: High gradient magnetic fields generated around magnetic elements localize nanoparticles to positions flanking the cell cortex, generating nanoparticle-mediated force.

2.4.1 Response of Periodic Micromagnetic Substrates

The focusing effect of the permalloy was numerical simulated with 3-D ANSYS FEA software, by modeling the permeability as a hyperbolic tangent function of our permalloy saturation and permeability, and obtaining solutions at various heights above the substrate. The thickness of the SU-8 layer used to planarize our substrate is verified to be approximately 0.5 to 1 μm above the permalloy dots. The extracted magnetic gradient at 1 μm is shown in Figure 2.4. As can be seen in comparison plots of normal and tangential excitation, the magnetic potential minima switches from being above the elements, to being in between the magnetic elements. The tangential field is slightly lower than the normal incident field due to the thickness being thinner than the diameter.

The magnetic induction was extracted directly from ANSYS, and subsequently fitted with an 8th order polynomial in MATLAB in order to smooth out the response. Contours of the magnetic flux density for normal mode of operation are given in Figure 2.5, for a plane located 1 μm above magnetic dots placed in a magnetic flux density of approximately 0.6 T. Overlayed in the same plot is the magnetic gradient felt by the particles.

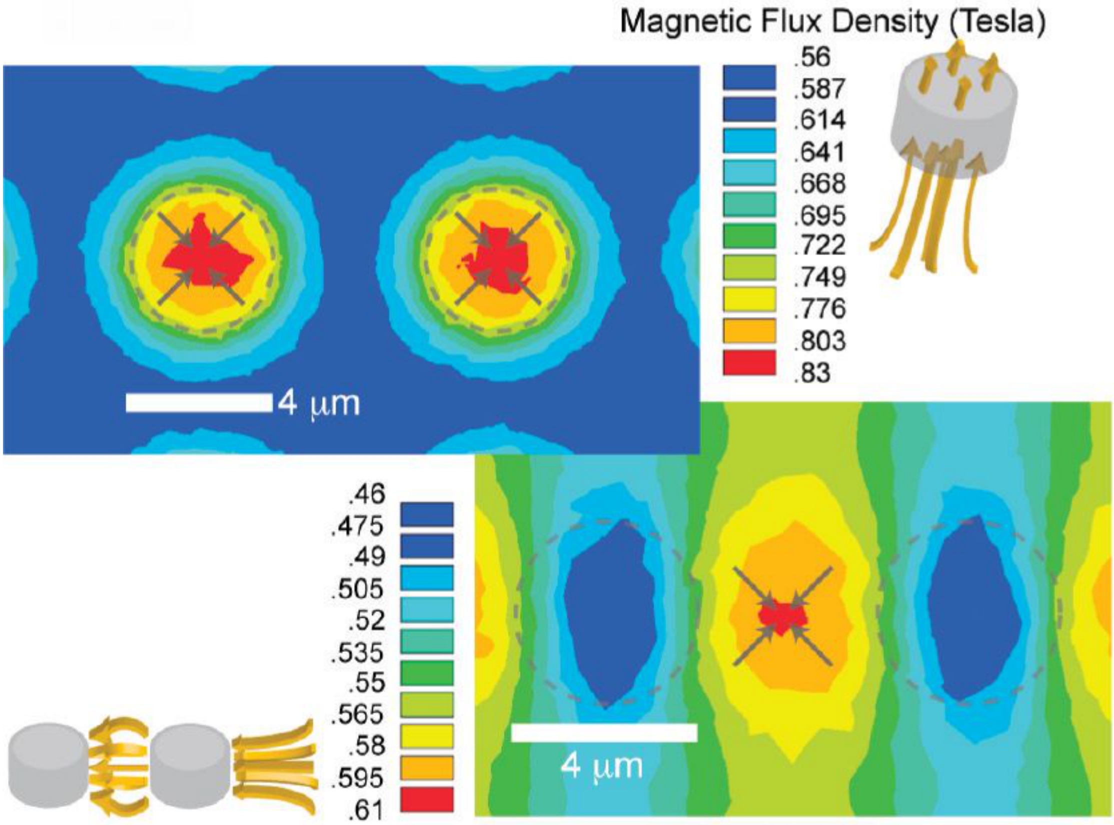

Figure 2.4: Magnetic-flux-density contours as simulated in ANSYS at 1 μm above the patterned 4-μm-diameter dots arranged in a 4-μm-pitch array. Dashed circles indicate the edge of the ferromagnetic dots.

The maximum magnetic gradient occurs at around the edge of the element, and peaks at around 100,000 T/m, and on average, particles experience around 50,000 T/m. For tangential fields, the gradient felt is a little more than half this value.

2.4.2 Response of Single Flanking Micromagnet

The magnetic response for our force-generating substrates is under significantly more scrutiny because we are attempting to establish an accurate estimate of the force. Due to the complexity of handling ANSYS simulations, COMSOL was chosen to simulate the magnetic fields as the user interface is simpler to navigate. We utilize the 3-d, static magnetic simulation capabilities to extract the relevant magnetic fields. 2-d cross-section plots for the simulated

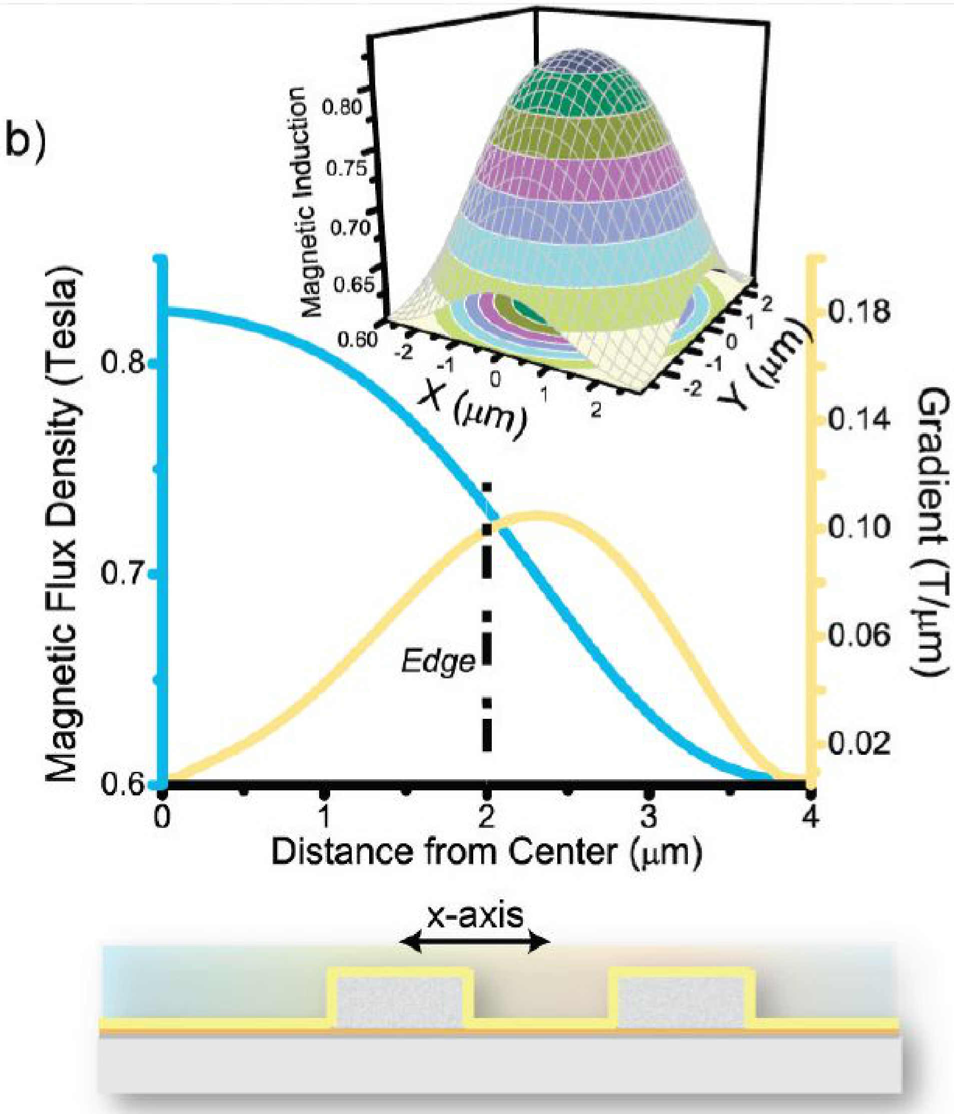

Figure 2.5: Overlayed plots of the magnetic flux density and corresponding radial gradient as we progress away from the dot midpoint for a normal incident field. The inset graph displays the contours of the magnetic flux density as generated by a best-fit polynomial (assumed radially symmetric). The edge is denoted by the dashed line, and coincides with the approximate peak of the magnetic field gradient.

magnetic field is shown in Figure 2.6.

Because our substrates are of similar size to our incident magnet, the magnetic field

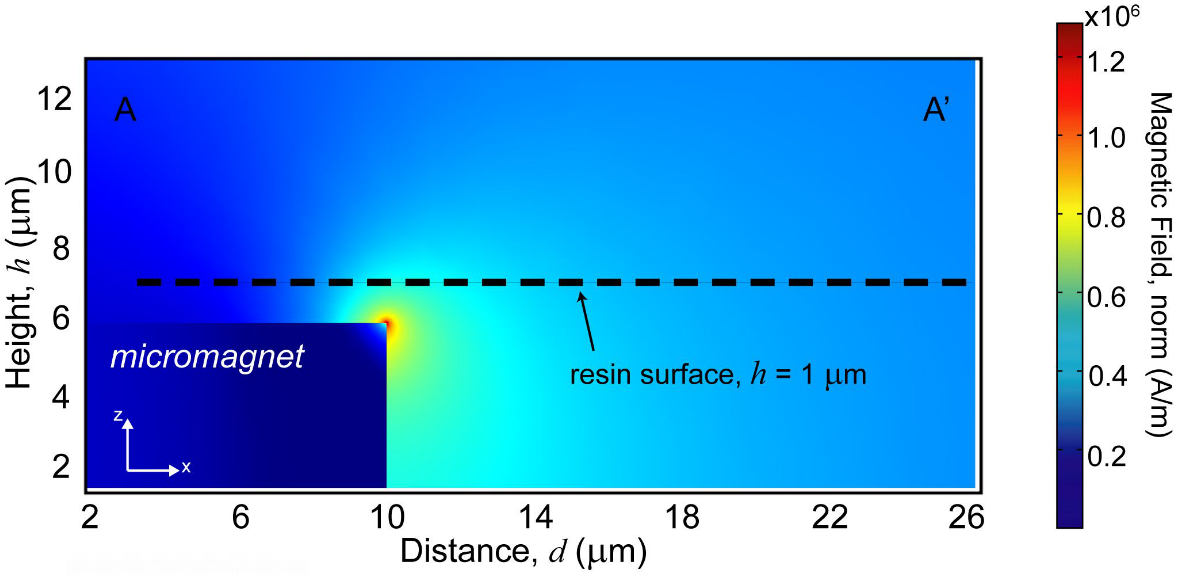

Figure 2.6: Magnetic fields generated by a single 30 μm by 20 μm by 10 μm element under a tangential magnetic stimulus from a single permanent magnet.

varies as a function of the orientation of the micromagnet with the permanent magnet. For simplicity, we measure the magnetic field generated by our permanent magnet at three different positions and use these as our simulation points for our magnet. As shown in Figure 2.7, the tangential field remains a constant .3 Tesla across our substrate, while the normal field varies significantly enough to warrant the separate simulations (0 T to .15 T).

The variation of the magnetic field for these three variations of the field is shown in Figure 2.8. The magnetic field and magnetic gradient are higher towards the corner of the magnet, as the induced angle in the dipole of the magnet induces a higher field.

2.5 Substrate Operation Metrics

Here we will extract some meaningful parameters on our substrate capabilities, such as the time constant for the operation of our periodic substrates, and the forces generated by our magnetic substrate.

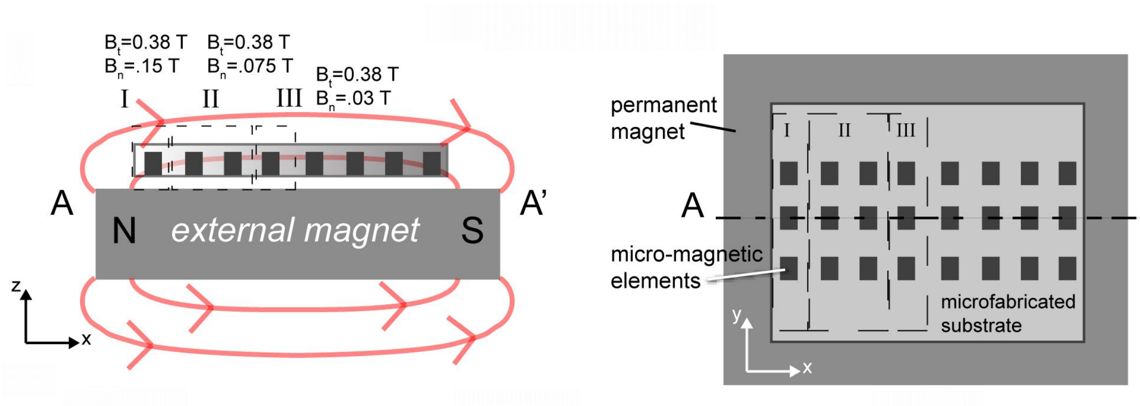

Figure 2.7: Magnetic fields generated by a single 1 in by 1 in by 1 in NdFeB magnet. The approximate orientation of our flanking magnet and the area of interest of our sample is shown to the right. The tangential field remains approximately constant over the range of the sample, while the normal field varies from 0 to .15 Tesla in magnitude.

2.5.1 Time Response of Periodic Substrate

As shown in Figure 2.5, the forces on the Chemicell particles we used for these experiments typically vary from close to 0.1 to 1 pN over its range of motion, and varying with the thickness of our planarizing layer.

The response time of a magnetic particle to our base array from any point can be determined directly by examining the equation of motion for the magnetic nanoparticles in our system:

$$\begin{gathered} m \cdot \frac{\partial v}{\partial t} = F_{\text{mag}} - F_{\text{drag}} \\ F_{\text{drag}} = 3\pi\mu a v \end{gathered} \tag{2.9}$$

with particle velocity in a stagnant fluid v, hydrodynamic diameter a, and kinematic viscosity μ.

Due to the negligibly small mass of nanoparticles, the velocity will stabilize at a steady state velocity given by:

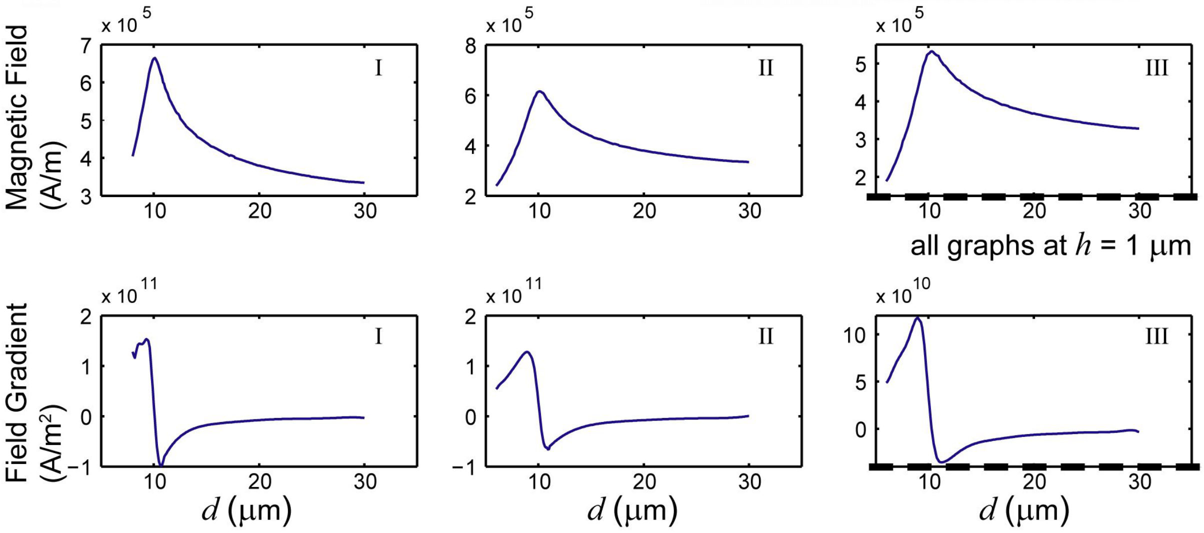

Figure 2.8: Shown at top are the magnetic field responses for in the different sections, while the below graph is the corresponding magnetic field gradient. Due to the larger normal field, the asymmetric orientation of the magnetic dipole yields a slightly larger field at the sides of the substrate. The lowest field and gradient are caused by the center section, with nearly all tangential component of force.

$$v_{\mathrm{ss}} = \frac{F_{\mathrm{mag}}}{3\pi\mu a} \tag{2.10}$$

This value is directly proportional to the magnetic field gradient at any position. This equation of motion for the nanoparticles can be solved to obtain a quick estimate of our response time (or time for assembled nanoparticle patterns to become noticeable). We will define this time as the initial formation time constant, τ. Ignoring the z-dimension, we obtain an approximate response time constant of 100 ms in water for a 4-μm-diameter dot in 4-μm-pitch array. Since the cell cytoplasm has a viscosity that is a complex function of spatial dimension, the time response in the nonlinear space of the intracellular medium would be a value moderately higher than that in water. While our time constant for water was predicted for our 100-nm-diameter particles, the manipulation speed for particles half this size (50 nm, which is closing in on the pore size for the nuclear membrane), would yield speeds only four times slower (400 ms), which is still fairly rapid.

2.5.2 Estimating Forces on our Particles

The magnetic nanoparticles, when coalesced, form a 3-dimensional structure along a non-linear magnetic gradient. To properly model the force, we must take into account this aspect of the generated force. From our comsol simulations we extract the magnetic field at a cross section (as in Figure 2.6), and crop the field to relevant points of interest. This value is fitted linearly in MATLAB, and this fit is plotted in a x-z meshgrid at a spacing at .2 μm resolution, and moderately smoothed with a simple Gaussian filter. This smoothed Z value is plotted in Figure 2.9. The edges of the magnet are at x = 10 μm, and z = 4.75 μm, as the 30 by 20 by 9.5 elements are centered in the mesh.

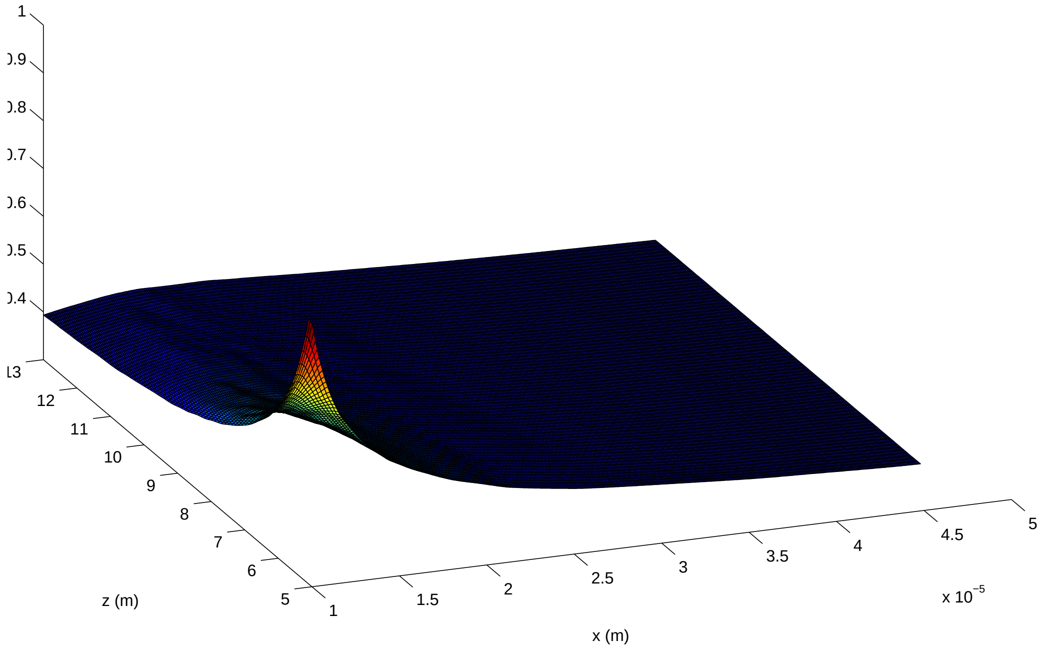

Figure 2.9: Extrapolated, linear fit of the COMSOL response. The edges of the magnet are at x = 10 μm, and z = 4.75 μm.

From the smoothed magnetic field we extract the magnetic field directly, and finally we obtain magnetic field gradient in the x-direction, from which we can obtain the x-magnitude of the force. This plot is shown in Figure 2.10. Magnetic nanoparticles in the x-z dimension can be mapped onto this x-z plot to obtain a continuum of force.

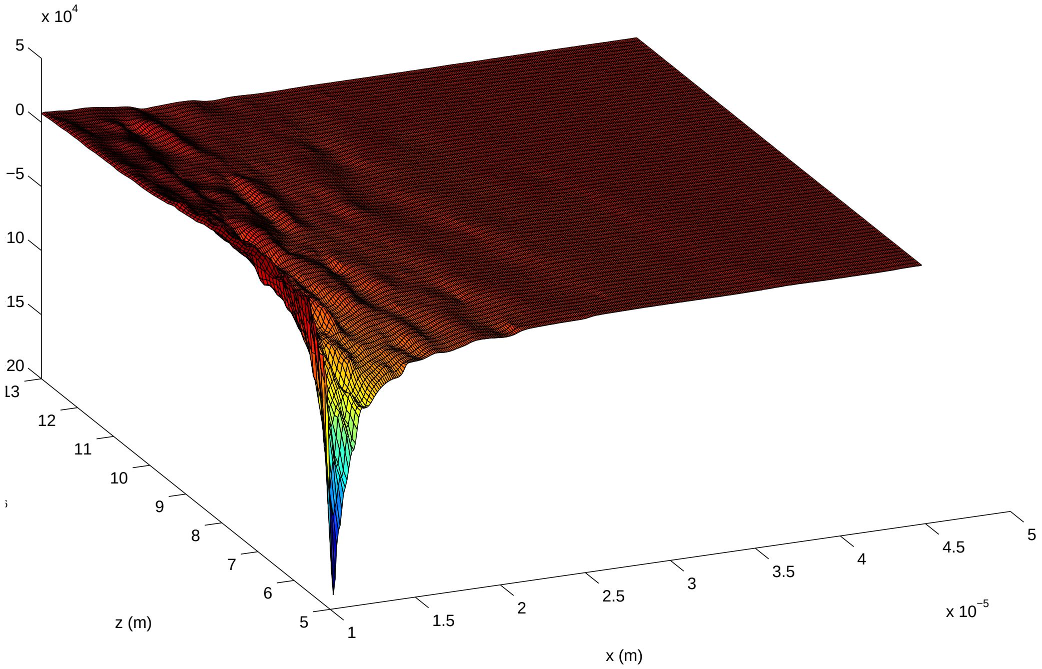

Figure 2.10: X-direction gradient of the magnetic field. The edges of the magnet are at x = 10 μm, and z = 4.75 μm.

2.6 Experimental Verification of Force

Experimental verification of force generated by our magnetic substrates is critical as we are attempting to draw relevant biological knowledge from our substrates. We verify our generated forces through a fluidic approach.

2.6.1 Drag Force for Trapped Particles near a Plane

For a low Reynolds Number system, the drag on a particle can be approximated by the following equations involving the drag coefficient:

$$\begin{aligned} F_{\text{drag}} &= \frac{1}{2}\rho v^2 c_{\text{d}} A \\ c_{\text{d}} &= \frac{24}{Re} \end{aligned} \tag{2.11}$$

This equation reduces directly to the typical equation for Stoke's drag force:

$$F_{\text{drag}} = 6\pi\mu R v \tag{2.12}$$

Our case is slightly different, however, as our particle is tightly flowing next to a planar surface. This then modifies the drag coefficient [62]. The lateral drag coefficient experienced by a sphere trapped close to a plane is given by Faxen's Law for when velocity at infinity approaches 0, as is the case for our system. Faxen's Law is thus:

$$\gamma_{\text{lateral}} = \frac{\gamma_0}{1 - \frac{9R}{16h} + \frac{R^3}{8h^3} - \frac{45R^4}{256h^4} - \frac{R^5}{16h^5}} \tag{2.13}$$

with drag coefficient γ, height of sphere midpoint h, sphere radius R,

This law is experimentally verified for particles on pluronics F127 adsorbed substrates, which is similar to the case of our experiments. This is shown in Figure 2.11.

As the particle becomes trapped by force closer and closer to the surface, the lateral drag force approaches 3 times the initial drag force. This then becomes the drag force we use to calculate our force.

2.6.2 Particle Trajectories

For a substrate, we ran two experiments at two different thicknesses in order to verify the response of our substrate at varying positions. Images were taken by a high-speed, Phantom camera at two different sampling rates, due to the difference in manipulations rates for the

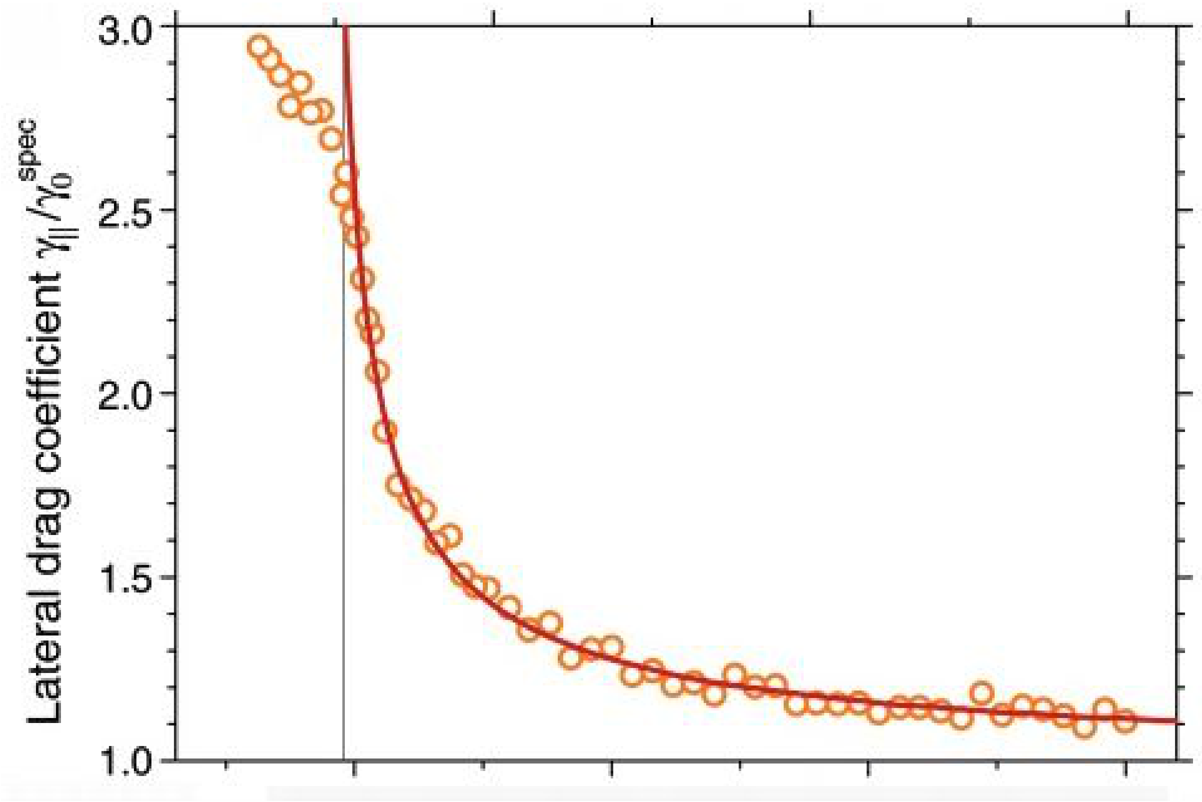

Figure 2.11: Faxen's Law is verified by optical trapping in the work of Schaffer [62].

two thicknesses. For the 5.3 μm thick resin we sampled at 2000 images per second, while for the 2.5 μm thick resin we sampled at 5000 images per second, using a 40 objective, and an added 1.5x modifying piece. Due to the fact that our magnet cannot be directly applied behind our substrate, as this would preclude our vision of the particles, the magnet is applied so as to barely allow light. The magnetic field generated by this position was estimated to be around .1 Tesla, and upon simulation, yields around half saturated magnetic elements, or half the typical gradient generated by these elements as typical. The general trajectories for our samples are shown in Figure 2.12.

2.6.3 Extracting Force

The experimental magnetic force is extracted directly by numerically extracting the velocity of the bead at different positions. The simulated force is generated by placing a test bead

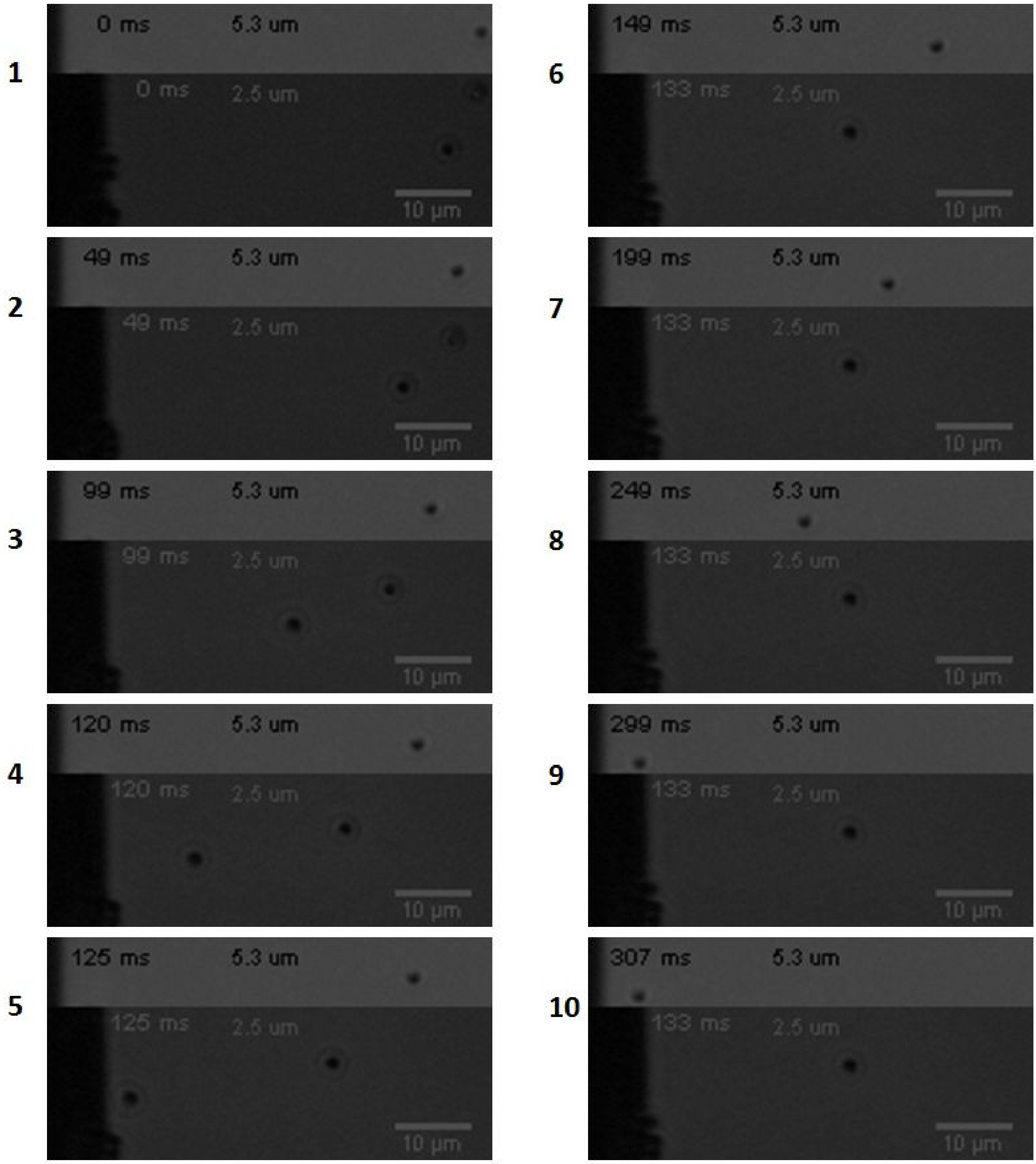

Figure 2.12: Particles under different forces due to varying resin height are manipulated at significantly different rates.

along the x-position of the substrate in the extrapolated x-z gradient mesh that was determined from comsol for this particular substrate. Comparison results of the trajectories of various particles on incident field with our FEM extrapolated force is shown in Figure 2.13.

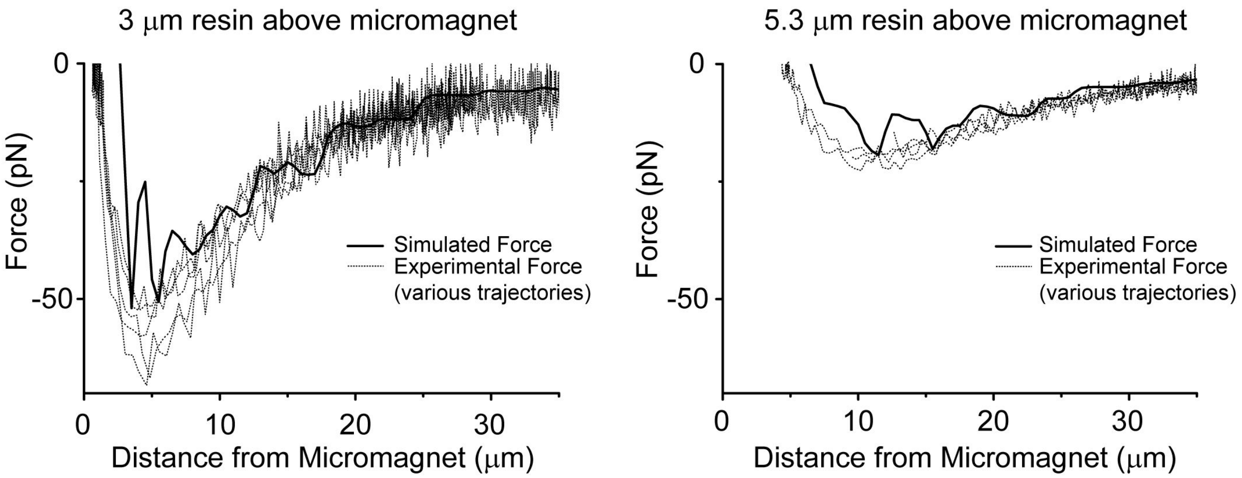

Figure 2.13: The experimental force over the range of the substrate shows strong agreement to our simulated force until the peak of the magnetic potential minima is crossed. Our substrates are designed to operate towards the right of this peak.

Our experimental force shows strong agreement over the relevant range of the substrate (to the right of the magnetic field valley), as our substrates are designed to operate at these points. We ascribe the error in measurement to be from a variety of possible sources, including the exact iron content of the magnetic elements used to characterize this measurement, the exact field generated at our stimulating position, and asymmetry in our application of the field. Despite this, the strong agreement in field gives us good reason to use our finite-element models as viable descriptors of the force generated by our micromagnetic elements.

2.6.4 Perturbation Analysis

We complete our analysis of the force generated by our substrates by introducing simple perturbation analysis to analyze the stability of the response upon the variation of several important parameters. The standard "test" volume is placed in our simulated response, as shown in Figure 3.2.

Various parameters are then modified to discern the stability of our measured force to inaccuracies in measurement. These are shown in Figure 2.15. Variation of the magnetic

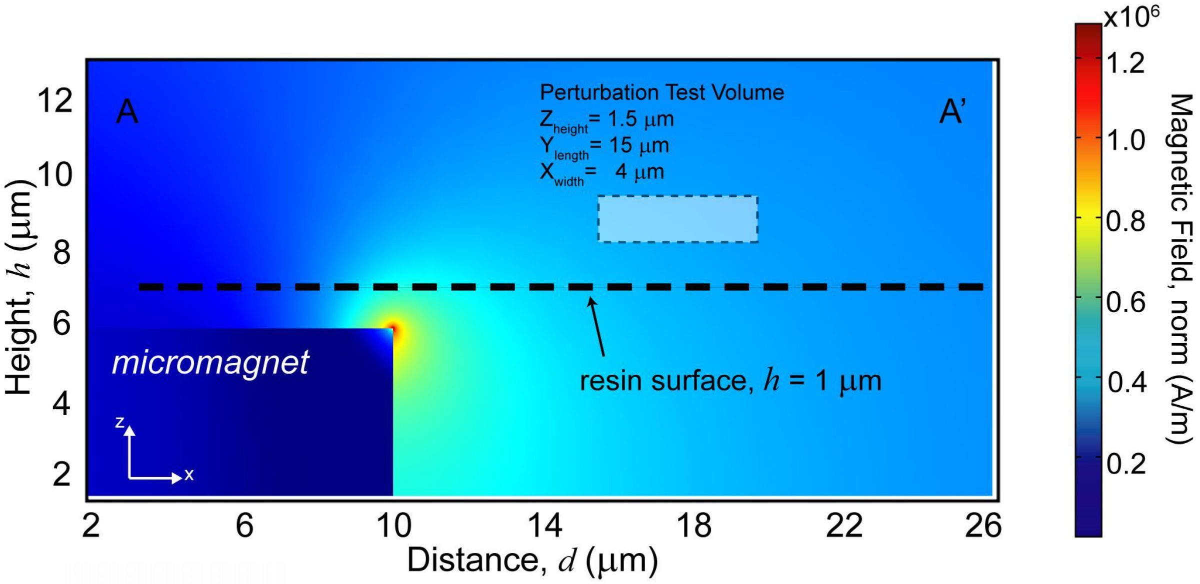

Figure 2.14: Test volume placed adjacent to our magnetic element of perturbation tests.

saturation of .03 T (around 2-3 percent variation in iron content, higher than the peak variation in a single sample) yields below 3 percent change in the final calculated force.

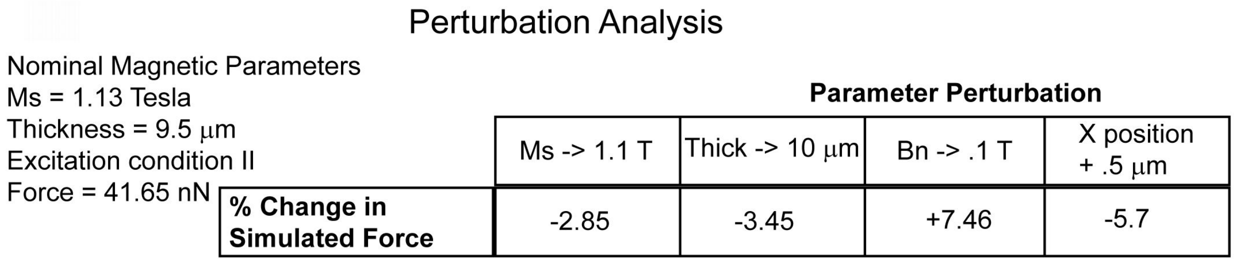
Perturbation Analysis

Nominal Magnetic Parameters
Ms = 1.13 Tesla
Thickness = 9.5 μm
Excitation condition II
Force = 41.65 nN

Parameter Perturbation

	Ms -> 1.1 T	Thick -> 10 μm	Bn -> .1 T	X position + .5 μm
% Change in Simulated Force	-2.85	-3.45	+7.46	-5.7

Figure 2.15: Resulting measured force shifts upon variation of substrate and measured parameters.

Variation of the measured thickness and nanoparticle cluster location by 0.5 μm yields 3.5 and 5.7 percent difference in calculated force respectively. Finally, the variation of the normal incident magnetic field to .1 T (corresponding to an x-y shift in the magnet position by 1 cm) yields a variation of 7.5 percent. This is due to a shift in angle of the incident fieldbecause the micro-magnet is essentially saturated, it is highly stable to z direction shifts in external magnet position.

2.7 Micromagnets in Interacting with Cells

The high accuracy and stability of a micro-magnetic approach to generate forces compares favorably to AFM, micropipette, and bulk-scale magnetic force generating approaches. This should be expected, as fields generated from singular elements can be precisely characterized, and the Maxwell's equations used to simulate such fields is linear, and the Finite Element Method used by various multiphysics platforms is easily able to simulate such fields. This is in comparison to approaches such as AFM, which typically has highly nonlinear responses as tips and substrate deform, micropipette, whose force vary strong with variable tip size, and more bulk-scale magnetic approaches, where exact gradients can be unknown.

CHAPTER 3

Fabrication

The development and execution of MEMS microfabrication processes is a fairly timely procedure. This difficulty scales with an increasing number and type of layer; indeed, layers must be physically compatible, exhibit minor stress mismatches, strongly adhere, and remain attuned to the process capabilities of our nanolab.

Our substrate fabrication can be decomposed into 3 major sections:

1) A magnetically active ferromagnetic layer. This is the layer with which outside, dynamically modifying magnetic fields can interact to generate strong, localizing magnetic field gradients at the micron scale.

2) The biologically compatible polymer layer, or the layer upon which cells will stabilize and traverse.

3) Physically adsorbed protein and cell-blocking layers which will essentially encode the surface for cell interaction, and rejection.

3.1 Layer Considersations

We begin by describing some of the logic of the fabrication choices made during our conceptualization of our process steps.

3.1.1 Magnetically-Active Layer

In forming the magnetic portion of the substrates, there are several base concerns to address, primarily encompassing material parameters of the magnet layer.

3.1.1.1 Magnetic Saturation

The most important material property required for our substrates is a high saturation magnetization. Because we can control magnetic fields off-chip with strong permanent magnets, a high saturation magnetization means we can increase the local fields that are generated on-chip by our individual elements. There is, however, a limit in certain special cases such as our first approach, where we would like to saturate the magnetization of elements to allow for dynamic manipulation and high precision control of magnetic nanoparticles. Because the elements must be saturated to achieve asymmetry in the potential minima around our elements, the saturation magnetization should be only a 2-4 times higher than our highest achievable permanent magnet field.

Commerially bought NdFeB permanent magnets typically generate up to 0.5 T at maximum (the remnance of thin NdFeB films, can achieve up to 1.4 T, however these decay and settle to significantly lower values over time), so this limits our saturation magnetization for our first approach at around 1.2 to 1.5 T. For our second approach, wherein a single element generates our magnetic fields, the saturation can be arbitrarily high to achieve as high of a coalescing force as possible.

3.1.1.2 Magnetic Remnance

Depending on application, the magnetic material could be desired to be soft or hard. Soft magnetic materials have a low magnetic remnance, and are characterized by BH-loops that closely approximate a single line, as little to no field is required to demagnetize the sample and remagnetize the magnetic element in another direction. Hard magnetic materials show significiant hysteresis, and the magnetization of the material depends strongly on the past incident magnetic field.

For current applications, where we want to dynamically manipulate nanoparticles, or apply and release force stimulation on cells, it is preferable for the material to be extremely soft, so the magnetic gradients can be reset with much higher ease. Despite our current needs, one can imagine substrates which need only be excited once to latch the substrate

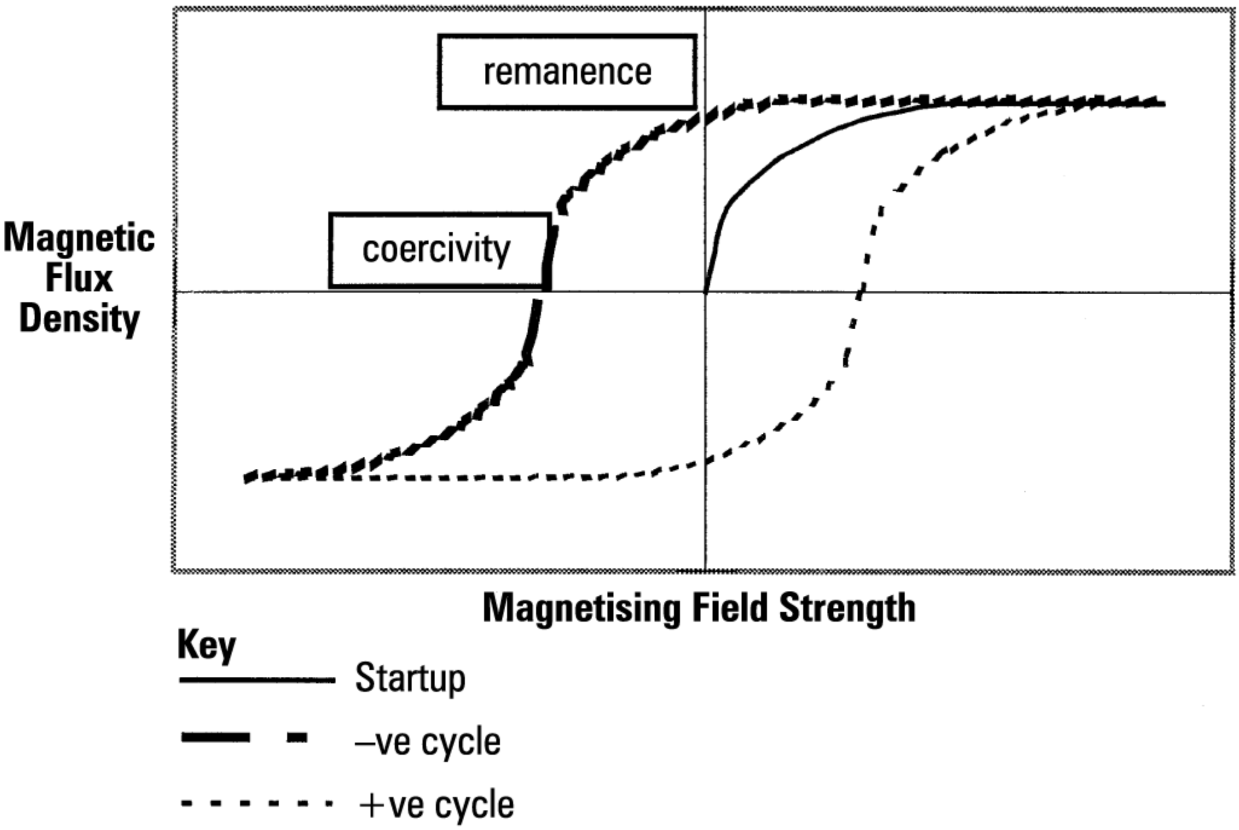

Figure 3.1: Standard BH loop for a hard ferromagnetic material. The induced magnetic field displays hysteresis depending on the previous excitation of the magnet. Large induced magnetization at 0 field, and large field required to zero the induced magnetic field of the material indicates high magnetic remnance and high magnetic coercivity respectively.

permanently in a magnetic state, without need for a constant magnet nearby.

3.1.1.3 Ease of Integration

A multitude of thin film magnetic materials have been demonstrated in MEMS, everything from the most basic Nickel films to thick NdFeB films. In multilayer processes such as the one we are employing, it is highly preferable that the layer been low-stress, and ideally possesses a low temperature, highly repeatable process step.

Ultimately, Ni_xFe_y alloy presents an excellent choice for our ferromagnetic material deposition, as this material is low-stress, well characterized and attempted in MEMS devices, and can be tuned (through modifying respective Ni and Fe concentrations) to have higher magnetization and lower remnance, depending on needs. At nominal values it has a saturation of 1.13 Tesla, which is right in our required range of operation. Our lab already has extensive experience in depositing $Ni_{70}Fe_{30}$, so this was chosen as our default material.

3.1.2 Polymer Layer

Over the lifespan of the project, a multitude of interfacial layers have been attempted to varying degrees of success. For MEMS designers, SU-8 is nearly always the resin of choice for interfacing with biological materials. SU-8 is not strictly bio-compatible, while the cross-linked resin itself (composed nearly exclusively of carbon-carbon and carbon-oxygen bonds) is inert, the photoacid which is used to cross-link the material contains Arsenic, which is not biocompatible. SU-8 is fairly easy to render biocompatible with the addition of hard-bakes, and optional leeching steps to either remove the photoacid altogether, or render it inert. Initial tests verifying the capability of our substrates to dynamically modify the location of nanoparticles within cells utilized these manner of substrates.

As our experiments became more complex, we began to study the effect of stimulation on proteins in single cells, which requires sensitive fluorescent microscopy. We would eventually switch and reoptimize our process for the photoresist PSR, developed at UCI which is both biocompatible, and possesses low background fluorescence [63]. This would eventually allow us to study highly sensitive biological processes with our substrates.

Currently, for a set of experiments where we need a malleable substrate to measure cell traction, we have yet again switched our interfacing layer to weakly cross-linked PDMS, a biocompatible, low background fluorescence, and highly stable elastomer. The main drawback of this layer is its difficulty in stripping and removing. However, these layers allow us to controllably achieve soft material (under 50 kPa), at well-controlled thicknesses through spinning.

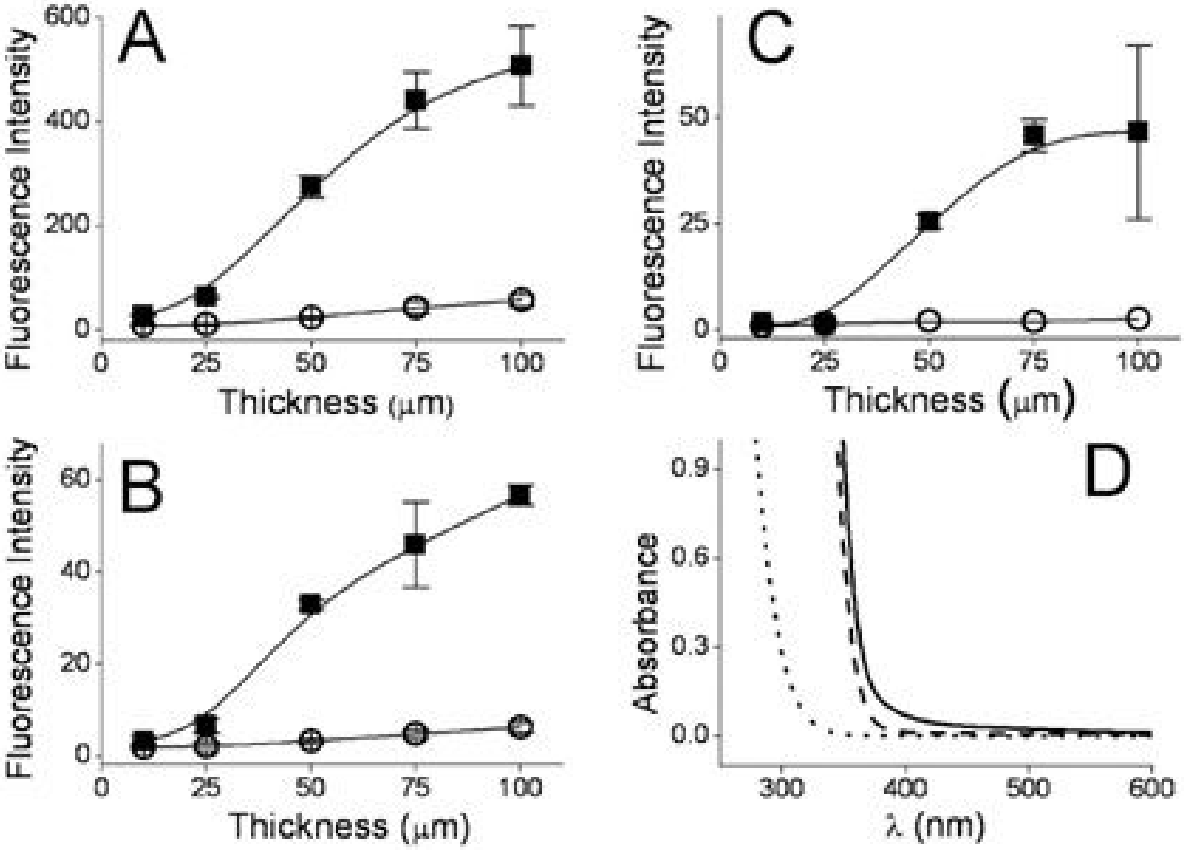

Figure 3.2: Comparison between fluorescence of SU-8 resist and PSR resin. A, B, and C compare the fluorescence intensity of FITC, TRITC and Cy5 channels, respectively.

3.1.3 Protein Patterning and Blocking

Our substrate must effectively pattern and delineate cells in order to form our desired experimental conditions.

3.1.4 Protein for Cell Adhesion

A variety of proteins and amino acids are used to encourage cellular adhesion.

3.1.4.1 Poly-l-lysine

Poly-l-lysine is a polymer of the amino acid lysine, an amino acid with an -R group terminated in a charged amino group. This positively charged amino group is what typically what 1) helps stabilize serum proteins, 2) encourages adhesion of ECM proteins to the substrate, and 3) attracts negatively charged cells to adhere onto the substrate. Poly-l-lysine, however, does not strictly compose extracellular matrix, and does not activate integrins, which are responsible for generating focal adhesions to the cell substrate [64, 65]. As the vast majority of mechanotransduction experiments is dependent on the consistent development of these adhesions, we choose not to use this as our cell adhering layer.

3.1.4.2 Collagen

Collagen is the most abundant protein in ECM, and forms the majority of connective tissue in animals. Unlike lysine, it directly binds to integrins, and encourages the formation of focal adhesions, so adsorbed collagen is linked directly to cells. This makes it a better candidate than lysine based substrates for mechanical studies.

3.1.4.3 Fibronectin

Fibronectin is a ubiquitous glycoprotein that binds integrins and collagen, and plays major roles in a large variety of cellular processes, including cell adhesion, migration, and more. It is secreted directly from cells and plays a critical role in a healthy biological system. It is very easily solubilized (unlike collagen that typically requires some heating and dissolution), and adsorbs simply onto hydrophobic surfaces.

3.1.5 Protein Blocking

In order to force cells into specific shapes and patterns, the counter pattern must be composed of protein and cell-rejected layers. This is nearly exclusively accomplished with use of polyethylene glycol (PEG) layers [66].

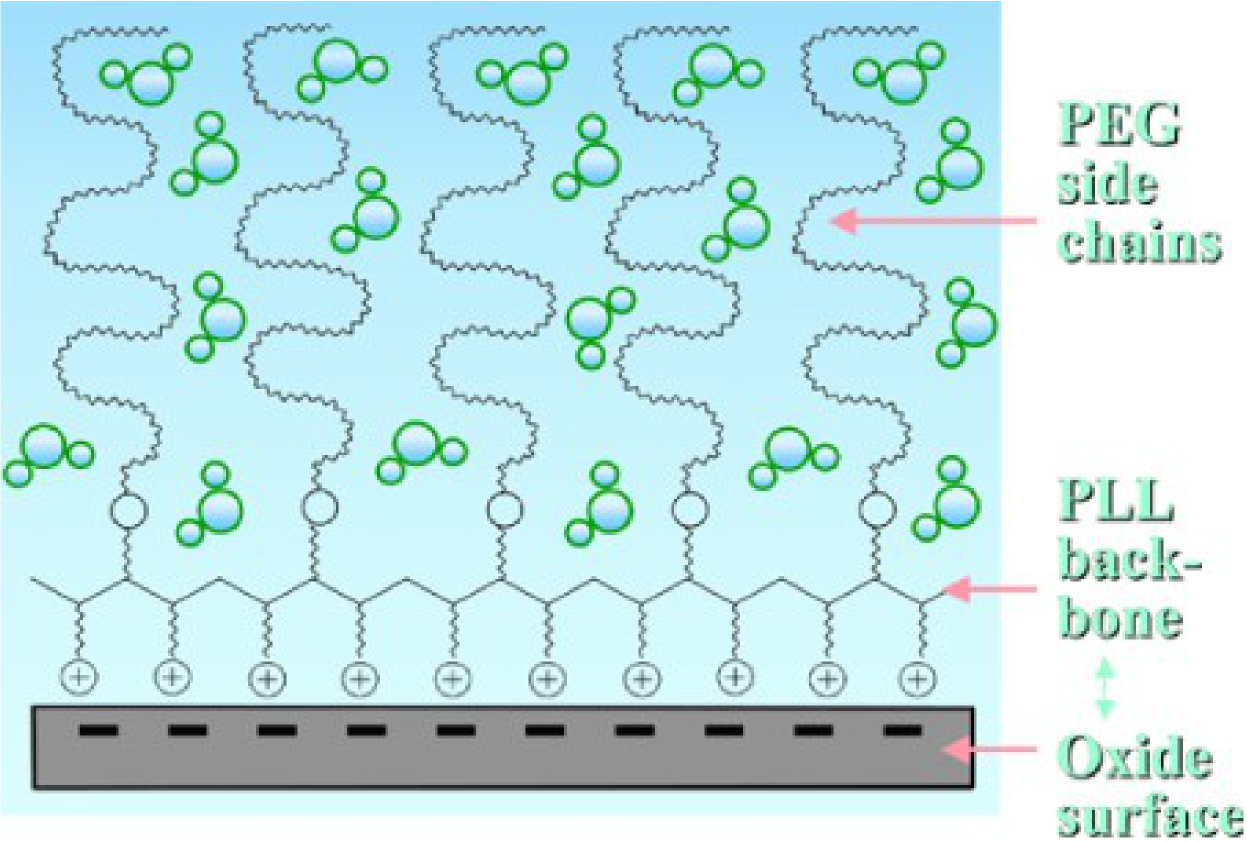

Figure 3.3: When adsorbed onto a surface, PEG forms a distinct brush-like structure that rejects water and proteins [66].

PEG is adsorbed onto substrates through either poly-l-lysine-PEG, which adsorbs onto hydrophilic surfaces, or various types of pluronics, which adsorbs onto hydrophobic surfaces. The distinguishing characteristics between these molecules is the backbone used to polymerize the PEG, which determines to which surfaces the molecule will adsorb.

3.2 Process Details

Here we explain in detail the notable processes used to fabricate our substrate.

3.2.1 Permalloy Deposition

Permalloy is one of the most common magnetic materials used in micromachining, and has been notably used in the work of Allen, Ahn, in the first magnetic switches, and in magnetic recording heads. The popularity of the material stems from the high permeability of the material-yielding large moments from low fields, the low remnance of the material — for repeatable performance, and low magnetostriction. Permalloy is the simulatenous deposition of Ni and Fe at the ratio of 80 % Ni and 20 % Fe. The reactions that occur at the counterelectrode are:

$$\begin{aligned} \mathrm{Fe}^{2+} + e^{-} &\rightarrow \mathrm{Fe} - E_0 = -0.417 \text{ V vs NHE} \\ \mathrm{Ni}^{2+} + e^{-} &\rightarrow \mathrm{Ni} - E_0 = -0.257 \text{ V vs NHE} \end{aligned} \tag{3.1}$$

One might note that the lower STD potential of Fe in comparison to Ni, meaning it is more reactive. This action runs close to intuition, as we know pure iron rusts rapidly in air. However, this also means that if we were to plate the two, we would expect more Fe to be evolved. This type of evolution is, of course, counter to the ratio we desire. In order to plate our wanted ratio, the general strategy is to plate at a low rate, thus making the electrochemistry mass-transfer limiting, which would then be proportional to the percentage of iron and nickel in solution. This requirement is also what makes it so difficult to plate properly.

Its relative success as a material underlies the difficulty in plating a repeatble, uniform layer. Current crowding near the edges of the mold — due to the nonuniform electric field — and clumping at edges — the slow plating rate allows material to gather near the edges of the mold — results in often harsh winging at the device edges. Most previous magnetic MEMS devices feature long and wide structures and out-of-plane motion, this type of features supplies the most force for these types of devices. This configuration means winging that occurs as a result of current crowding at the edges of structures are less critical to device performance due to their relative size in comparison to the total device. In-plane actuation runs counter to this logic, as armatures must be relatively slender in order to reduce the spring constant. The need to deposit a dielectric directly over the device also places limitations on our permalloy layer as dielectric deposition over bumps is slower and less uniform than that over a smooth plane.

3.2.1.1 Plating Agitator

Clearly, agitation is the preeminent factor in plating the uniform layer we need to properly fabricate our device. Proper agitation would ensure uniform movement of material through the structures, ensuring no spots where ions can gather. Agitators generally are comprised of 4 main types:

(1) Oscillating grid
(2) Pressurized nozzles
(3) Ultrasonic
(4) Moving wafer

The easiest of these to implement within our setup ended up being an oscillating grid. Upon review of existing designs from literature, an agitator was custom designed to fit within our specified plating setup.

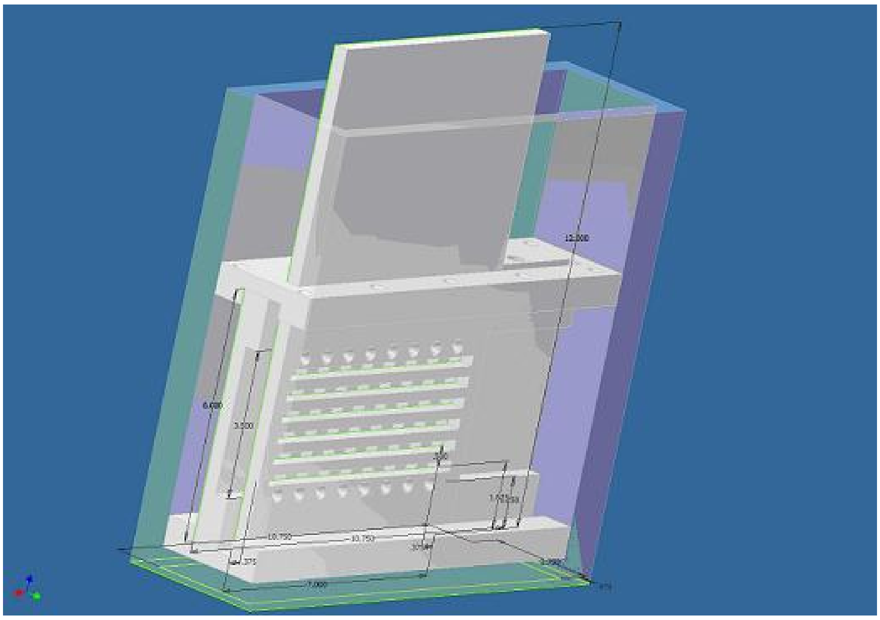

Figure 3.4: Schematic of the agitation system for the plating bath.

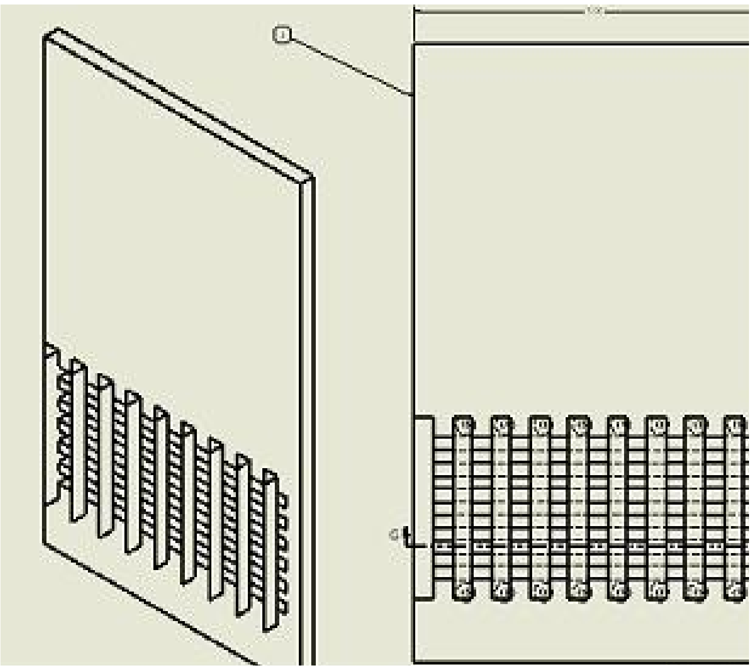

Figure 3.5: View of the fins running across the wafer. While wiping, the fins encourage the entrance of fluid from one side and subsequently out the other side.

The finalized agitator is comprised of two fitting sections, a wafer chuck, and the wafer chuck housing/wiping grid. The wafer is fitted with an insulated wire and copper tape, and set into the wafer chuck by two offsetting blocks. This chuck is then installed behind a wiping grid and the Nickel electrode compartment. During plating, the wiper oscillates in front of the wafer at 20 rpm. The idea behind the agitator is that as the fins wipe over the wafer, water will flow in one side and then be forced out the other, ensuring a constant supply of material to and from the wafer. Various wiping speeds were tested, there is a sweet spot in speed that is not so slow as to barely allow movement, but not too fast as to not allow any time for the material to move.

Typically, with our agitator, we are able to obtain less than 5 % variation in permalloy thickness across a single structure, greatly easing constraints on the top dielectric layer of our device.

3.2.2 Polymer Layer

Depending on the needs of the process, the polymer layer processing can undergo quite a few transformations

3.2.2.1 Etching

In cases where high accuracy in thin film thickness is needed, the polymer resin layer can be spun on as normal, and then etched back. This process has the effect of increasing long range planarity (features above 4 μm), and causing high nanometric surface roughness whose intensity increases with etch-time. For SU-8, PSR resist, and KMPR resins, a recipe of 85 % O_2 and 15 % CF_4 plasma RIE optimizes etchrate. Higher oxygen content typically increases the surface roughness, while higher fluorocarbon will begin cross-linking the resin significantly (the emission tends more strongly towards the ultraviolet). Increasing etch-time significantly increases the background fluorescence of resins due to UV curing, and should typically be minimized.

3.2.2.2 Hydrophobic Recovery

Etching the resin with oxygen plasma significantly increases the wetting of the substrate, as the hydrophilicity increases with the increasing exposed oxygen groups generated by the plasma. For the purposes of cell-patterning by adsorption, the surface must be made hydrophobic again. There are several ways of accomplishing this:
1) CF_4 plasma (only for extremely short oxygen etches),
2) High heat or greater than 1 month wait time,
3) Depositing a thin film (parylene or diluted resist solution), or
4) Silanization.

The third and fourth options yield the best results, with the silanization option being the easiest to execute. Octadecyl-trichloro silane is highly reactive with hydroxide groups, and yields robust hydrocarbon chains on the surface, creating a strong hydrophobic surface.

200 μL silane is dissolved in 15 mL hexanes and placed in a petri dish. The sample is then submerged for under 5 minutes (varies depending on the hydrophilicity of the substrate), before being washed in hexanes, and subsequently isopropanol and water. This sample can be tested under running water to verify its hydrophobicity.

3.3 Process Flow

Shown in Figures 3.6 through Figure 3.12 is our process flow.

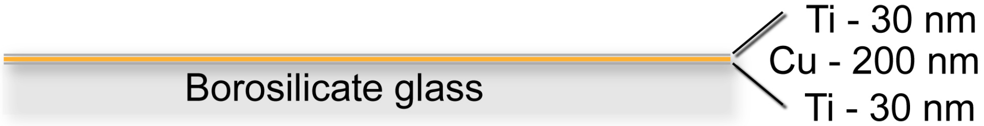

Figure 3.6: Step 1: We begin with glass slides (purchased from Fisher Sciences), which are cut in half, and cleaned in piranha and oxygen plasma (Tegal Asher, 200 W, 5 min). Ti/Cu/Ti seed layer is deposited to thicknesses of 30 nm / 200 nm / 30 nm in a CHA evaporator.

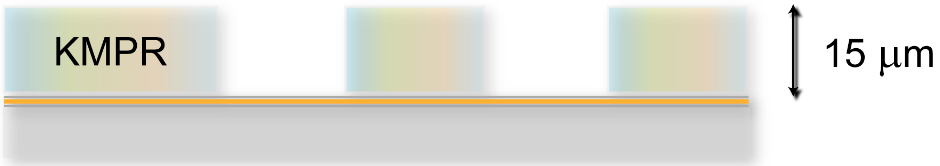

Figure 3.7: Step 2: KMPR photoresist (1005 or 1010 depending on required thickness), is spun and processed to form openings through which nickel-iron alloy will be electroplated. Sample is oxygen-plasma cleaned in either Technics RIE (200 W, 1 min), or Tegal Asher (200 W, 1min, 100 C) to ensure clear opening.

For our periodic micromagnetic substrates, the PSR layer is replaced with SU-8, and placed in oxygen plasma (200 W, 30 s) instead of adsorbed with fibronectin. This provides a more MEMS fabrication lab friendly process with a standard photoresist and simple plasma step to encourage cell adhesion.

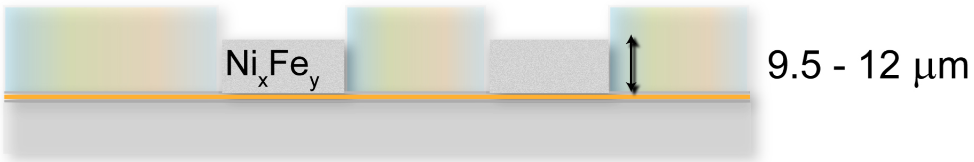

Figure 3.8: Step 3: Nickel-Iron alloy is electroplated using a custom-designed setup, at a current of 1 mA for 2 to 2.5 hours to generate desired thickness.

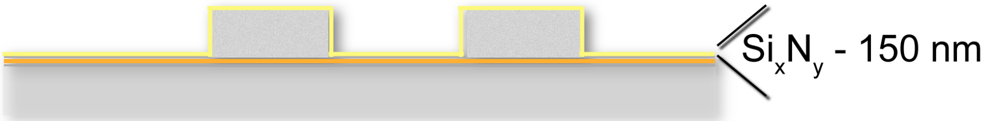

Figure 3.9: Step 4: KMPR electroplating mold is stripped in Aleg-355 or Aleg-380 photoresist stripper over 30 minutes at 75 C. The seed layer is etched first in 1 % hydrofluoric acid, then in 5 % acetic acid / 15 % hydrogen peroxide, and again in 1 % hydrofluoric acid. The metal layer is finally passivated with 150 to 200 nm of PECVD Si$_x$N$_y$ at 300 C.

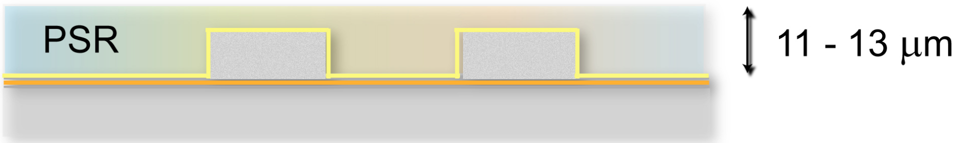

Figure 3.10: Step 5: For our force substrates, PSR resist is spun with a ramp of 500 rpm/s, baked under ramping conditions for 20 minutes from 65 to 95 C, 55 second exposure dose, hard baked for 6 minutes at 95 C, and cured at 120 C for 12 minutes.

3.4 Magnetic Nanoparticle Fabrication

Standard magnetic nanoparticles do not internalize rapidly into cells, and are only internalized slowly through phagocytosis. Several other internalization methods are significantly

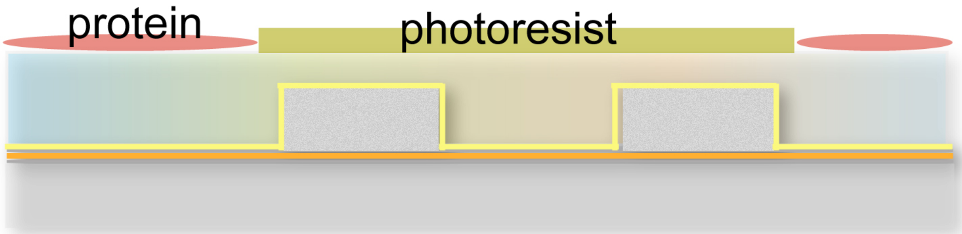

Figure 3.11: Step 6: Photolithography step with AZ5214E, spun at 5000 rpm, and exposed for 10 seconds at 11 W / cm^2. Fibronectin (25 μg/mL) is adsorbed onto the surface for 3 hours, and photoresist is etched away in ethanol for 1 min (10 s in ultrasonic bath).

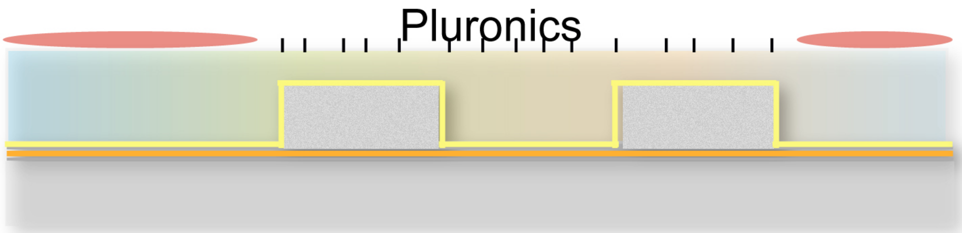

Figure 3.12: Step 7: Pluronics F127 (1 % w/v) is adsorbed onto the surface for 45 minutes.

quicker, such as endocytosis. Endocytosis can be encouraged by increasing the positive charge on the particle, which encourages adsorption onto the cell surface and subsequent internalization. High quality (high magnetic saturation, non-toxic) nanoparticles are typically not fluorescent.

The simplest method to acheive both these goals is through amination of magnetic nanoparticles, as amine groups not only important stable positive charge to the particles, but also introduce active reaction spots with which fluorophore can be reacted.

A simple diagram of the process is shown in Figure 3.13.

The process essentially begins with dextran polymerized particles, which have their hydroxide groups deprotonated by addition of a strong base. This deprotonation activates the hydroxide for attack of epoxide group of a heterolinker (epichlorohydrin). Ammonia, in the

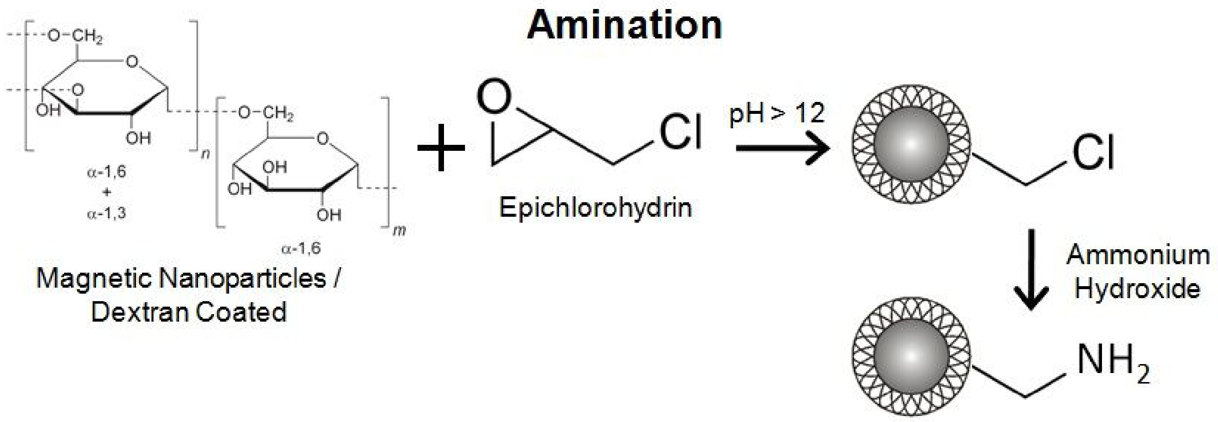

Figure 3.13: Dextran sugars can be aminated through reaction with epichlorohydrin and subsequent immersion in ammonium hydroxide solution.

form of ammonium hydroxide, replaces the chloride group, and we are left with aminated magnetic nanoparticles.

The exact process is as follows. 1) Nanomag -D dextran magnetic fluorescent nanoparticles (-plain, 130 nm, micromod, Germany) is immersed with 10 M NaOH and epichlorohydrin (Sigma) at a ratio of 41 % colloid, 25 % NaOH solution, and 33 % epichlorohydrin. This is vortexed extensively, and reacted for 24 hours on a shaker, covered in aluminium foil. 2) At the 24 hour mark Ammonium Hydroxide solution (33 % w/v) is added so that this solution composes 25 % (v/v) of the final volume of total solution. This is again vortexed extensively and reacted for 24 hours inside aluminum foil. 3) Upon completion, this solution is dialyzed in 50 kDa MW dialyzing bag for at least three days. 4) Upon completion, the particles are captured overnight by a permanent magnet, and the buffer is changed from DI water to bicarbonate buffer (pH = 8.3), and the particles are diluted back to the initial concentration of the colloid. At this point the particles are aminated, and ready for further conjugation.

The particles are nominally stable at this high pH if stored at 4 C for at most 3 months, however, as time passes, the amine groups and magnetic nanoparticles begin to degrade. In order to impart fluorescence, these particles are reacted with alexa-fluor 488 (green), 568 (red) or 647 (deep red). We found all these particles to internalize rapidly inside cells, and impart equivalent responses on heLa cells. We typically react .5 μL of fluorophore (10 mg/mL), per 300 μL of magnetic nanoparticle colloid overnight. The particles are checked for brightness (there is some variability in the number of attached amine groups), and the particles are re-reacted with additional fluorophore as necessary.

Upon reaction completion, the particles are separated under magnetic field and washed 5 times in phosphate-buffered saline solution. The solution is finally heat treated at 50 C for 10 minutes, before final vortexing, and storage at 4 C.

Amine groups can be coupled through a variety of biomolecules through EDC-NHS reactions, opening up the possibility to generate bio-active magnetic fluorescent nanoparticles with fairly straightforward chemical reaction.

CHAPTER 4

Biological Methods and Analysis

In this chapter we detail the methods used in our biological studies, and discuss our image processing techniques to extract parameters of interest.

4.1 General Sample Protocol

Here we outline the method with which we pattern, internalize nanoaprticles, and subsequently excite cells.

4.1.1 Cell Seeding

Several cell lines have been used with our substrates, and these include MCF7 (breast cancer cells), HeLa (cervical cancer cells), and 3t3 (mouse fibroblast cells). These were all grown in a standard incubator at 37 C, 5 % CO_2, in humid conditions. The standard cell culture medium consists of high-glucose Dulbecco's modified essential medium, with 10 % fetal bovine serum, and 1 % pen/strep solution.

Cells are allowed to grow to no more than 30 passages before being trashed so as to maintain consistency is cellular response. Lab passage cells are grown in 75 mm^2 flasks, and are typically passed once a week.

For non cell division experiments, cells are grown to half confluency in 25 mm^2 flasks, and subsequently incubated with magnetic nanoparticles. For this we typically dilute 3 to 10 μL of modified magnetic-fluorescent-nanoparticle colloid into 3 mL of DMEM medium, and incubated for 20 minutes to 1 hour. This variation is due the variety in internalization strength of particles from run to run, as subtle variations in number of amine-groups and conjugated fluorophore affect the rate at which particles are internalized. Upon completion of the nanoparticle internalization process, cells are washed extensively in PBS, before being incubated in standard culture medium for 3 hours to allow the cells to rest before beginning the seeding process of the cells on our substrate.

The seed process begins with washing cells three times with PBS, and incubating with Trypsine/EDTA for 3 minutes. Suspended cells are washed with culture medium and pelleted for 4 minutes at 3000 rpm. Cells are resuspended in culture medium, and pipetted directly above our substrates (immersed in culture medium). The samples is agitated until we acheive a cell quantity of approximately 10 cells per 100 μm^2. Cells adhere and subsequently spread over a 40 minutes time span. Typically, every 15 minutes the cells are checked under microscope and agitated so cells can resample the substrate pattern. Upon satisfactory inspection under microscope, the samples are washed in culture medium three times, and subsequently allowed to rest for another three hours.

Shown in Figure 4.1 is a diagram of this method.

4.1.1.1 Cell Division Experiments

Cells are grown to 25 % confluency in a 100 mm^2 flask, and serum starved over 48 hours. The cells are then given a double-thymidine (Sigma) block. This comprises a 2 mM treatment of thymidine for 18 hours, followed by a release for 9 hours, and a second 2 mM thymidine block for 17 hours. Thymidine arrests cells in pre-G2 phase, as excess thymidine inhibits the proper replication of DNA. Once cells are released for their second time, they proceed synchronously through G2 and mitosis. This type of synchronization allows the gathering of data from more dividing cells than normal.

4.1.2 Live-Cell Experiments

Live cell experiments were conducted in a lab-made incubator box surrounding our fluorescent microscope. 5 % CO_2 is fed directly to the substrate through a humidifier (bubbler), and the sample is heated to 37 C. Images are captured using the lab's inverted fluorescent

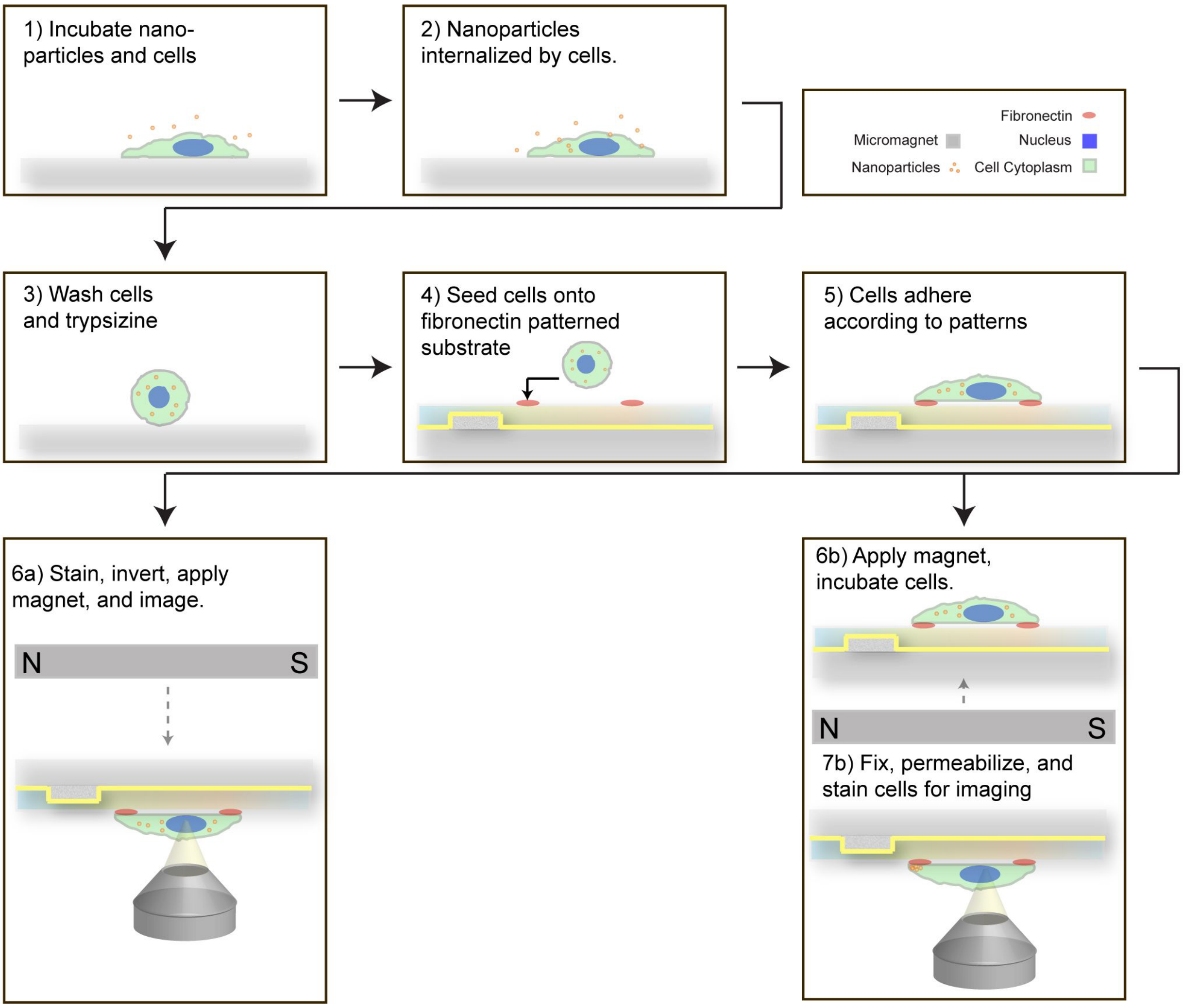

Figure 4.1: Generalized experimental protocol. Fibronectin patterns defined by photoresist become adhesive regions for cells. After nanoparticle dosing and cell patterning steps, both live-cell and fixed-cell imaging experiments can be conducted.

microscope (Nikon). A general diagram of this is shown in Figure 4.2.

4.2 Immunofluorescence

Once stimulation procedures are completed, cells are fixed in heated 3 % formaldehyde in PBS for 8 minutes at 37 C in the incubator. For fascin stains, cells are instead fixed for 5

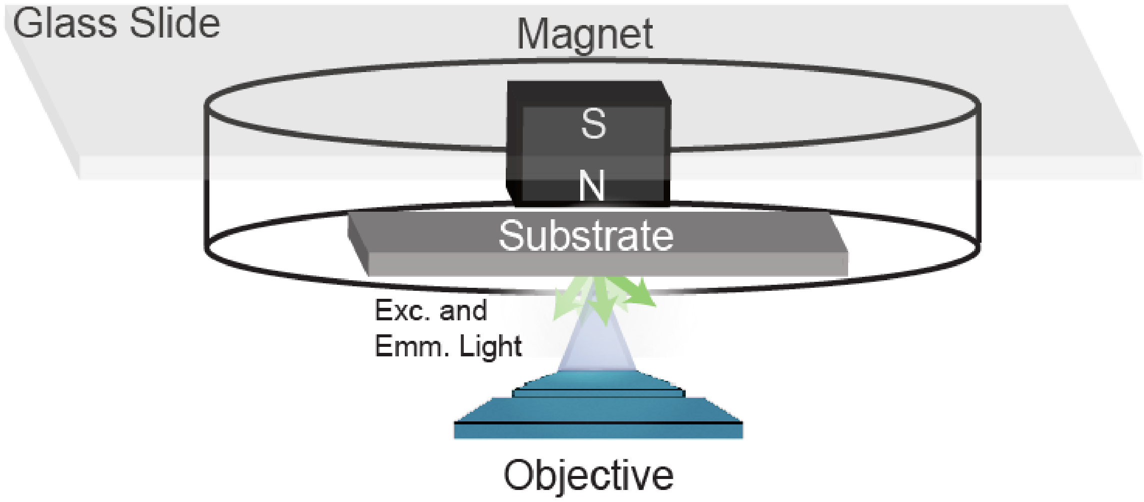

Figure 4.2: Imaging protocol for our live-cell imaging setup. A single large magnet is translated behind a petri dish to generate our desired operation mode.

minutes at -20 C in methanol, as formaldehyde denatures the fascin antibody binding site. Unless otherwise noted, cells are permeabilized in .5 % triton-x 100 for 10 minutes. Actin, not strictly an immunofluorescence stain, is stained with 12 μL phalloidin-alexafluor 488 in 3 mL of PBS for 20 minutes.

For immunostains, cell samples are blocked in 5 % bovine serum albumin for 1 hour, and permeabilization is done using tween-20 over a 30 minute timespan.

Beta1 integrin (Millipore), is incubated at 1 μg/mL at 4 C for overnight.
Phosphorylated-Tyrosine (p-tyr-100, Cell Signalling), is incubated 1:400 at 4 C overnight.
Myosin-X (Novus Biologicals), is incubated at 1:1100 at 4 C overnight.
Phospho-PAK (ser199/201, Millipore), is incubated at 1:400 for 36 hours at 4 C.

Samples are washed three times in PBS, and incubated in 1:500 in appropriate secondary antibody (alexa fluor 568-IGG) for 45 minutes.

4.3 Inhibitor Studies

We studied the following inhibitiors:

Streptomycin (1 mM, 2 hr-, Sigma), GSMTx-4 (25 μM, 30 min-, Sigma), EGTA (5 mM, 2 hr-, Sigma in Ca free medium) are inhibitors of calcium signalling in cells (stretch-activated channels are commonly implicated as an effector of cell mechanotransduction).
CK869 (30 μM, 1 hr-, Sigma) is an inhibitor of an actin nucleator in lamellipodia.
PP2 (20 μM, 1hr-, Sigma) is an inhibitor of SRC, and primarily focal adhesion kinase, a kinase involved in mechanotransduction of cellular focal adhesions.
Wortmannin (750 nM, 1hr-, Sigma) is a broad inhibitors of PI3K, PAK localization, PDGFR, and other kinases.
ML141 (10 μM, 1hr-, Tocris) inhibits CDC42, a critical protein in cell migration.
NSC23766 (100 μM, 1 hr-, Tocris) inhibits RAC, a critical mechanotransductive protein implicated in the degradation of stress fibers.
Axitnib (10 nM, 1hr-, Tocris) inhibits VEGFR, a major cell membrane receptor implicated in mechanotransduction.
PD98059 (50 μM, 1hr-, Sigma) inhibits MEK/ERK mechanotransduction pathways.
dasatinib (200 nM, 1 hr-, LC Labs), inhibits SRC, and c-abl (a mediator of some types of filopodia).
IPA-3 (30 μM, 30 min-, Sigma) inhibits PAK, a critical mechanotransductive protein implicated in the formation of filopodia.

These inhibitors were added to standard DMEM/10 % serum/penstrep medium at notated times before magnet application. Samples are then excited by magnet for 1 hour to 1 hour 15 min (varying with substrate thickness), before being fixed, stained, and analyzed as in previous actin quantification experiments. We chose shorter times for inhibitory experiments due to the tendency of some inhibitors to degrade over time. All of the above inhibitors are stable and reactive within the 2 to 2.5 hour time frame of this experiment, as determined from references.

Our inhibition experiments consist of simultaneously running mini-groups of samples, typically 2-3 samples with added inhibitors alongside a single standard sample in normal culture medium (with or without DMSO) as the control for the group. Inhibitory data is calculated as a percentage of this control response so as to normalize the response to a standard.

4.4 Image Processing

In our results, we attempt to discern the asymmetry of actin protrusions, and the biased cell division axis generated by high local tension. In order to do this, we have to properly numerically analyze our extracted images. In all our fluorescence experiments we capture blue (DAPI, cellular DNA), green (phalloidin-alexafluor 488, actin), red (fibronectin-alexa fluor 568, cell patterns), and deep-red (nanoparticle-alexa fluor 647, magnetic nanoparticles). Brightfield images are sometimes captured along with these, however they are only particularly useful for discerning the position of the micromagnetic element.

Large, stitched images are captured using an automated microscope stage on our inverted Nikin fluorescent microscope, and typically capture .5 μm^2 images. These images are subsequently cut into 6100 pixel by 6100 pixel images in order to obtain reasonably sized images that ImageJ and MATLAB can efficiently process. Images are parsed in MATLAB, and single, patterned cells are picked using a MATLAB script, and individual cell images, separated into each distinct channels, are numbered and stored into respective folders.

4.4.1 Analyzing Actin Asymmetry

For our actin experiments the images processed in order to improve accuracy in measurement. The images are processed in order as follows:

Deep-red channel, quantifying nanoparticles, has its background intensity substracted, and is transformed into an initial black-white image using the graythresh function.
Red channel, showing the fibronectin, has its background intensity substracted, and is transformed into a black white image with use of the graythresh and imadjust functions in MAT-

LAB.

Green channel, showing the actin, has its background subtracted. The green image is closed (image process where small features are effectively removed from the image) along the vertical or horizontal direction so as to remove protruding features. The edges are then discovered with a canny edge detector.

These images are all stored as separate images in the folder.

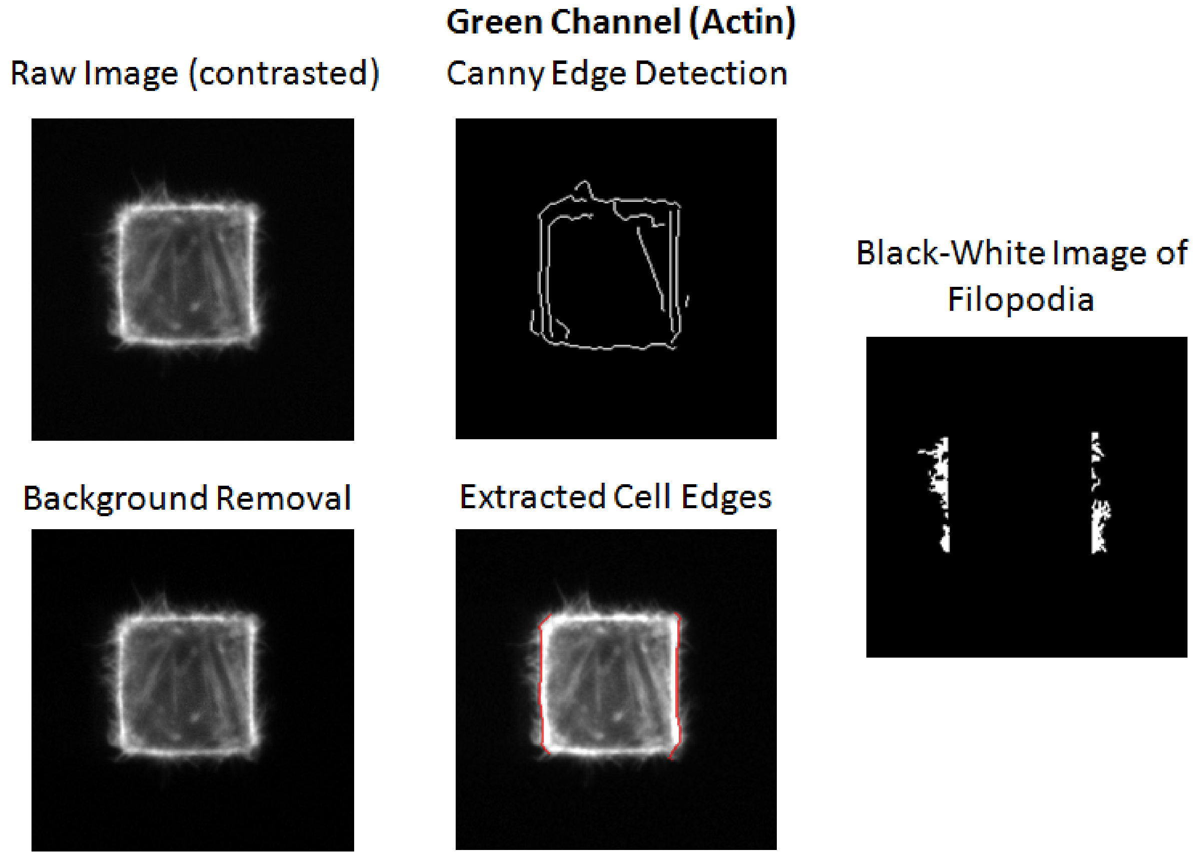

Figure 4.3: Images processing for the actin image. Image background is subtracted. The green image is closed (image process where small features are effectively removed from the image) along the vertical or horizontal direction so as to remove protruding features. The edges are then discovered with a canny edge detector.

The edge image is processed so as to isolate the four sides of the cell to lines. The code is imperfect, for example, cells with high quantity of protrusions will not properly isolate the side of the cell. This occurs with approximately 10 % of samples. Code was developed that connects edge points determined by the above code, and allows the user to effeciently manually correct the side image.

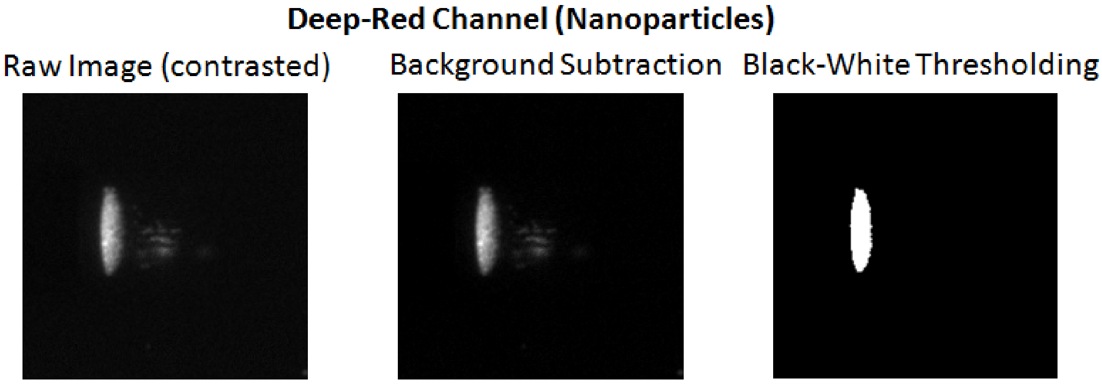

Figure 4.4: Images processing for the nanoparticle image. Background intensity substracted, and is transformed into an initial black-white image using the graythresh function.

Once the edges are correctly processed, the following parameters are extracted:
Pattern limits - from the fibronectin image.
Micromagnetic position - From brightfield image or DAPI image.
Midpoint - average of pattern limits.

With these parameters extracted, a black-white image following the protrusions of the sample is generated using imadjust and graythresh, as with the red and deep-red channel images.

4.4.1.1 Critical Parameters of Actin

Once the images and cell parameters are extracted, we proceed with determining the critical parameters of asymmetric actin. Our most important parameter is "actin asymmetry." This is defined as the average intensity of protruding actin (per unit length) over a range encom-

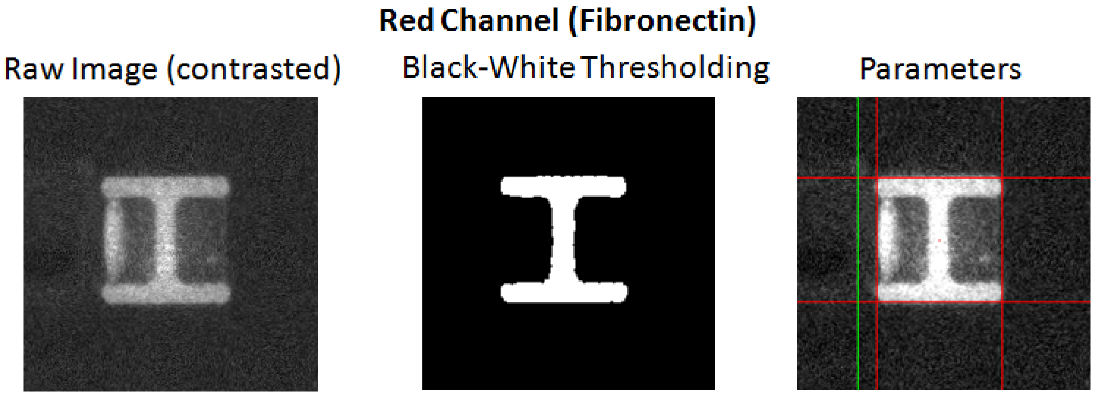

Figure 4.5: From the fibronectin image, the extents of the pattern are gathered for later analysis.

passing the nanoparticle length plus 4 μm, divided by the average intensity of protrusing actin over the other sides of the cell that are similar. By similar, we define as being the same type of cell cortex boundary. For the X pattern this is all the other sides of the cell, for the I pattern this is only the two horizontal stress fibers of the cell, as the top and bottom lines neighbor focal adhesions, and thus have different fundamental activity.

One other major parameter we quantify is actin correlation, which determines how the actin stress fiber line varies with incident force. This is accomplished by taking the pixel correlation of actin stress fibers to the flanking force at that pixel. A negative number would mean that at high forces, the stress fiber tends to decay, while a positive number would indicate that the stress fiber amplifies itself.

4.4.2 Cell Division

The preparation of samples for our cell division measurements is prepared in much the same way as our initial preparation for actin asymmetry. Large, stitched images showing the whole sample response of our samples are parsed, and single, dividing cells (whether pre or post-anaphase), are cropped and numbered for later analysis.

Dividing cells from a single sample are analyzed together using a custom matlab script. The fibronectin sample is used to determine the angle of the sample, and this is subsequently

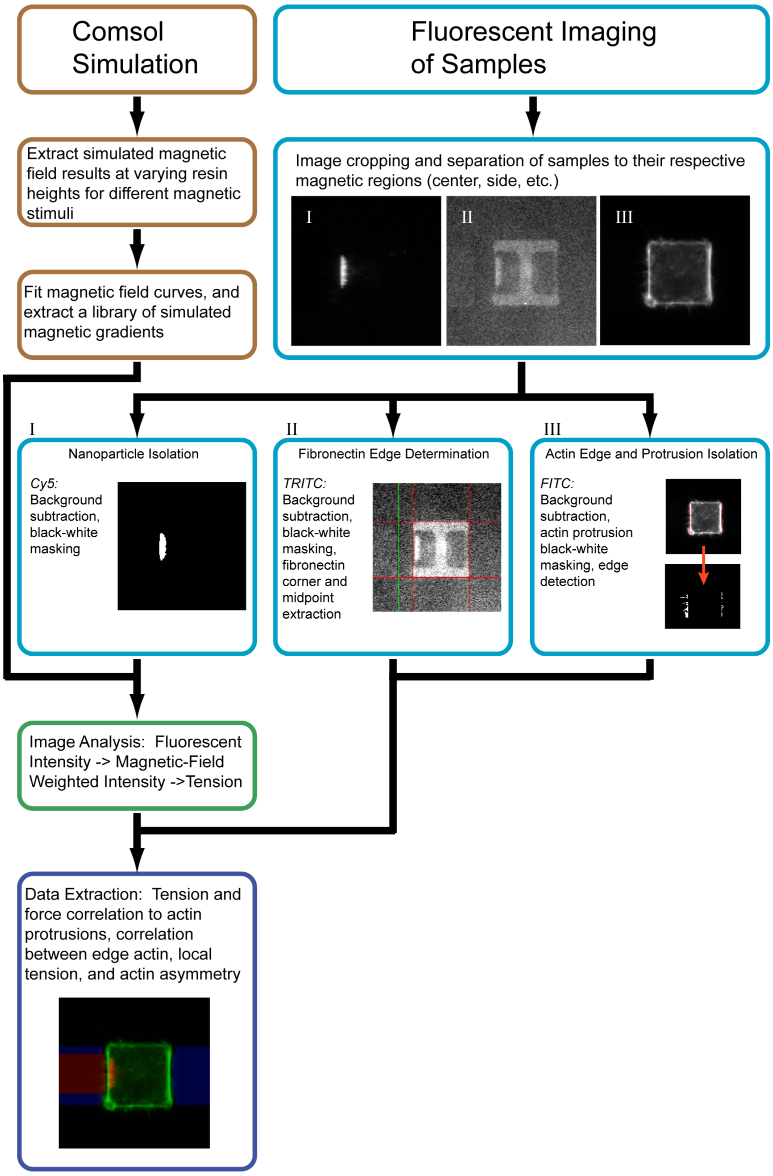

Figure 4.6: General flow diagram for our quantitative analysis of force-dependent actin polymerization asymmetry. Numerical simulation is separated into FEM analysis in COMSOL (as in Figure S2), and numerical analysis in Matlab. Widefield images are separated into fluorescent components and critical parameters extracted in order to quantify the effect of scaling tensions on local cellular actin. Black-white masking for important parameter calculations is performed to reduce noise.

used for the baseline angle for the rest of the cells. Each individual cells has a line drawn parallel to the angle of the DNA for cells in mitosis, or in the case of actively dividing cells, the line is chosen perpendicular to the DNA line.

In addition to quantifying the DNA angle, we draw a cropping box around the coalesced magnetic nanoparticles, and this is used to quantify the coalesced nanoparticles stimulating each cell.

This data is parsed and collected to comprise our final data.

CHAPTER 5

Results

In this chapter, we report on the capabilities of our two general approaches. First, the capability of our periodic magnetic substrates to dynamically generate and manipulate patterns of coalesced nanoparticles, and secondly, our magnetic-nanoparticle mediated forces in inducing large scale asymmetries in cellular behavior.

5.1 Periodic Micromagnetic Substrates

Through experimentation, we found our periodic substrates capable of dynamically patterning intracellular magnetic particles with high precision and repeatability.

5.1.1 Patterning Magnetic Particles in Water

We initially verified the feasibility of our micromagnetic substrates by executing simple patterns in water before progressing to working with cells.

We began by testing out the ability of our ferromagnetic dots to controllably localize particles to designed locations. Using our fabrication process, we spelled out UCLA and JUDYLAB, incubated our substrates with magnetic particles, and applied a magnet to see the response. This is shown in Figure 5.1.

For a magnet positioned directly underneath the substrate, particles clearly colocalize to positions directly above the ferromagnetic dots. We next attempted to verify the reversibility of our system. As the particles are paramagnetic (with a fairly low remnant saturation), and the ferromagnetic elements are made of magnetically soft $Ni_{70}Fe_{30}$, aspects of the magnetic system should demagnetize once the incident magnetic field is removed.

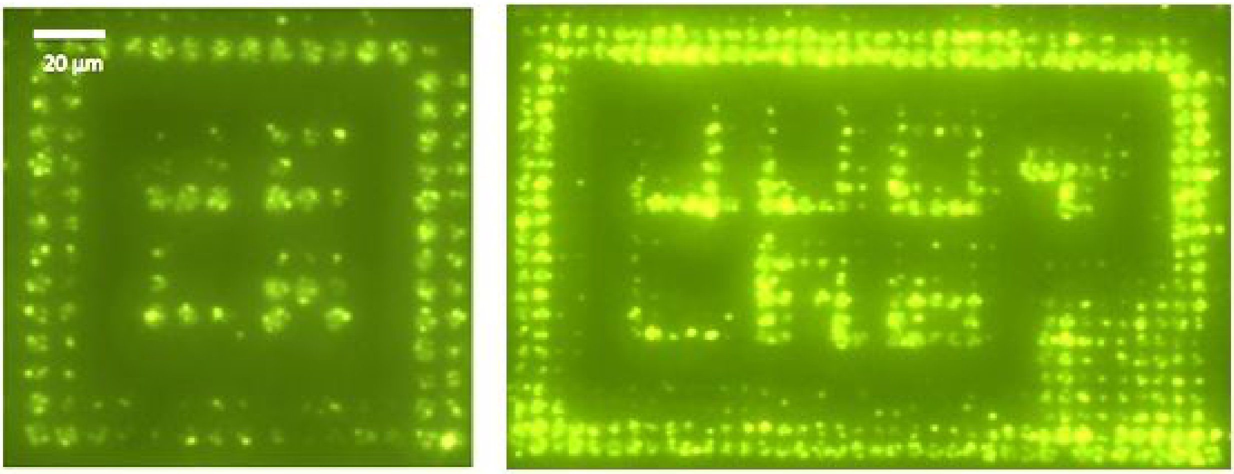

Figure 5.1: Magnetic-fluorescent nanoparticles are patterned by our ferromagnetic elements rapidly in DI water. Particles clearly localize to positions directly above the magnetic elements for a magnet applied directly underneath the substrate.

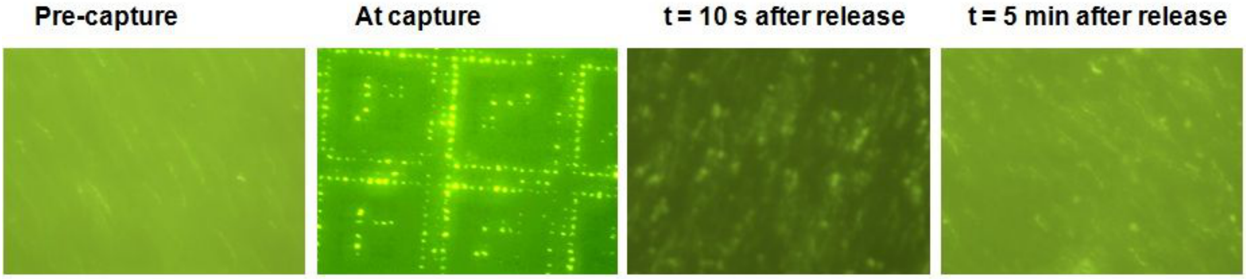

Figure 5.2: The disparate elements of our system are all magnetically soft, which means that the pattern generation is reversible.

As shown in Figure 5.3, removal of the magnet rapidly reverses the system, even under low fluidic agitation, and begins occuring immediately upon magnet removal. Withint 10 s the magnet particles have turned into disparate clumps, and by 1 min the system has completely reversed.

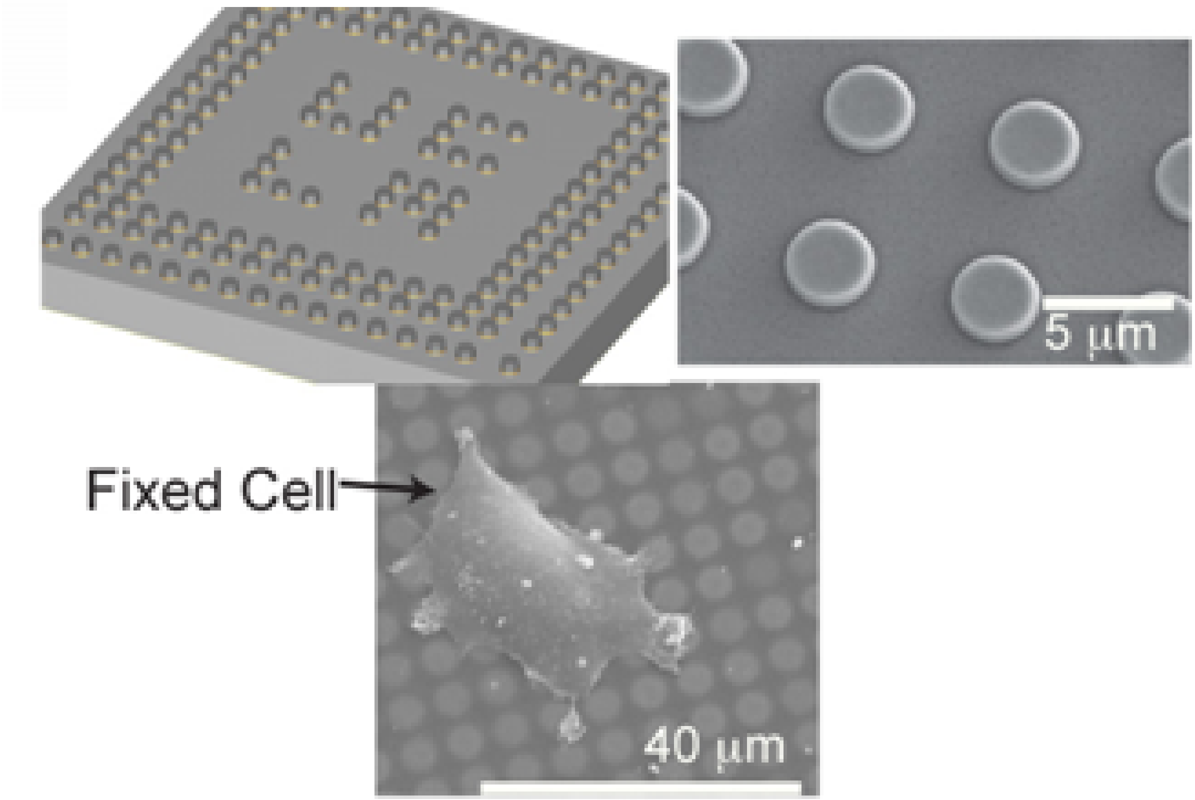

Figure 5.3: Shown are schematic of our substrate, and Scanning Electron Microscopy images of patterned ferromagnetic dots and a fixed cells above our substrate.

5.1.2 Intracellular Patterning of Magnetic Particles

Next we attempted studies on the ability to pattern magnetic nanoparticles in the intracellular environment. MCF7 cells were cultured in medium, and subsequently incubated with Chemicell magnetic nanoparticles overnight in a manner as generally described in our methods chapter (except at significantly higher concentrations as there are no amine groups on these particles). The cells were then seeded onto our substrate, and set in our incubator-fluorescent microscope setup for further study.

5.1.2.1 Intracellular Patterning of Magnetic Nanoparticles

We found that under magnetic stimulus, as in our water-based tests, the magnetic particles would coalesce to distinct positions inside the cellular space. We also found that the particles would organize to precise positions based exclusively on the orientation of the external magnet. Examples of these are shown in Figure 5.4. We found that the simplest method of verifying the location of the nanoparticles to be through the UV excitation, blue emission filter set. This is because the sample reflects strongly in the ultraviolet range, but that particle absorb strongly in this very range, creating clear contrast between the substrate and nanoparticles.

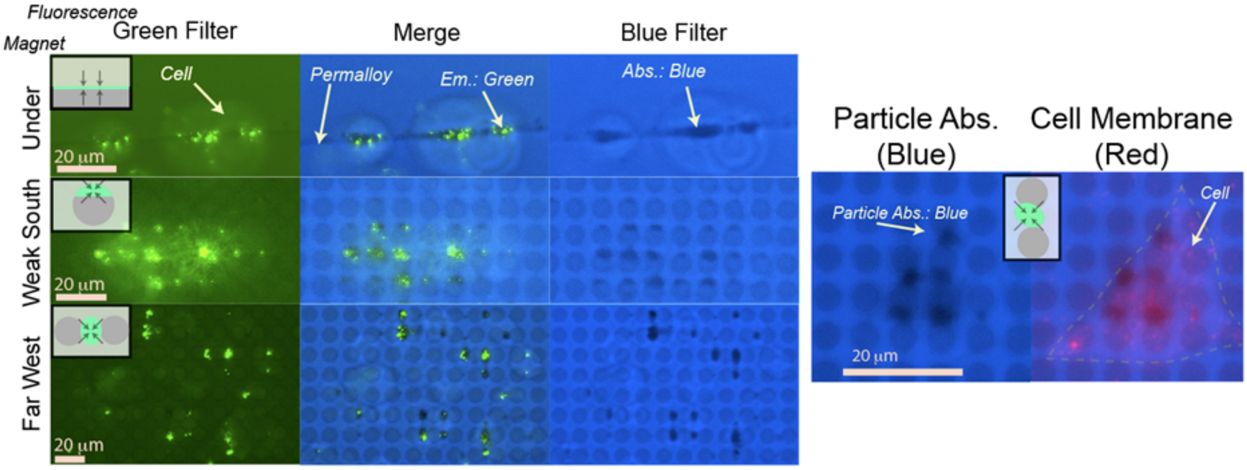

Figure 5.4: Depending on the orientation of the magnet with the substrate, the magnetic nanoparticles coalesce to distinct orientations above the micromagnetic dots. Shown at right is a merged image of cells stained with lipid stain dIl and magnetic nanoparticles.

The localization of nanoparticles for various magnetic orientations, for various shapes of patterns, follow directly with what we expect from simulation. Above magnetic lines, the particles form lines above the edges of the magnet, where fringing fields emanate from. When the magnet is oriented weakly south of the substrate, the magnetic particles "cap" the micromagnet dots, and when the magnet is oriented far to the west, meaning the incident field is nearly all tangential, the nanoparticles occupy points in between ferromagnetic dots.

The cells by default autofluoresce in the green channel, and this is seen in our images. To clarify the cell position, we also stained the cell with lipid stain dIl (red channel stain), which clearly delineates the cell membrane edge. The modification of nanoparticle position due to cell edges can be shown in the right image of Figure 5.4.

While we are able to acheive most of the desired modes of operation, localizing the magnetic nanoparticles to a position in the exact center of the magnet is difficult due to the how thin the magnetic elements are. The exact center of the magnet, in addition to in between the elements at the diagonals are dead zones for our substrate, and comprise less than 15 percent of the substrate area.

5.1.2.2 Statistical Analysis of Patterned Particles

In order to determine the precision of the magnetic nanoparticle patterning, we conducted statistical analysis for the variation of magnetic nanoparticle positioning over a set single frame area (where the magnetic field is approximately uniform in both intensity and orientation). This determines to what accuracy we can expect to be able to repeatably localize generated clusters of nanoparticles.

The centroid of particle clusters was determined in MATLAB, and the scatter is plotted as in Figure 5.5. As is shown in the graphs, we are consistently able to pattern magnetic particles with sub-micron accuracy. Presumably, using a larger magnet would improve this metric.

In our chips we also varied several parameters, specifically ferromagnetic dot size and pitch. We analyzed the effect that these subtle changes in substrate organization could affect the coalesced particles. We found that in general, particles occupied relatively consistent surface area of the substrate, meaning the area percentage of the substrate occupied by particles is relatively consistent across our varying samples. This makes sense, as the focusing affect of the particles increases with smaller ferromagnetic tip diameter. This quantity is shown in Figure 5.6.

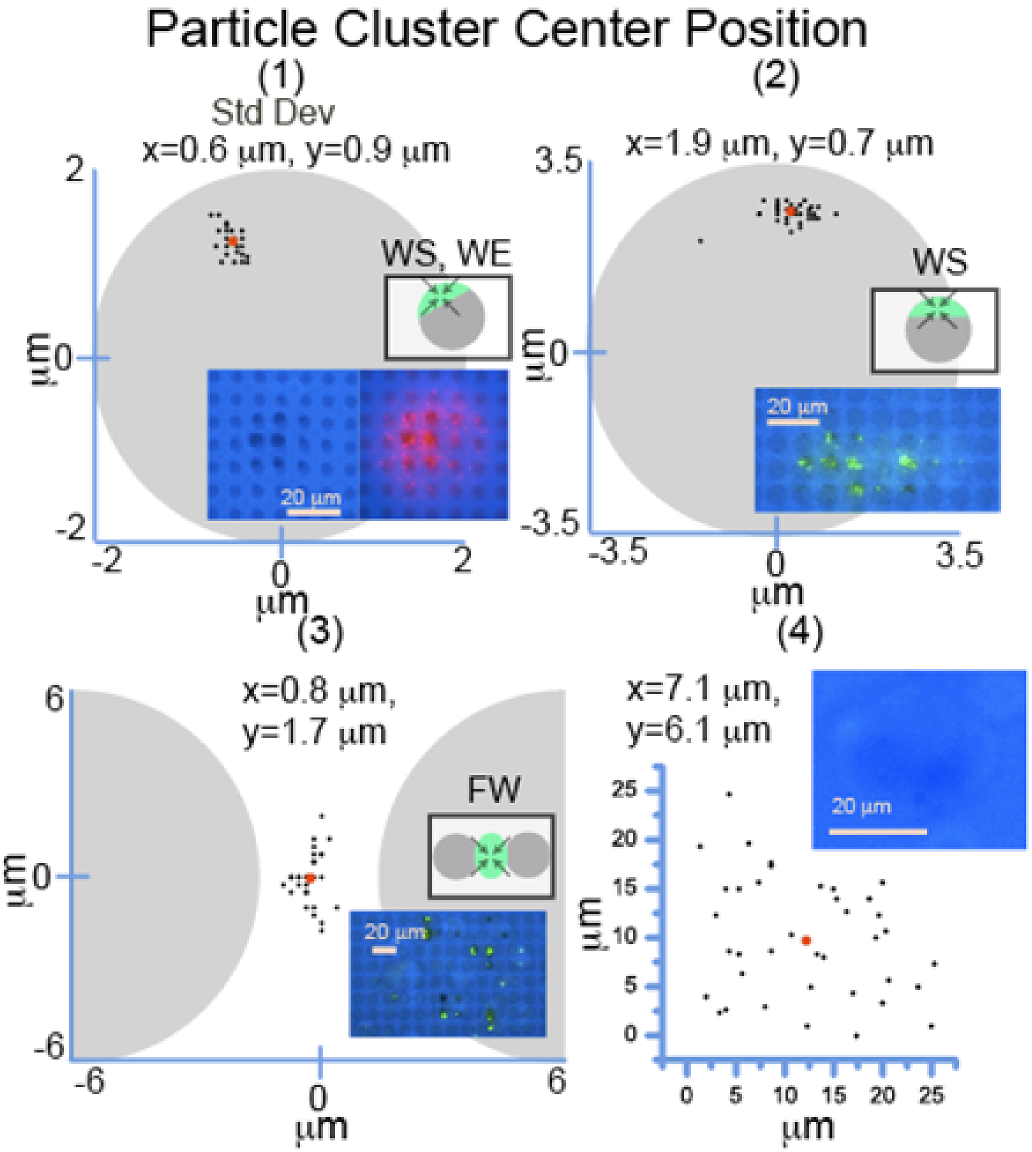

Figure 5.5: Scatter plots are overlayed on images of our ferromagnetic dots to show the variation of the orientation of the magnetic particles. Inset is an image of one of the cells from which data points are gathered.

5.1.2.3 Morphology of Patterned Particles

To complete our studies, we attempted to analyze the actual appearance of our nanoparticle cluster. This is accomplished with a focused-ion-beam, scanning electron microscope. Cells are fixed with glutaraldehyde, and dried in a supercritical dryer by sublimation of methanol.

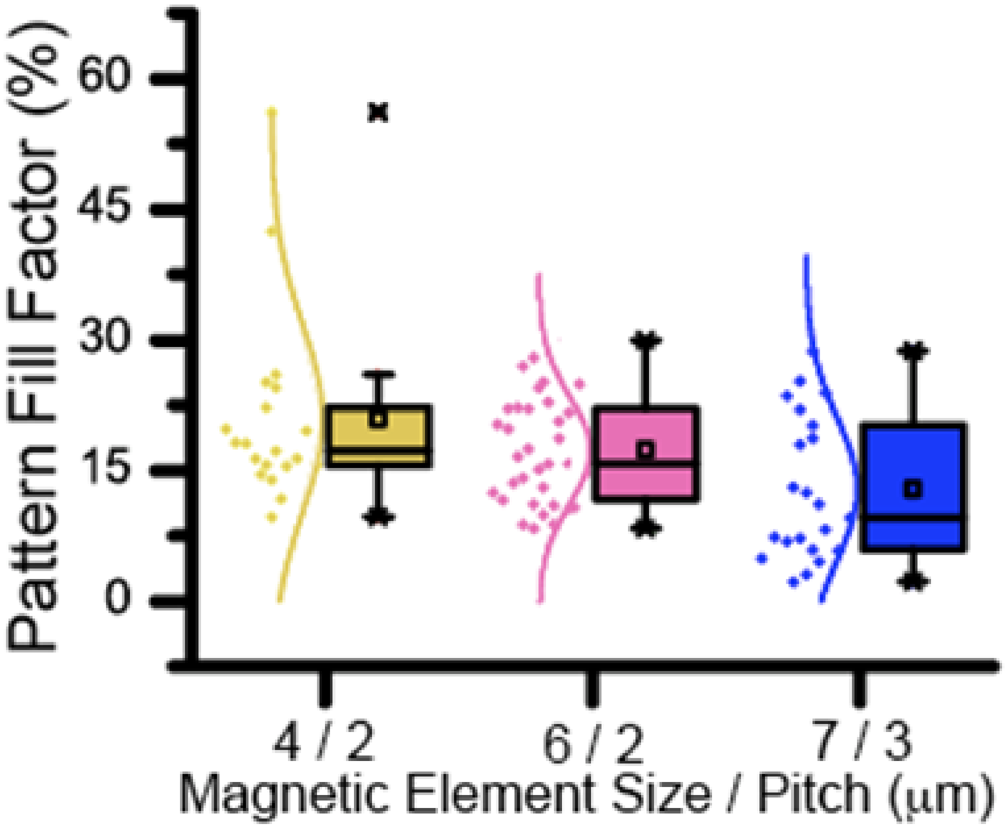

Figure 5.6: The size of the particle clusters remains relatively constant throughout the varying of the diameter/pitch size of the ferromagnetic dot pattern.

A FIB makes progressive cuts through our cell sample, slowly revealing the shape and nature of the coalesced nanoparticles in the cell (Figure 5.7). The nanoparticles are densely packed due to the long exposure time of the particles to the magnetic field and generate a noticeable bump in the cell.

Finally, we conclude with an image showing the disparate aspects of our system in high resolution (Figure 5.8). The integration of the disparate

5.1.2.4 Dynamic Patterning of Magnetic Particles

As suggested by our ability to generate highly precise localization of particles in single cells, particles should be able to be dynamically manipulated by shifting the position of the

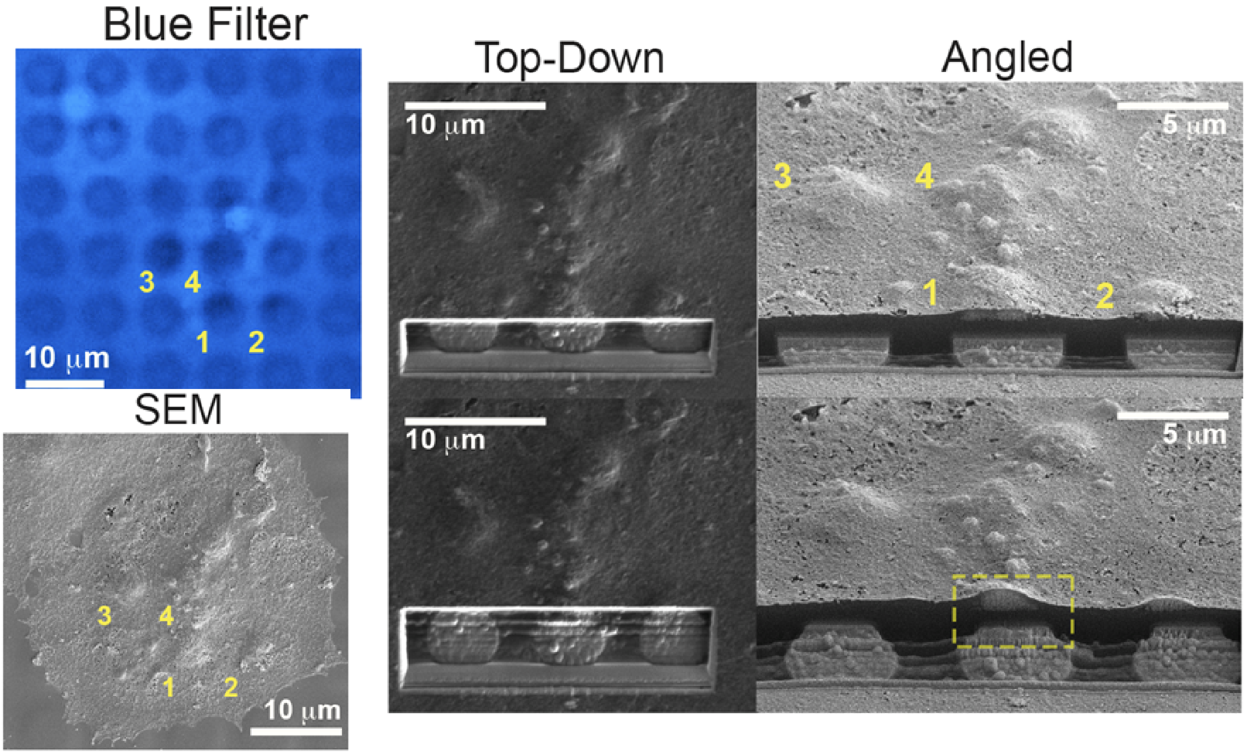

Figure 5.7: a) Top-down images of the same fixed cell under UV exposure - blue emission and SEM imaging. Four clear ensembles are noted on each image. b) Top-down and coinciding cross-sectional view of generated magnetic nanoparticle ensemble at two lines of cuts. The ensemble tends to resemble a hemisphere, as would be suggested from the magnetic potential landscape generated by the underlying ferromagnetic elements. At the bottom is a close-up of a single created ensemble.

permanent magnet behind the substrate.

We first demonstrate this capability with simple shift in pattern (Figure 5.9). Shown in a) are four groups that are strongly visible: a group flanking the left edge of the membrane, a group flanking the right edge of the membrane, and two internal, completed groups. in part b) consecutive images of the particles were taken at 10 second intervals upon shifting the permanent magnet. The left group sees little morphological changes during the time scales of the experiment, presumably due to the density and flattening against the cell edge. We found that if these particular nanoparticles were allowed to incubate with particles for

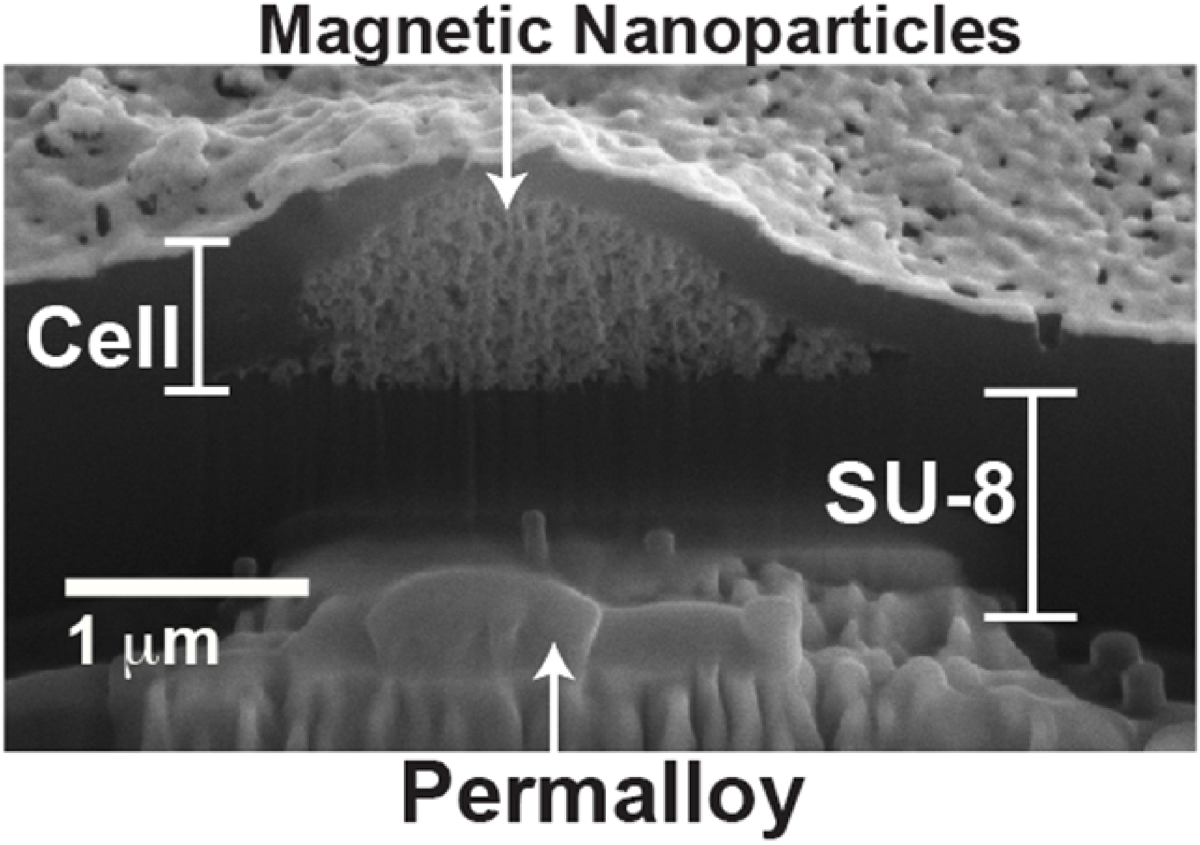

Figure 5.8: Detailed in this image are all the important aspects of our system, the planarized SU-8, the cell, the nanoparticles, and the ferromagnetic dots.

an overly long time (3-4 days), a certain percentage of nanoparticles would often simply coalesce to a section of the sample and no longer be manipulable.

The rightmost group, from images 1 to 2, and 4 to 5, sees limited movement as restricted by the cell edge, and its centroid is incapable of reaching its expected potential minima in a manner as suggested by our statistics. The differences between images 1 to 2, and 4 to 5 are shown between those particular images, and clearly illustrate the shift in position of the nanoparticles during these manipulations (for the rightmost group, in 4 to 5 it appears to have no shift). In addition, during these manipulations, various merge and separations were accomplished, demonstrating additional versatility in the technique. This is conceivably powerful to generate various quenching, reaction, combinatory reactions in dealing with the

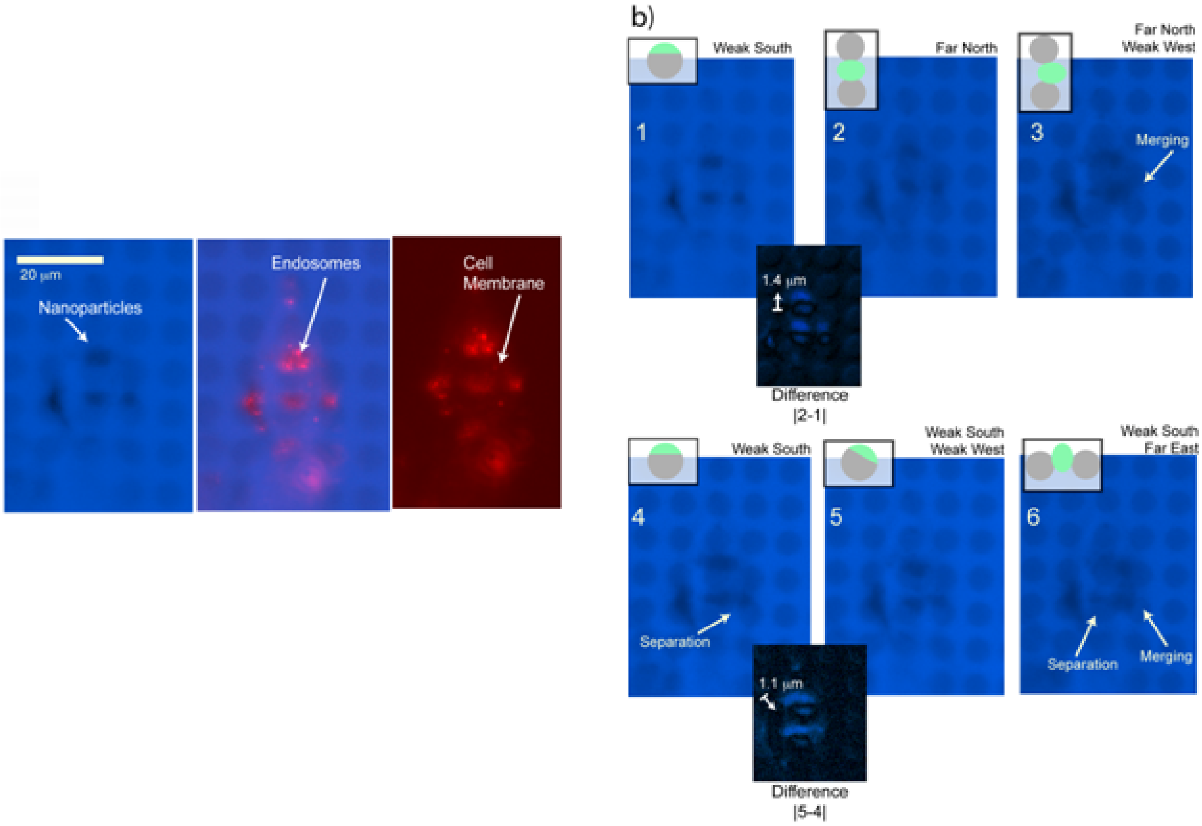

Figure 5.9: a) UV excitation blue filter, green excitation red filter and merged images of a single cell with patterned nanoparticles to be manipulated. b) Consecutive images of the particles taken at 10 second intervals upon shifting the permanent magnet. Shown are various merge and separations.

nanoparticles.

The capability of merging and separating samples gives additional capability to the technique, as one can imagine dynamically controlling the reactions of various biomolecules in a localized intracellular space, activated by these operational techniques.

Additionally we note from the red-colored stain that the red (endosomes) translates with the particles. This indicates that the nanoparticles internalize via some uptake pathway (endocytotic, phagocytotic, etc), and are quenched by the cell via endosomes, and remain in endosomes throughout the period of manipulation.

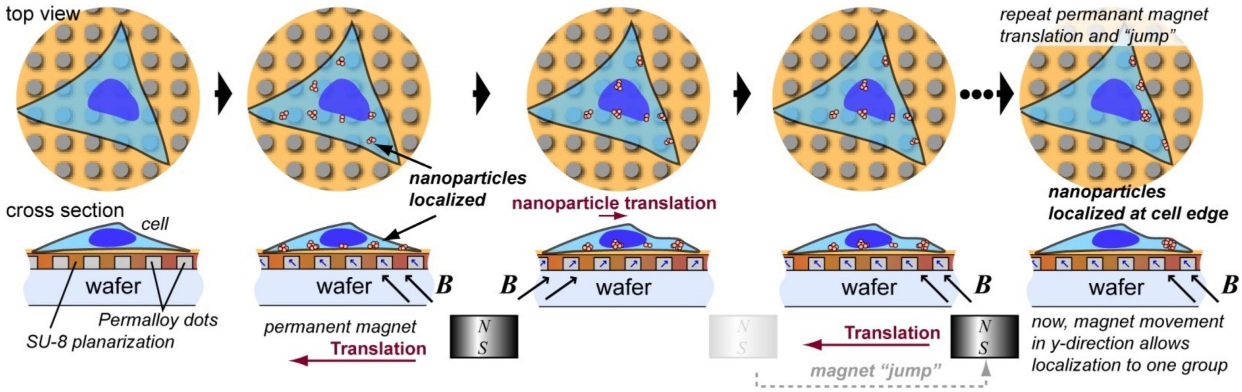

Figure 5.10: A schematic drawing shows the method of long-distance dynamic manipulation and collection of nanparticles to a subset of potential minima using a series of permanent magnet translations, movements away from the substrate (jump), and repositioning.

We next examine the capability of our system of directly translating particles to any location in the cellular environment. The technique is shown in Figure 5.10, and is accomplished by shifts and jumps of the flanking permanent magnet. The structure of the underlying ferromagnetic dot array is critical for this approach. The pitch (inter-dot spacing) must be tuned to below a critical distance so that the particles can be caught in the neighboring overlapping potential minimum after jumping. Here the diagram depicts movement of the nanoparticles to a single edge of a cell, but movement of the permanent magnet in the perpendicular direction would allow coalescence to a single ensemble, and dynamic movement of this entire ensemble throughout the cell.

In addition, it becomes clear why we designed the pitch size to be smaller than the magnetic element size; because the space in between elements is small, nanoparticles can easily be shifted to neighboring elements with high efficiency. For smaller micromagnetic dots, the particles would merely remanipulate to the opposite side of the micromagnet.

The execution of this magnetic nanoparticle translation is shown in Figure 5.11. The cells are stained with dIL lipid membrane stain. One also notes the mechanical deformation in the cell membrane generated by these nanoparticles. The induced force is enough to shift the cell

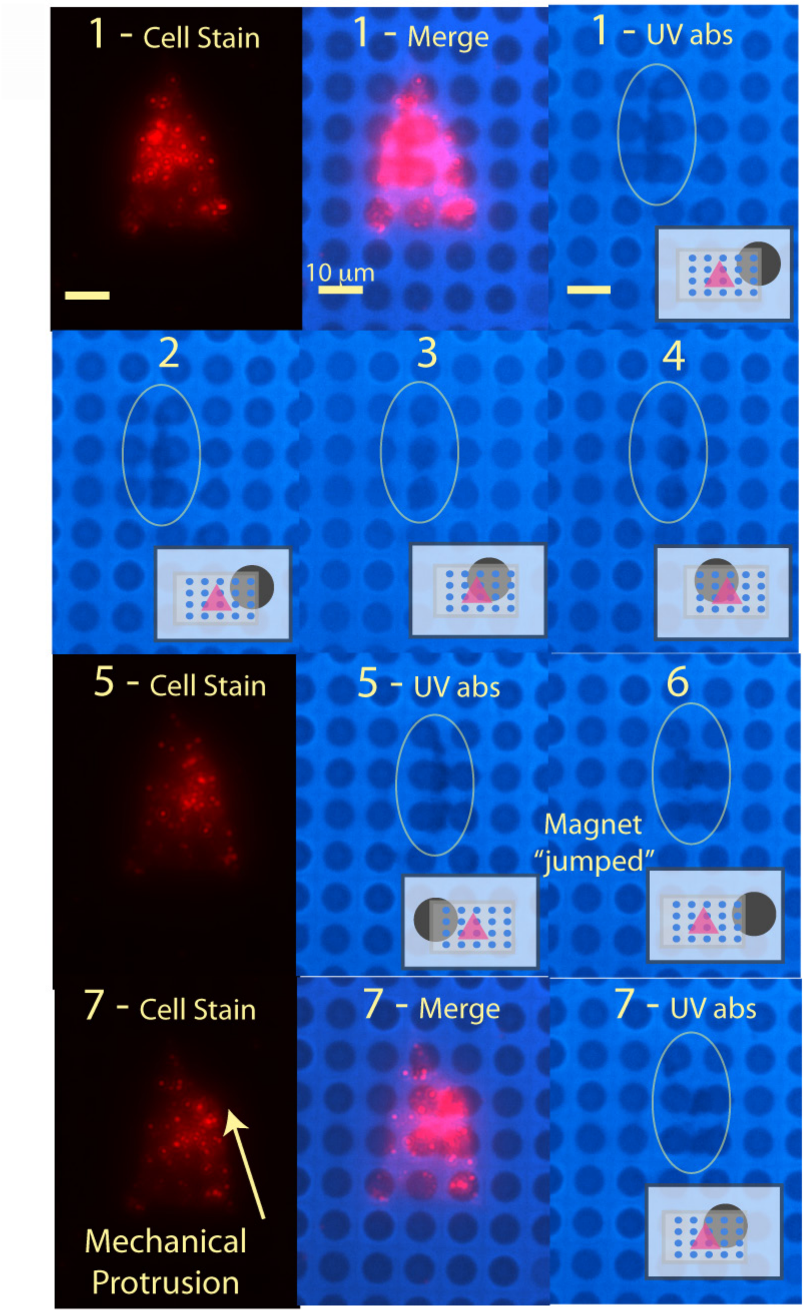

Figure 5.11: Here we show large distance shifting of magnetic nanoparticles spanning a distance greater than 10 μm. Also note a protrusion in the cell membrane caused by compression of the nanoparticle ensembles towards the right of the cell after shifting in 7, demonstrating the ability to apply large mechanical stimuli internal to the cell.

by several micron, and additionally has effects on cell shape. This conclusively demonstrates the ratcheting ability of our substrates, and demonstrates the ability to on-demand generate an effect on cellular response, in this case cell-shape and cell-morphology.

We complete this study by demonstrating the ability, with controlled rotation of the flanking permanent magnet, to precisely control these particles continuously over time (Figure 5.12). This demonstrates the precision engineers have in controlling nanoparticles in relation to the micromagnetic elements.

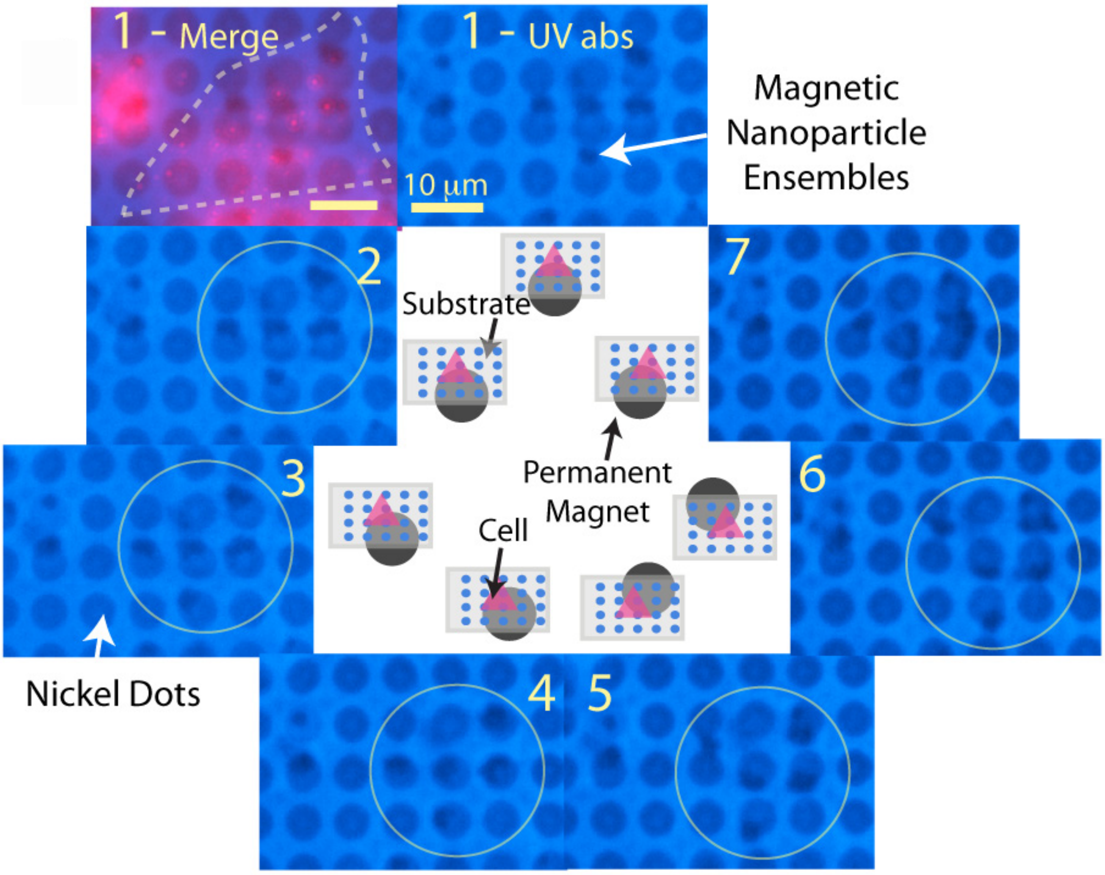

Figure 5.12: Generated magnetic nanoparticle ensembles are rotated around within the cell by a rotating magnet beneath the substrate. Movements of nanoparticles spanning a 7 μm diameter are observed.

5.2 Mechanical Stimulation of Single Cells

Here we display some metrics of our system, and introduce the large-scale induced asymmetry in cellular behavior due to our nanoparticle-generated force.

5.2.1 Time-Response

Before thoroughly examining our biological results, we display the speed at which magnetic nanoparticles nanoparticles coalesce. This gives a an idea of when the force experienced by the cell saturates to its final value. This is key for determining a baseline point from which we can time our experiments.

The response of the sample approaches saturation at less than 30 minutes. This response is approximately similar for thicknesses of resin up to 5 μm, as the saturation of the magnetic nanoparticle force is limited by particles localized across the cell that experience similar gradients no matter the thickness of the polymer resin. As resin thickness increase, however, the rate of particle localization slows beyond this expected value.

5.2.2 Force-activated Actin Response

Actin is a unique protein which can form dimers and filaments, and eventually organizes into macrostructure. In cells, it forms stress fibers, filopodia, and microvilli (which are bundles). Polymerized actin is elastically strong, and thus used to transmit forces (barbed ends on the plasma membrane). Many critical cellular structures are composed of actin, particularly those involved in cell motility, like lamellipodia (networks of actin fibers), and filopodia (which act as protrusing sensors for cells).

We find that generating forces approaching yield tension of the cell yields consistent development of filopodia around regions of high tension. A 2-d array showing some cellular response as magnetic nanoparticles increase along with increasing magnetic force is shown in Figure 5.15.

As can be seen from the image matrix, the top right diagonal of the matrix begins to

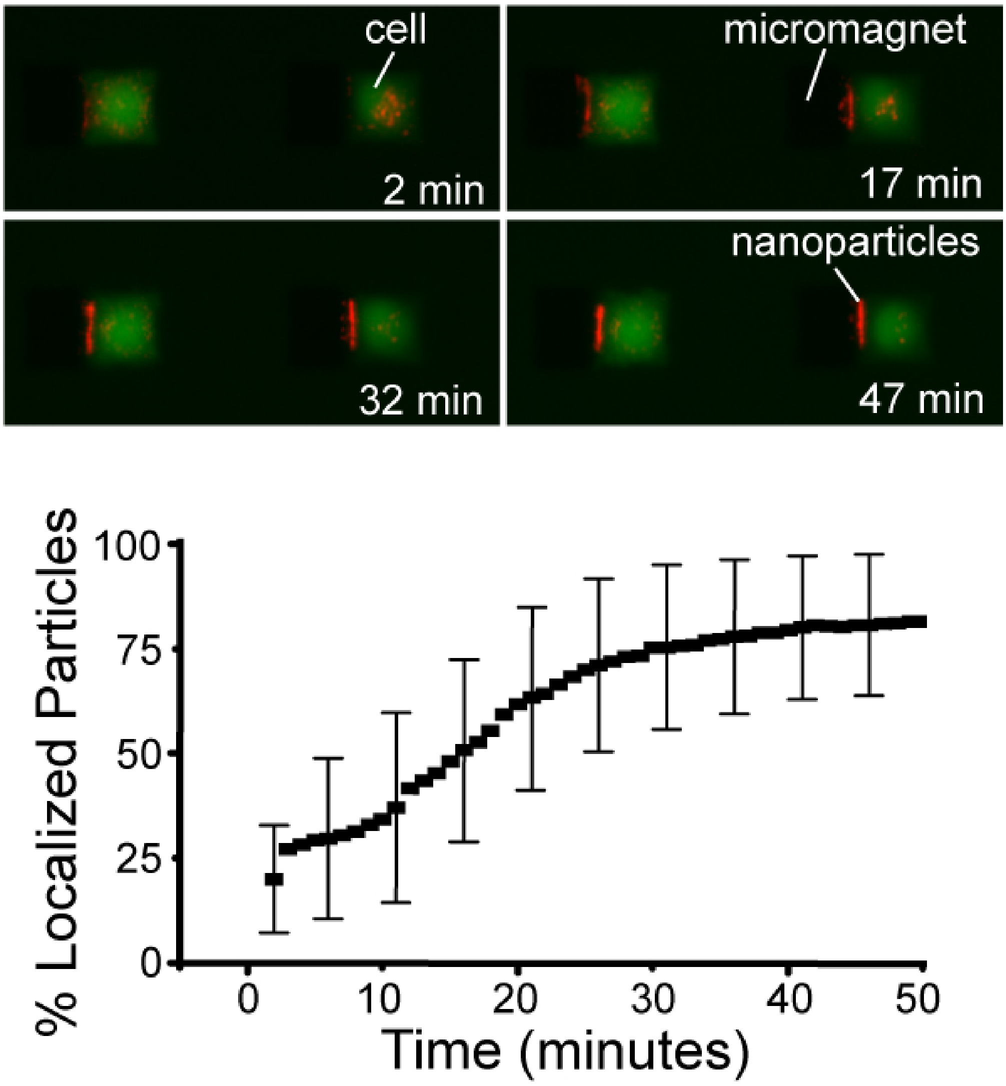

Figure 5.13: Coalescing nanoparticles under large gradients (sample thickness: .5 μm) occurs over a short timescale. The graph displays the time required for localization of nanoparticles internalized in cells on X patterns: a saturated response occurs within 30 minutes.

experience increasing quantity of induced filopodia at increasing forces. The filopodia also appear highly directed, in comparison to those originating from the corners of the samples, the filopodia radiate radially and for significant distances. In addition, the increasing force generates increasing cellular deformation, until the cell membrane yields as nanoparticles experience pull-in instability. At these yielding forces, we found that cellular response typi-

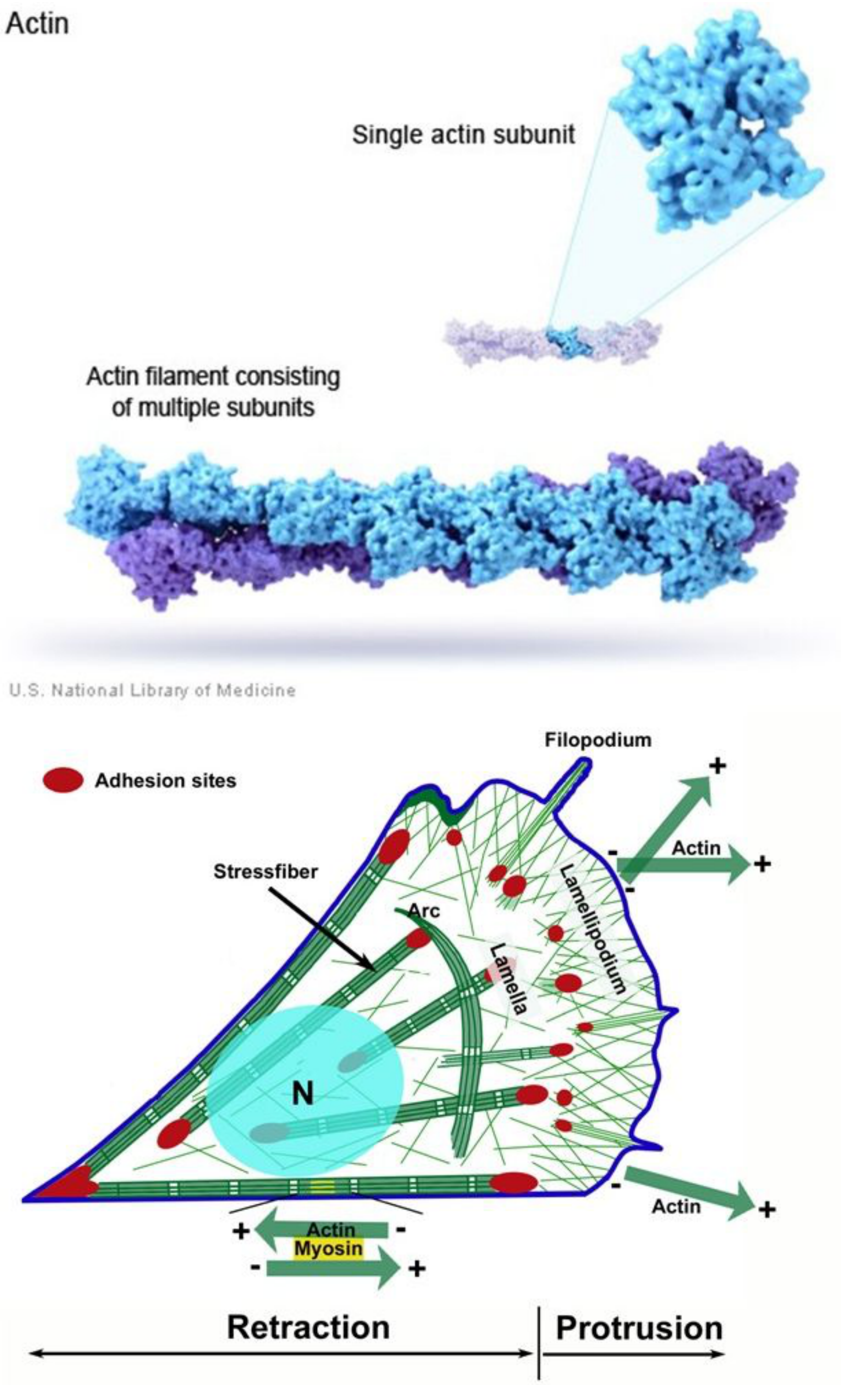

U.S. National Library of Medicine

Figure 5.14: Top: Polymerized actin composes various actin filaments. Bottom: Polymerized actin is able to generate and carry tensions during cellular activity.

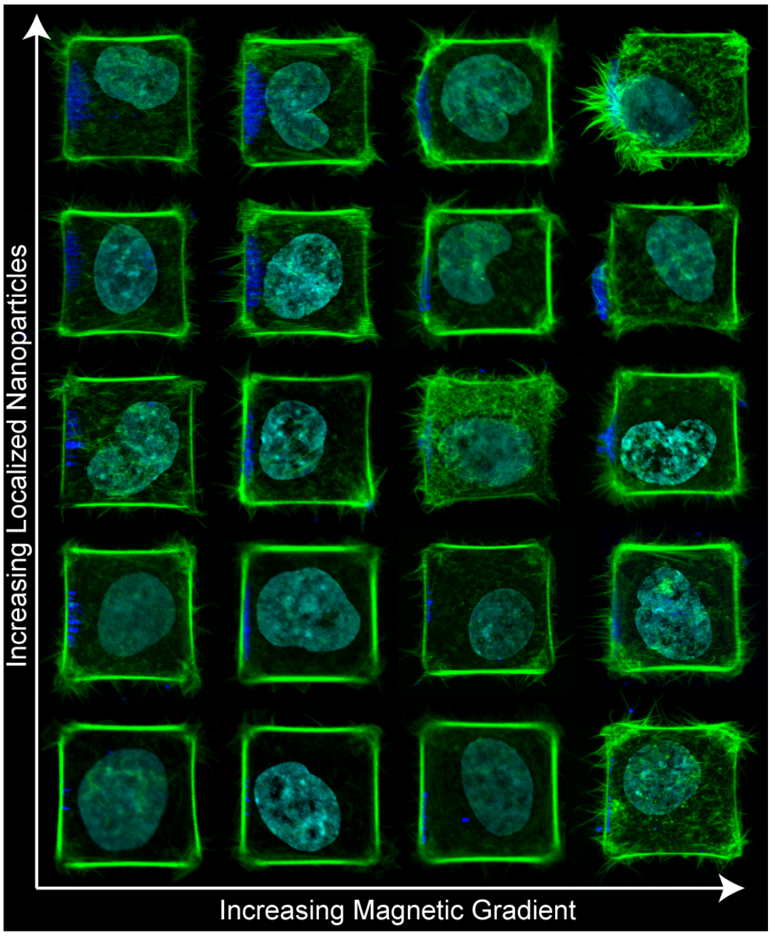

Figure 5.15: The array of images shows representative results as nanoparticle dosing and magnetic field gradient increase. As force increases, an increasing number of cells begin to display actin-spiking and protrusions, and clear deformations in the cell membrane are generated, until finally some cells (upper right corner) experience a pull-in instability where particles are pulled through the original membrane boundarys. The gradient range varies from 2500 to 70000 T/m, while the nanoparticle dosing varies from approximately 5 pg to 300 pg / cell.

cally diverges, as there are at times extreme responses in filopodia, but mostly an actin stress fiber reforms to reject the forced nanoparticles. It is very likely that this is a time-dependent response, and that after the initial cell membrane destabilizes, the cell will eventually reform its boundary.l

5.2.2.1 Immunostains of Filopodia

Actin bundles protruding from the cell cortex are invariably defined as filopodia, but we attempt to analyze these structures further, to see whether they possess the activity of typical filopodia. Normal filopodia possess specific proteins at the tip structures [67], the critical component being Myosin-X, which recruits a number of important proteins to filopodia tip in order to give them their activity (primarily integrins, which bind to extracellular matrix to form focal adhesion). This is what give filopodia their sensor-like ability, as proteins at the tip complex preferentially interact with the environment depending on whether chemical activity is induced.

We stained our force activated filopodia for a number of critical filopodia defining components. Fascin, which is a protein that bundles actin together, should co-localize with filopodia spikes. Myosin-X, the protein mentioned in the previous paragraph that gather components to the tip, should localized at the filopodia tip. β-integrin, a type of cellular integrin that binds ECM, should localize strong to the filopodia tip. Finally, phosphorylated tyrosine, or acivated critical tyrosine kinases (which control a variety of cellular processes), should localize to filopodia tips.

The results of these stains are shown in Figure 5.16. As shown in the figure, the tips are positive for the tip proteins notated in the previous paragraph. This suggests the filopodia generated by our mechanical tension are capable of interacting, and sensing the environment of the cell.

5.2.2.2 Actin Protrusion Asymmetry

We attempted to characterize the actin protrusions by generating a metric to determine the local quantity of actin as it compares to the rest of the cell. This was explicitly defined in chapter 4, and describes the average actin protruding local to the force as compared to actin protruding over other similar lines in the cell.

Show in Figure 5.17 are our shapes cells displaying high asymmetry in actin protrusions. In addition to a significantly increased quantity of filopodia emanating from the origin of the

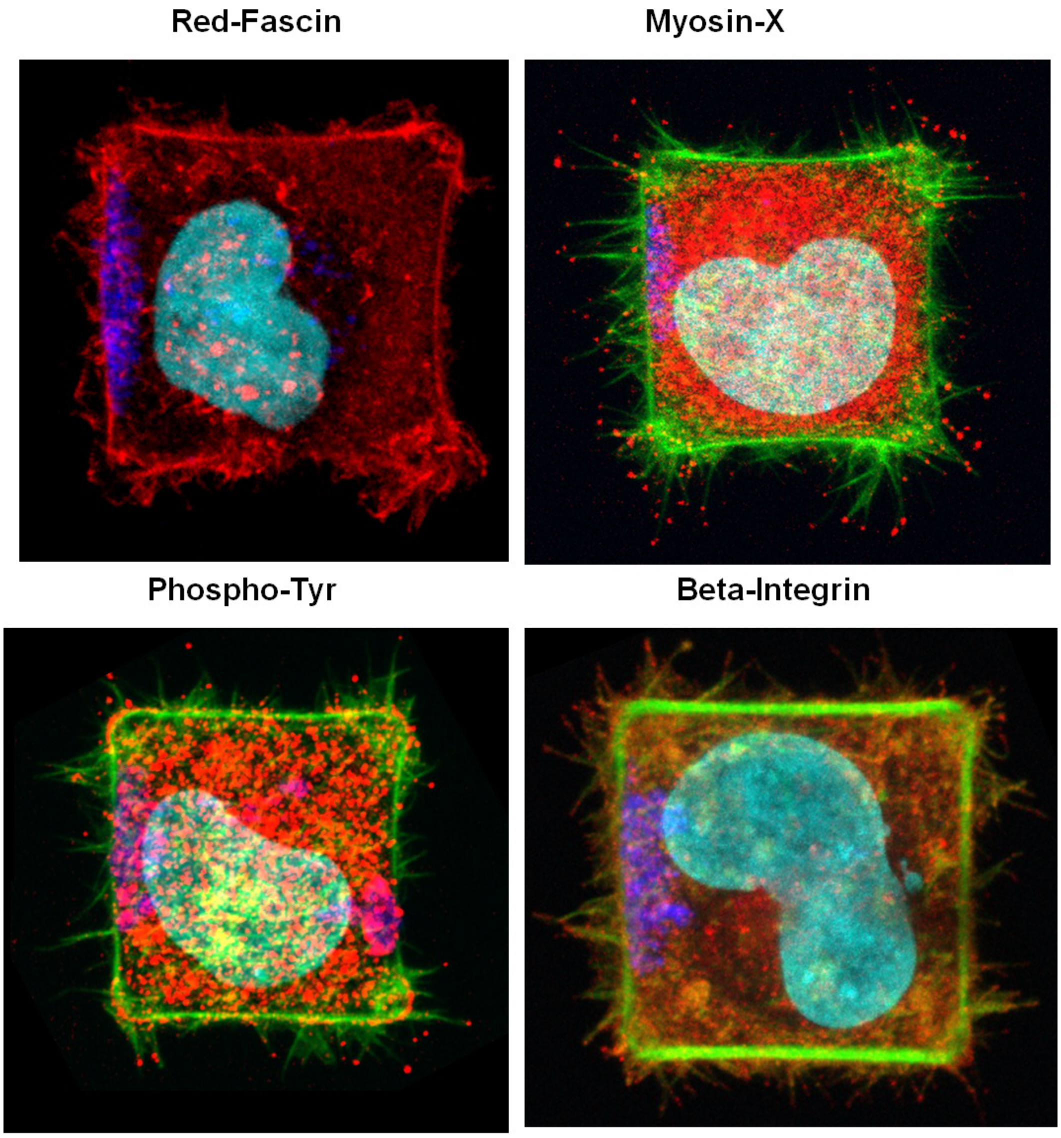

Figure 5.16: We demonstrate that the cells stain positive for a number of critical filopodia components, including fascin, p-tyr, myosin-x, and beta-integrin.

force, these filopodia often appear highly directed when compared to other existing filopodia. This organization suggests a coordinated response by the cell in response to the generated tension.

Actin asymmetry data (Figure 5.18 was determined from three different samples stimulated at the same time, and of three different thicknesses, 0.7 μm, 2.1 μm, and 4.3 μm. Our

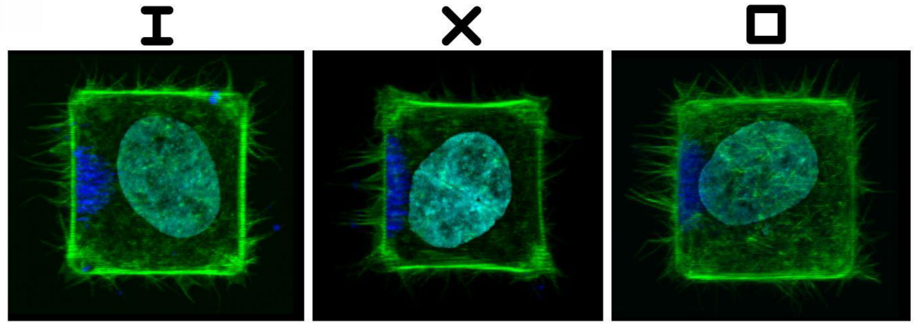

Figure 5.17: Square shaped cells, forced into this shape by different fibronectin patterns (I, X and square outline shapes), displaying high asymmetry in protruding actin, typically characterized by highly-directed actin spikes emanating from the origin of force.

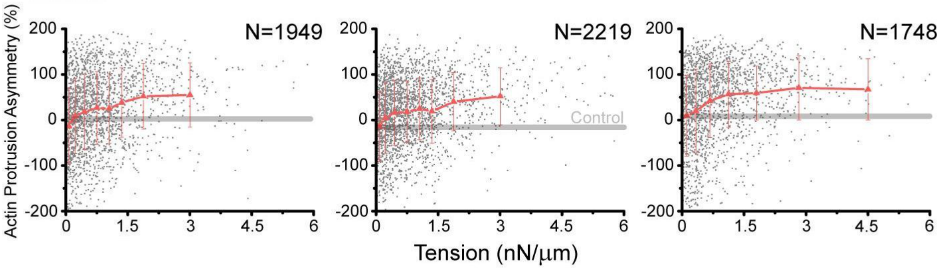

Figure 5.18: Scatter plots with overlayed averages plotting the actin protrusion asymmetry (zero corresponds with symmetric actin across the cell). As force increases, the scatter of individual cell response trends from random around zero bias to positive, indicating an increasing number of cells experience localized actin polymerization from where force is applied to the membrane.

scatter plots show distinct trends in actin asymmetry, as an increasingly large percentage of cells see positive biasing in local actin. The baseline of the sample is determined from results from our control plots (Figure 5.19): these are samples overloaded with magnetic nanoparticles, to quantities on average four to five times higher than those as gathered from our data in Figure 5.16.

This data is reemphasized directly in scatter plots from the three samples that comprised

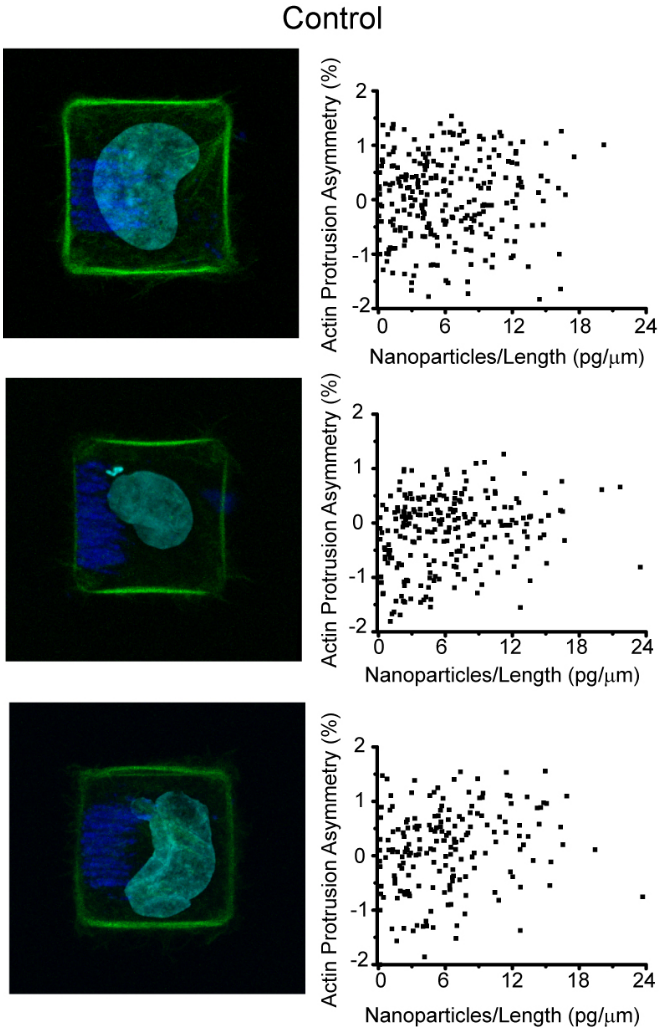

Figure 5.19: Representative images and corresponding scatter plots for actin asymmetry control cells overloaded with coalesced nanoparticles without applied force. Shown in the plot are equivalent percent difference scatter plots displaying percent difference of localized asymmetric actin as it varies with increasing particles/μm localized to the cell edge (around 4-5 times higher than the average cell of Figure ??).

this data. As can be seen from these two controls, cells overloaded with particles (which do not induce significant asymmetry in filopodial protrusioin), and in addition, different quantities of nanoparticles generating tension (as shown in our substrates of different thickensses), do not induce differences in induced filopodia. In fact, the response is highly consistent with respect to generated mechanical tension, rather than any quantity of localized nanoparticles, or endosomes.

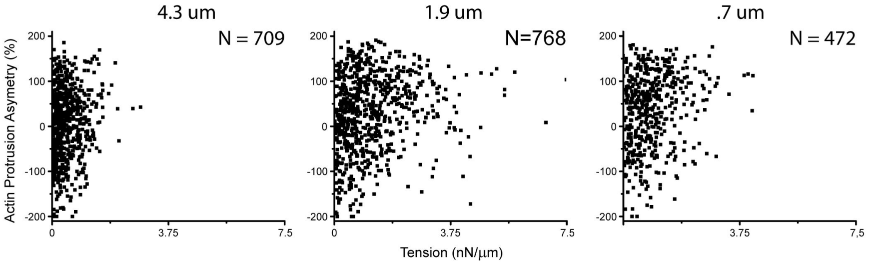

Figure 5.20: Scatter plots of actin protrusion asymmetry for cells patterned in I shapes at the 3 distinct resin thicknesses (0.8, 2.1, and 4.3 μm). Each resin thickness yields different magnetic gradient magnitudes and thus different forces for the same number of nanoparticles. The data is consistent despite the varying quantities of nanoparticles generating the identical respective tensions for each of the samples.

We additionally attempted to determine metrics as to tensions and stresses at which cells will respond in a certain manner. We extract from our plots certain parameters of cellular response, for example the yield tension and stress (the tension at which the cell membrane destabilizes and the nanoparticle experience pull-in instability.) Additionally, from our actin measurements, we determined metrics for the protrusion threshold, which we define as the tension at which a significant number of cells have a significant asymmetry filopodial protrusions. This is shown in Figure 5.21.

We found that the I and X shapes had similar yield and protrusion thresholds, while square shapes have a slightly higher yield thresholds, while significantly lower (under half magnitude) protrusion threshold. From confocal microscopy, the thickness of the nanoparticle clusters in these yielding cells typically varies between 1.5 to 2.3 μm with an average of 1.8 μm. This is used as our approximate thickness.

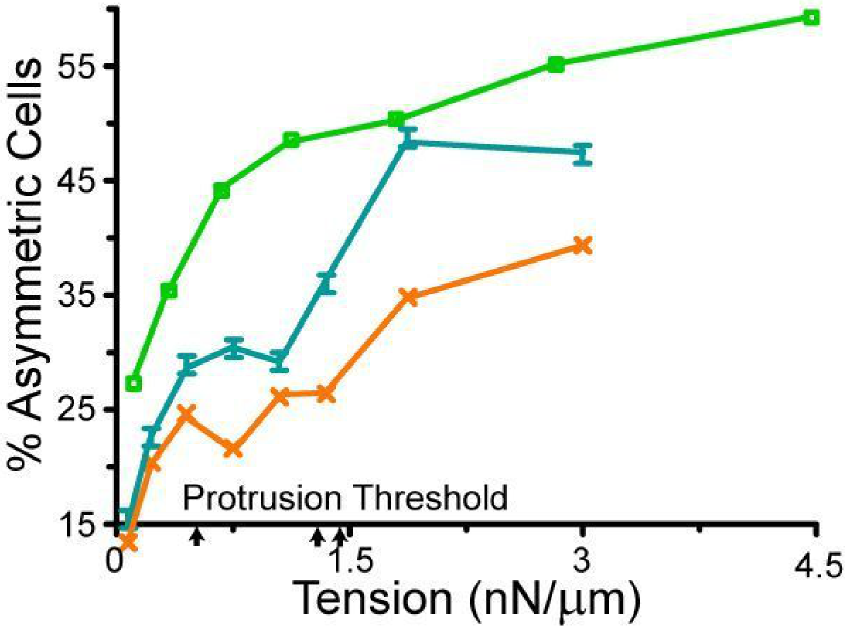

Figure 5.21: The graph displays the percentage of cells at a given force level with actin asymmetry over 70 percent. Here we define a protrusion threshold, as the tension at which this asymmetry nears its maximum observed.

5.2.2.3 Inhibitor Studies

In order to characterize the molecular origins of force-dependent filopodial generation we systematically inhibited previously characterized mechanotransduction pathways. A number of stretch-activated calcium channel blockers [68, 69, 70], including the EGTA quenching of calcium itself, did not induce any noticeable effect on filopodia.

Shown in Figure 5.23 is the normalized filopodial-generation of three separate normally run samples on three different days, with one carrying DMSO. The responses are approximately consistent throughout the samples, and the induced filopodia consistently increase with increasing tension. In addition we found that, as expected, DMSO itself has effectively no effect on filopodial generation.

	I	×	□
Experimental Yield Tension (nN/μm)	4.3	4.7	5.6
Estimated Yield Stress (nN/μm²)	2.4	2.6	3.1
Protrusion Threshold (nN/μm)	1.3	1.5	0.5

Figure 5.22: The table compares yield tension between cells on different adhesive patterns (defined as the lowest average tension at which nanoparticle clusters are observed to break through the cell membrane). Yield stress is estimated from yield tension and approximate nanoparticle thicknesses as obtained from confocal microscopy. Protrusion threshold is defined from Figure5.21.

Shown in Figure 5.24 are the normalized filopodia-generation responses to seven inhibitors of major mechanostransductive proteins: CK-869 (Arp 2/3) [71, 67, 72], wortmannin (PI3K, PAK) [73, 74], PD98059 (MEK/ERK) [75], PP2 (SRC kinase) [76], axitinib (VEGFR,PDGFR) [77], NSC23766 (RAC) [78, 79, 80], and IPA-3 (PAK) [81, 82, 83, 84, 85] in comparison to uninhibited controls run on the same day. Of the twelve inhibitors we tested, only two showed significant inhibition of the force-induced filopodia across all force ranges: wortmannin and IPA-3, while RAC inhibition was more modest but significant at higher forces. Wortmannin has been shown to have an effect on both PAK expression and localization (although the intensity of this inhibition is unquantified), while IPA-3 is commonly used as an inhibitor of the various forms of PAK [86].

Images representing typical filopodial response of cells with exposure to these inhibitors are shown in Figure 5.24. In comparison to uninhibited cells, wortmannin inhibited cells showed fewer and shorter filopodia emanating from the origin of force whereas IPA-3 treat-

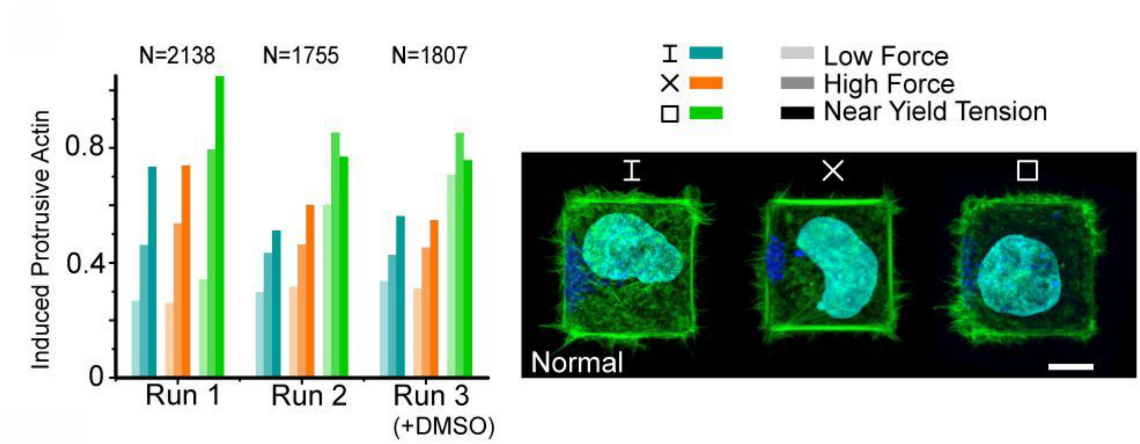

Figure 5.23: Triplicate runs quantifying the average intensity of filopodia around regions of high tension. The response is consistent across multiple runs, with or without the addition of DMSO, the carrier for a number of the inhibitors. To the right are typical cellular responses at moderately deforming tensions for these samples, showing localized protrusion of filopodia from the site of force.

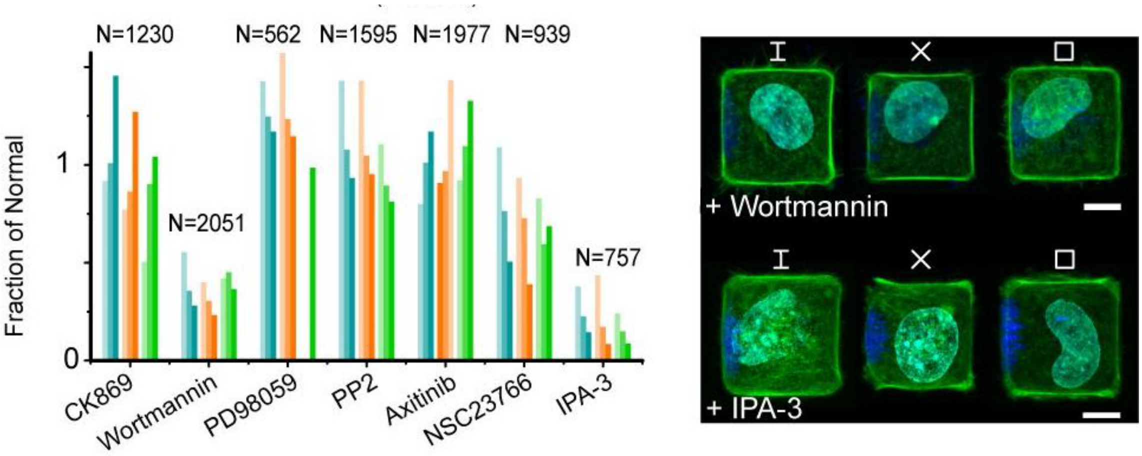

Figure 5.24: Results from inhibitor studies for 7 inhibitors of mechanotransductive proteins. The responses for the vast majority of inhibitors showed little variation from its corresponding control sample, except for wortmannin and IPA-3, both shown to affect PAK activation and localization. Representative images for each inhibitor are shown to the right.

ment eliminated a significant percentage of the filopodia altogether. In addition to suppressing filopodia, a percentage of treated cells (40 %) displayed non-apoptic blebbing (Figure 5.27) [87].

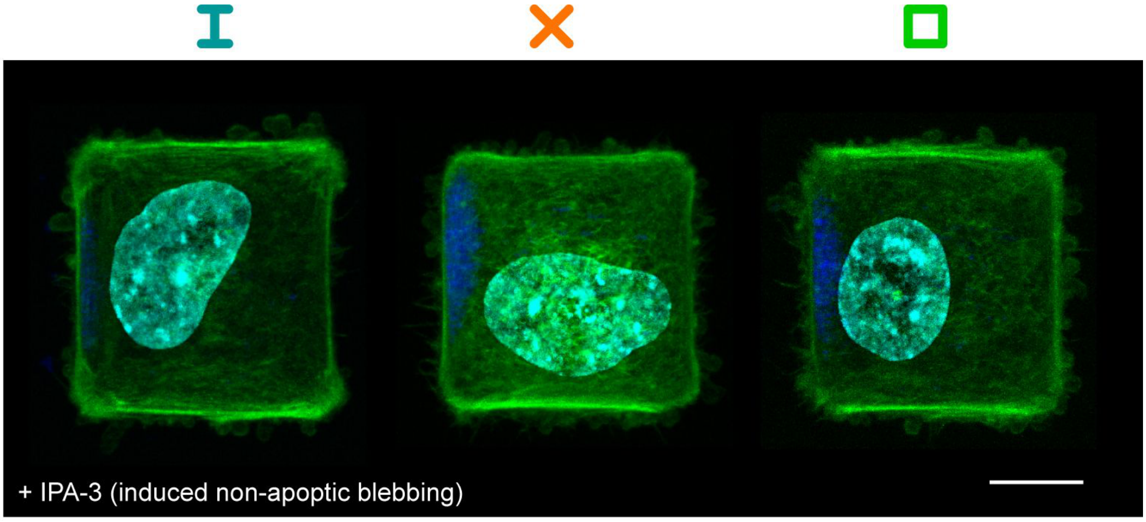

Figure 5.25: Cells blebbing under inhibition of PAK by IPA-3. The blebbing typically occurs uniformly and unbiased towards the direction of force.

Blebbing has been demonstrated to occur with both PAK inhibition [88], and in knockdown of critical filopodial interacting proteins [89, ?]. Blebbing cells were not included in our analysis, as the blebs impaired our ability to quantify the protruding filopodia. In general, however, blebbing cells displayed similarly low intensities of filopodia to those without significant blebbing.

Immunofluorescence experiments additionally revealed the significance of PAK. Shown in Figure 5.26 are consecutive z-slices for cells significantly deformed by our tension. Arrows point to bands of high membrane localization of activated PAK, which progress all along the regions of high deformation. Additionally, phospho-PAK localizes to filopodia tips in cells grown on I and X patterns, and throughout filopodia on square patterns (presumably from filopodia emanating from positions close to fibronectin adhesion) (Figure 5.27). Overall, these data suggest that the localized nanoparticle-mediated force leads to execution of a PAK-dependent biological program of filopodial generation that is similar in nature to

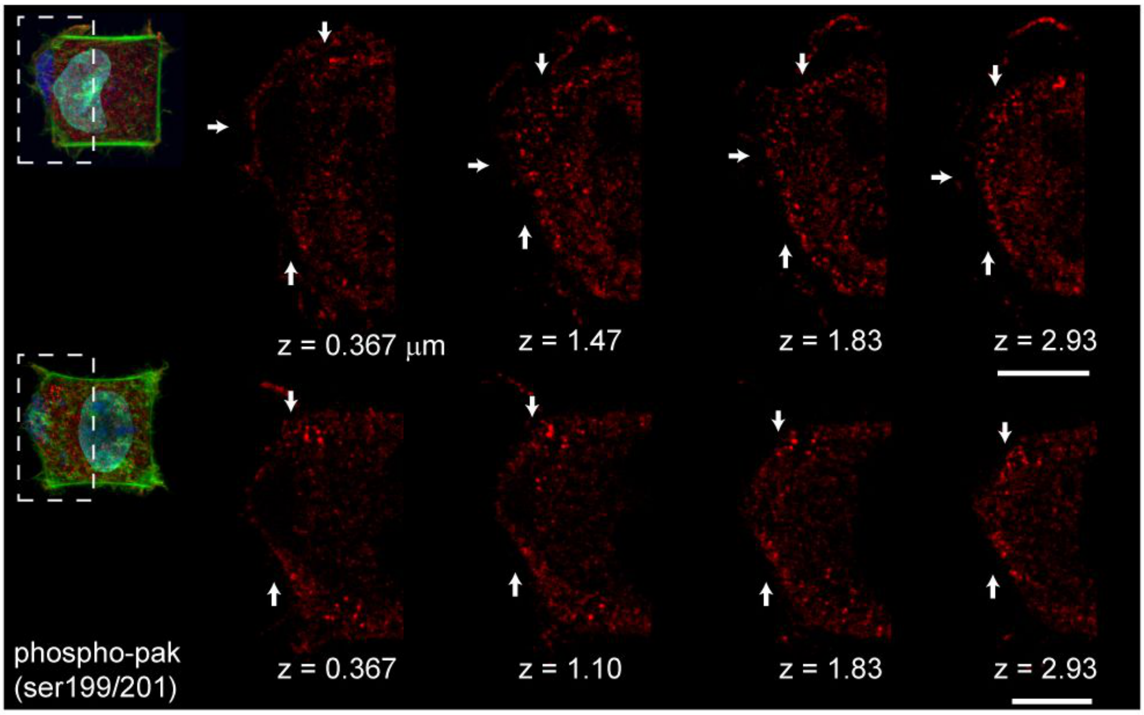

Figure 5.26: Z-slices displaying the activation of membrane localized phospho-PAK, which forms a band that enfolds regions of high deformation. This occurs whether or not cells exhibit a particularly high filopodial asymmetry.

filopodial generation at locations of cell adhesion (and force application) to the fibronectin substrate.

5.2.3 Discussion

Our results suggest mechanical tension guides the formation of active cytoskeletal elements (in particular actin-based elements such as filopodia), and it does so through biochemical pathway involving critical mechanotransductive proteins. In our case, we found that P21-activated kinase (or PAK), is critical to the development of this asymmetrical response.

PAK is implicated in a wide variety of cellular biology, including cell motility and morphology, in cytoskeletal reorganization, and in the formation of filopodia. A number of cancer cells are known to overexpress this protein, and is the cause of the increased motility of many

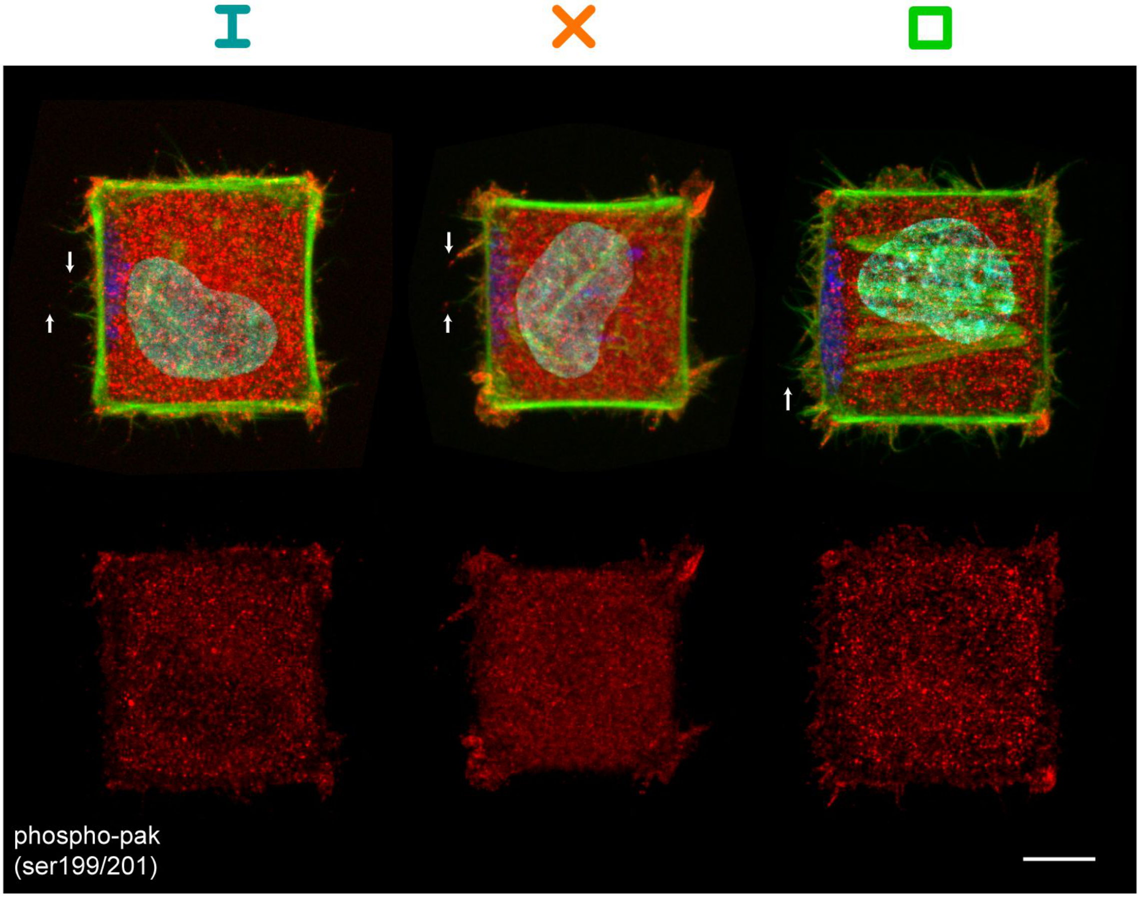

Figure 5.27: Phospho-PAK stains filopodia tips for filopodia emanating from forces in I and X samples, while it stains both the filopodia tip and body for filopodia emanating from regions close to fibronectin (square samples and edges of I and X samples).

cancer cells (as more PAK protein means more activated PAK and increased cytoskeletal fluctuations). It is a target of a number of important upstream proteins that more generally controls these responses, for example it is the effector of the well-known protein CDC42 (ie. CDC42, when activated, will activate PAKs to generate the response). We demonstrate here, that through tension, PAK will localize to cytoskeletal components (stress fibers), where it can effect change through the development of filopodia.

5.2.4 Force-activated Biasing of the Metaphase Plate

We additionally demonstrate the ability to manipulate another cellular processin this case the organization of DNA and subsequent division of cells during mitosis. The adhesive environment has been shown to direct the spindle axis, and subsequently the chromosomal organization and division axis of cells [90, 91, 92]. Recently, force was shown as the fundamental origin of this biasing with labor-intensive experiments on a few cells21. Here, we confirm these results and show that our magnetic nanoparticle-mediated forces can simulate intracellular cortical forces en masse, causing dramatic 45 to 90 degree shifts in the orientation of DNA and the subsequent division axis of single cells. Cells synchronized by double thymidine block were stimulated on our magnetic substrates in triplicate for three conditions (at the maximal magnetic fields, at an order of magnitude lower holding fields, or at 0 field), fixed during mitosis, and imaged.

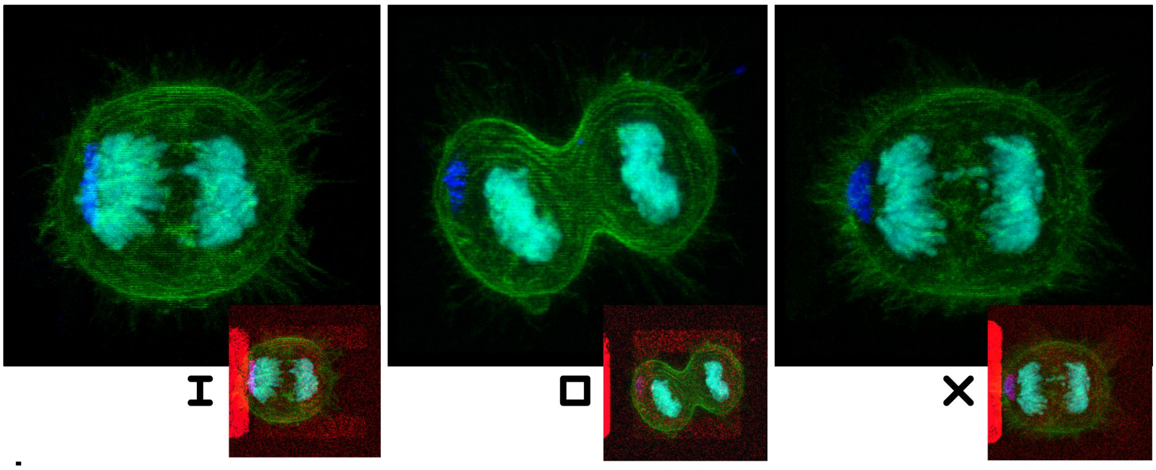

Figure 5.28: Cells dividing after adhering on I, X, and square fibronectin shapes are observed to divide along the axis of applied force.

Division axis was determined as perpendicular to the metaphase plane. Cells in which force was applied by nanoparticles exhibited cell division axes significantly biased along the direction of force in comparison to control samples in which nanoparticles were localized but then the magnetic field was reduced or removed. Stained cells with mitotic spindle biased under magnetic force are shown in Figure 5.28. Red signal indicates fibronectin, green signal shows actin, dark blue indicates nanoparticles, and cyan indicates DNA stain.

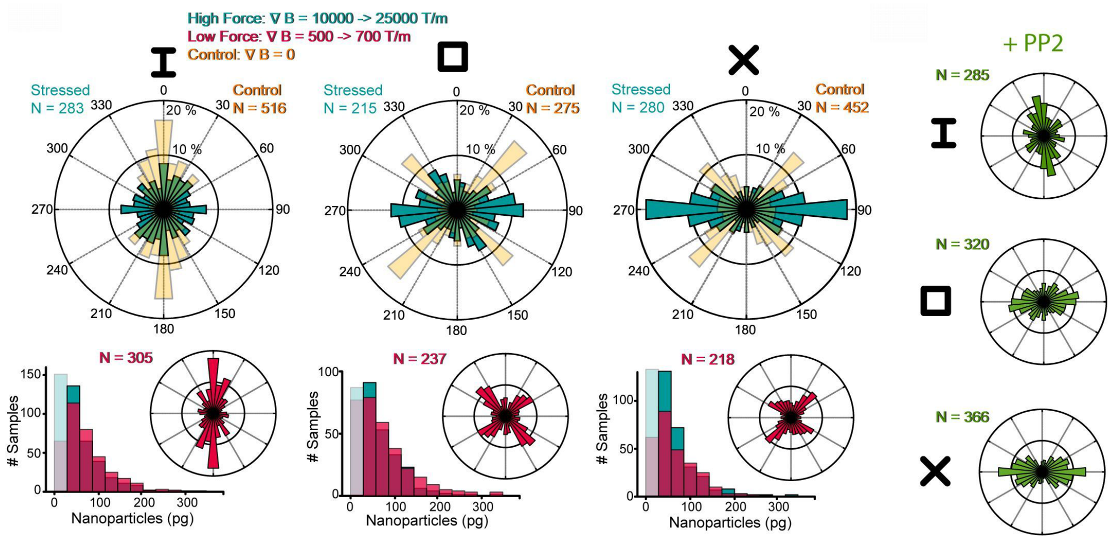

Figure 5.29: Left Top: The orientation of the metaphase plate and the subsequent cell division axis is significantly biased by nanoparticle-induced force when compared to control cells with initially localized nanoparticles but no sustained force. Left Bottom: Spindle angle histograms for control samples initially localized with nanoparticles but subsequently released to a lower holding force, in conjunction with bar plots comparing the distribution of coalesced nanoparticles for both low and high applied force conditions. Right: Results from samples under maximally forced conditions with addition of PP2.

The distribution in quantity of localized particles for both the high force and low force excited cells are shown in Figure 5.29. Despite possessing essentially the same distributions of nanoparticles, the distribution of spindle axis angles varies significantly. The angle of orientation is biased towards the direction of force in each case in a manner which competes with the extracellular cues from the underlying pattern of adhesion (I, X, and square). High force stimulation experiments in the presence of the inhibitor PP2, which has been shown to disrupt FAK, and thus force sensing of retraction fibers [90], also yields similar results. These data suggest that force-induced biasing of division axis can occur independently of focal adhesion kinase.

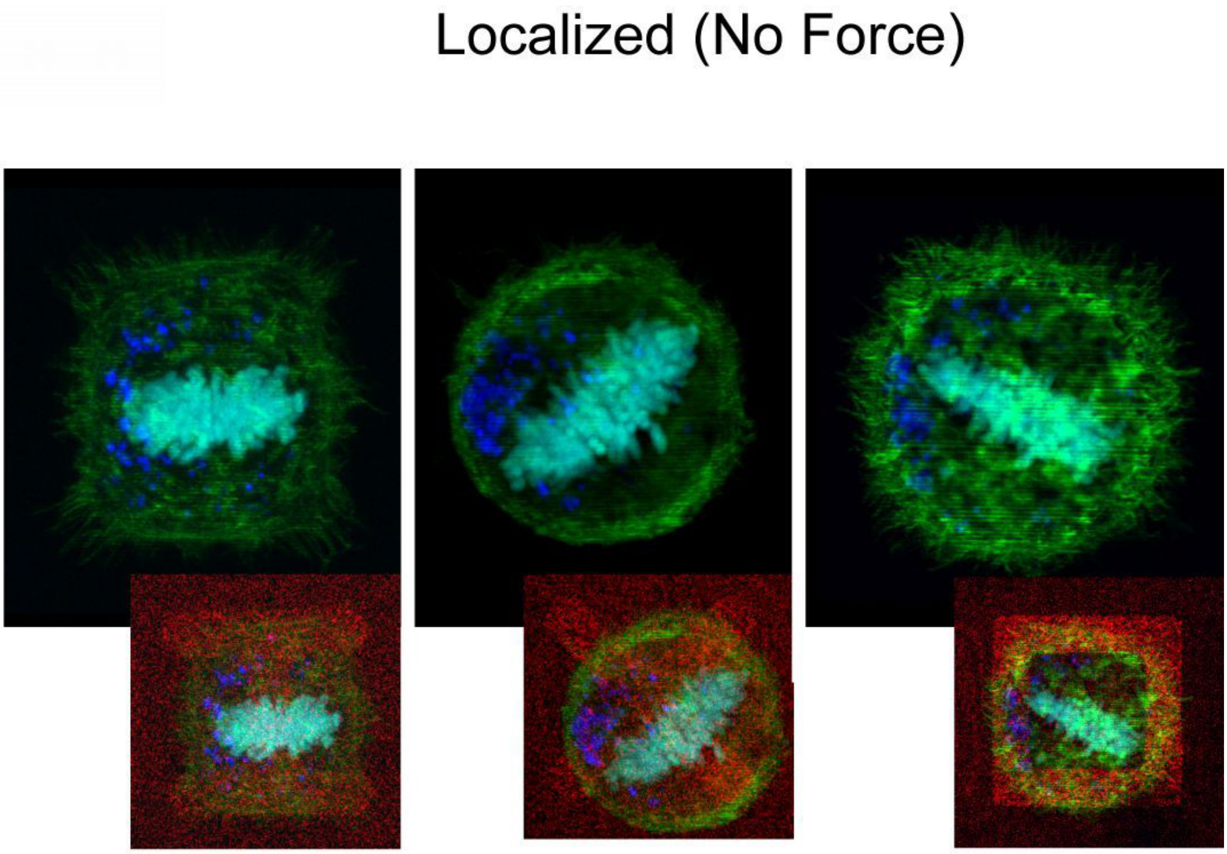

Figure 5.30: Control cells from these experimentsthe nanoparticles are localized inside the cell, but are significantly less dense due to the removal of the magnet.

Shown in Figure 5.30 and Figure 5.31 are the sample control cell images from our two different control condition: particles coalesced and released (the particles slowly diffuse back into the cytoplasm), and particles coalesced and held at a lower holding force.

5.2.5 Discussion

The biasing of cell division axis is more apparent for cells patterned on X and I shapes as opposed to the square fibronectin patterns. For both the X and I patterns force was applied to the cell membrane in regions with no adhesive connections to the substrate which differs from the square pattern in which the cell interacts with the substrate through retraction fibers in an overlapping region to where force is applied by the nanoparticles. It is likely that

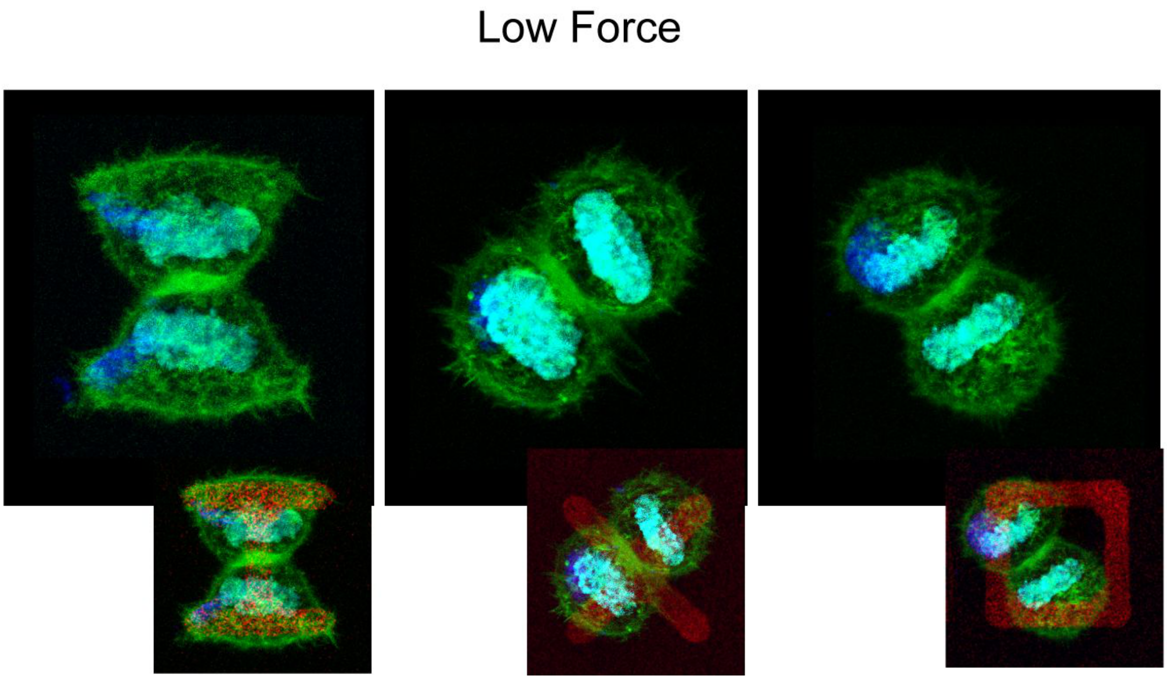

Figure 5.31: Low-Force condition cells, experiencing a reduced force do to movement of the magnet away from the sample.

the additional force generated from the nanoparticles competes with retraction fiber-induced force, and thereby reduces the overall change in local cortical tension upon application of magnetic field as compared to other patterns. The retraction fibers can be seen in Figure 5.32, and are composed from confocal images taken from the bottom planes of the confocal z-slices.

5.3 Discussion of Results

In these biological results, we demonstrate the capability of internalized particles to polarize cellular behavior in a massively parallel manner. Fundamentally, we believe this to be a powerful demonstration of the ability of simplistic manipulation in magnetic nanoparticles to induce massive response in biology. The concept, and indeed the execution can be broadened in scale to include a variety of other functionalized magnetic nanoparticles, within or outside of endosomes, to induce response on biology through localization.

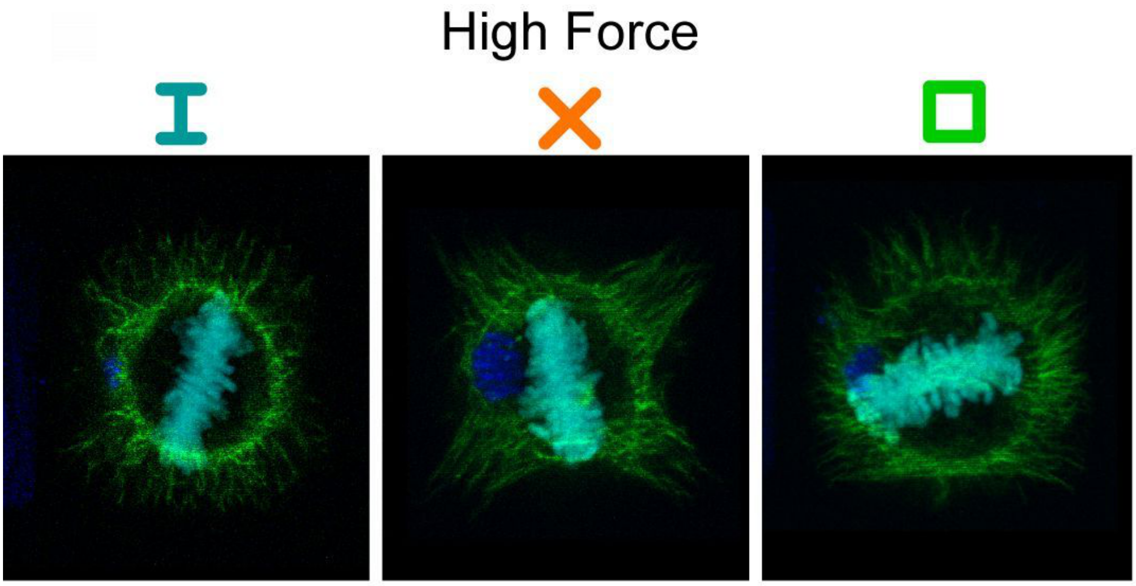

Figure 5.32: Bottom z-planes of cells under high mechanical stress, displaying the asymmetry of the assembly of the metaphase plate in addition to the retraction fibers. For I and X shapes, the retraction fibers appear to orient properly with the cell membrane, while for the square shape, the length of the fibers on the nanoparticle edge appear shorter (and presumably not under tension) as compared to the other edges. This effect may restrict the force-biasing effect for square patterned cells as compared to the other shapes.

In addition to control capabilities, we believe such approaches can coax novel results about the nuances in single cell behavior, as a complex spatially stratified machine. The combination of patterning underlying biochemistry, and patterning transduction gives engineers the ability to control a large variety of parameters before experimental execution, in addition to simplifying experimental method.

CHAPTER 6

Discussion and Conclusion

Nanotechnology is poised to generate a bevy of tools to assist in both academic and everyday endeavors. The ability to control and generate tools at the scale of what is the fundamental components of many materials and objects presents engineers with a direct control of the properties of macro-structure. Among these, magnetic nanoparticles, capable of directly translating information generated from large-scale systems into molecular systems, are poised to give biologists and engineers access to an ever increasing toolbox.

In this dissertation we present a set of strategies that utilize the intracellular manipulation of magnetic nanoparticles in an attempt to dynamically localize cellular cues. In total we demonstrate:

1) Periodic magnetic dots as a strategy to dynamically and rapidly translate magnetic particles in intracellular space.

2) Manipulation of magnetic particles with submicron precision and less than 2 second response time.

3) Translation of magnetic particles across the cellular space through a ratcheting mechanism.

4) Alginment of patterned cells and micromagnets using a novel process and method.

5) Force-generating capability of greater than 100 nN of total force, 5 nN / μm, and 2.5 nN / μm^2.

6) Force-mediated generation of active (myosin-X positive) filopodia.

7) Force-mediated polarity and activation of localized biochemistry (phosphorylated P21-activated kinase).

8) Force-mediated biasing of the metaphase plate during cellular mitosis.

9) Dynamic generation of biological cues (force).

We believe such approaches, whereby particle content is polarized in the single cell environment, holds potential as a method for both single cells analysis and control. More generally, once approaches to release nanoparticles from endosomes are implemented, the technique provides a platform to dynamically apply a range of localized stimuli arbitrarily within cells. Through the bioconjugation of proteins, nucleic acids, small molecules, or whole organelles a broad range of questions should be accessible concerning molecular localization and its importance in cell function.

References

[1] C. Schmidt, M. Mayer, and H. Vogel. A chip-based biosensor for the functional analysis of single ion channels. *Angewandte Chemie*, 112(17):3267–3270, 2000.

[2] A. Han, E. Moss, R.D. Rabbitt, K.L. Engisch, and A.B. Frazier. A single cell multi-analysis system for electrophysiological studies. In *TRANSDUCERS, Solid-State Sensors, Actuators and Microsystems, 12th International Conference on, 2003*, volume 1, pages 674–677. IEEE, 2003.

[3] NR Tas, JW Berenschot, P. Mela, HV Jansen, M. Elwenspoek, and A. Van den Berg. 2d-confined nanochannels fabricated by conventional micromachining. *Nano Letters*, 2(9):1031–1032, 2002.

[4] A. Karlsson, R. Karlsson, M. Karlsson, A.S. Cans, A. Strömberg, F. Ryttsén, and O. Orwar. Molecular engineering: networks of nanotubes and containers. *Nature*, 409(6817):150–152, 2001.

[5] NR Tas, JW Berenschot, TSJ Lammerink, M. Elwenspoek, and A. Van den Berg. Nanofluidic bubble pump using surface tension directed gas injection. *Analytical chemistry*, 74(9):2224–2227, 2002.

[6] J. Voldman, M.L. Gray, M. Toner, and M.A. Schmidt. A microfabrication-based dynamic array cytometer. *Analytical chemistry*, 74(16):3984–3990, 2002.

[7] H. Andersson and A. Van den Berg. Microfluidic devices for cellomics: a review. *Sensors and Actuators B: Chemical*, 92(3):315–325, 2003.

[8] T. Lehnert, MAM Gijs, R. Netzer, and U. Bischoff. Realization of hollow sio micronozzles for electrical measurements on living cells. *Applied physics letters*, 81:5063, 2002.

[9] F. Arai, A. Ichikawa, M. Ogawa, T. Fukuda, K. Horio, and K. Itoigawa. High-speed separation system of randomly suspended single living cells by laser trap and dielectrophoresis. *Electrophoresis*, 22(2):283–288, 2001.

[10] C. Reichle, K. Sparbier, T. Müller, T. Schnelle, P. Walden, and G. Fuhr. Combined laser tweezers and dielectric field cage for the analysis of receptor-ligand interactions on single cells. *Electrophoresis*, 22(2):272–282, 2001.

[11] J. Do, J.W. Choi, and C.H. Ahn. Low-cost magnetic interdigitated array on a plastic wafer. *Magnetics, IEEE Transactions on*, 40(4):3009–3011, 2004.

[12] M. Zborowski, L. Sun, L.R. Moore, P. Stephen Williams, and J.J. Chalmers. Continuous cell separation using novel magnetic quadrupole flow sorter. *Journal of Magnetism and Magnetic Materials*, 194(1):224–230, 1999.

[13] H. Lee, AM Purdon, and RM Westervelt. Manipulation of biological cells using a microelectromagnet matrix. *Applied Physics Letters*, 85:1063, 2004.

[14] Q. Ramadan, C. Yu, V. Samper, and D.P. Poenar. Microcoils for transport of magnetic beads. *Applied physics letters*, 88:032501, 2006.

[15] C.H. Ahn, M.G. Allen, W. Trimmer, Y.N. Jun, and S. Erramilli. A fully integrated micromachined magnetic particle separator. *Microelectromechanical Systems, Journal of*, 5(3):151–158, 1996.

[16] R.J. Mannix, S. Kumar, F. Cassiola, M. Montoya-Zavala, E. Feinstein, M. Prentiss, and D.E. Ingber. Nanomagnetic actuation of receptor-mediated signal transduction. *Nature nanotechnology*, 3(1):36–40, 2007.

[17] J. Dobson. Remote control of cellular behaviour with magnetic nanoparticles. *Nature Nanotechnology*, 3(3):139–143, 2008.

[18] A.H.B. De Vries, B.E. Krenn, R. Van Driel, and J.S. Kanger. Micro magnetic tweezers for nanomanipulation inside live cells. *Biophysical journal*, 88(3):2137–2144, 2005.

[19] J. Gao, W. Zhang, P. Huang, B. Zhang, X. Zhang, and B. Xu. Intracellular spatial control of fluorescent magnetic nanoparticles. *Journal of the American Chemical Society*, 130(12):3710–3711, 2008.

[20] H. Andersson and A. van den Berg. Microtechnologies and nanotechnologies for single-cell analysis. *Current opinion in biotechnology*, 15(1):44–49, 2004.

[21] B.P. Helmke and A.R. Minerick. Designing a nano-interface in a microfluidic chip to probe living cells: Challenges and perspectives. *Proceedings of the National Academy of Sciences*, 103(17):6419–6424, 2006.

[22] I. Obataya, C. Nakamura, S.W. Han, N. Nakamura, and J. Miyake. Nanoscale operation of a living cell using an atomic force microscope with a nanoneedle. *Nano letters*, 5(1):27–30, 2005.

[23] Y. Luo, H. Liu, Q. Rui, and Y. Tian. Detection of extracellular h2o2 released from human liver cancer cells based on tio2 nanoneedles with enhanced electron transfer of cytochrome c. *Analytical chemistry*, 81(8):3035–3041, 2009.

[24] S.W. Han, C. Nakamura, N. Kotobuki, I. Obataya, H. Ohgushi, T. Nagamune, and J. Miyake. High-efficiency dna injection into a single human mesenchymal stem cell using a nanoneedle and atomic force microscopy. *Nanomedicine: Nanotechnology, Biology and Medicine*, 4(3):215–225, 2008.

[25] X. Chen, A. Kis, A. Zettl, and C.R. Bertozzi. A cell nanoinjector based on carbon nanotubes. *Proceedings of the National Academy of Sciences*, 104(20):8218, 2007.

[26] M. Huse, L.O. Klein, A.T. Girvin, J.M. Faraj, Q.J. Li, M.S. Kuhns, and M.M. Davis. Spatial and temporal dynamics of t cell receptor signaling with a photoactivatable agonist. *Immunity*, 27(1):76–88, 2007.

[27] Y. Qiu and K. Park. Environment-sensitive hydrogels for drug delivery. *Advanced drug delivery reviews*, 53(3):321–339, 2001.

[28] P. Gupta, K. Vermani, and S. Garg. Hydrogels: from controlled release to ph-responsive drug delivery. *Drug discovery today*, 7(10):569–579, 2002.

[29] T.R. Hoare and D.S. Kohane. Hydrogels in drug delivery: Progress and challenges. *Polymer*, 49(8):1993–2007, 2008.

[30] A.M. Kloxin, A.M. Kasko, C.N. Salinas, and K.S. Anseth. Photodegradable hydrogels for dynamic tuning of physical and chemical properties. *Science*, 324(5923):59–63, 2009.

[31] E.K. Moioli, P.A. Clark, X. Xin, S. Lal, and J.J. Mao. Matrices and scaffolds for drug delivery in dental, oral and craniofacial tissue engineering. *Advanced drug delivery reviews*, 59(4-5):308–324, 2007.

[32] J.K. Tessmar and A.M. Göpferich. Matrices and scaffolds for protein delivery in tissue engineering. *Advanced drug delivery reviews*, 59(4-5):274–291, 2007.

[33] S. Funamoto, R. Meili, S. Lee, L. Parry, and R.A. Firtel. Spatial and temporal regulation of 3-phosphoinositides by pi 3-kinase and pten mediates chemotaxis. *Cell*, 109(5):611–623, 2002.

[34] E. Tzima, M.A. Del Pozo, S.J. Shattil, S. Chien, and M.A. Schwartz. Activation of integrins in endothelial cells by fluid shear stress mediates rho-dependent cytoskeletal alignment. *The EMBO journal*, 20(17):4639–4647, 2001.

[35] S. Chien. Mechanotransduction and endothelial cell homeostasis: the wisdom of the cell. *American Journal of Physiology-Heart and Circulatory Physiology*, 292(3):H1209–H1224, 2007.

[36] S.R.L. Young, R. Gerard-O'Riley, J.B. Kim, and F.M. Pavalko. Focal adhesion kinase is important for fluid shear stress-induced mechanotransduction in osteoblasts. *Journal of bone and mineral research*, 24(3):411–424, 2009.

[37] J.H.C. Wang, P. Goldschmidt-Clermont, J. Wille, and F.C.P. Yin. Specificity of endothelial cell reorientation in response to cyclic mechanical stretching. *Journal of Biomechanics*, 34(12):1563–1572, 2001.

[38] A.O. Duty, M.E. Oest, R.E. Guldberg, et al. Cyclic mechanical compression increases mineralization of cell-seeded polymer scaffolds in vivo. *Journal of biomechanical engineering*, 129:531, 2007.

[39] D.E. Discher, P. Janmey, and Y. Wang. Tissue cells feel and respond to the stiffness of their substrate. *Science*, 310(5751):1139–1143, 2005.

[40] B.C. Heng, H.K. Haider, E.K.W. Sim, T. Cao, and S.C. Ng. Strategies for directing the differentiation of stem cells into the cardiomyogenic lineage in vitro. *Cardiovascular research*, 62(1):34–42, 2004.

[41] X. Hu, P.H. Bessette, J. Qian, C.D. Meinhart, P.S. Daugherty, and H.T. Soh. Marker-specific sorting of rare cells using dielectrophoresis. *Proceedings of the National Academy of Sciences of the United States of America*, 102(44):15757, 2005.

[42] J. Voldman. Electrical forces for microscale cell manipulation. *Annu. Rev. Biomed. Eng.*, 8:425–454, 2006.

[43] T. Schnelle, T. Müller, G. Gradl, SG Shirley, and G. Fuhr. Paired microelectrode system: dielectrophoretic particle sorting and force calibration. *Journal of Electrostatics*, 47(3):121–132, 1999.

[44] K.C. Neuman and S.M. Block. Optical trapping. *Review of scientific instruments*, 75:2787, 2004.

[45] JP Mills, L. Qie, M. Dao, CT Lim, and S. Suresh. Nonlinear elastic and viscoelastic deformation of the human red blood cell with optical tweezers. *MCB-TECH SCIENCE PRESS-*, 1:169–180, 2004.

[46] R.M. Hochmuth. Micropipette aspiration of living cells. *Journal of biomechanics*, 33(1):15–22, 2000.

[47] W.R. Jones, H. Ping Ting-Beall, G.M. Lee, S.S. Kelley, R.M. Hochmuth, and F. Guilak. Alterations in the youngs modulus and volumetric properties of chondrocytes isolated from normal and osteoarthritic human cartilage. *Journal of biomechanics*, 32(2):119–127, 1999.

[48] QS Li, GYH Lee, CN Ong, and CT Lim. Afm indentation study of breast cancer cells. *Biochemical and biophysical research communications*, 374(4):609–613, 2008.

[49] S. Sen, S. Subramanian, and D.E. Discher. Indentation and adhesive probing of a cell membrane with afm: theoretical model and experiments. *Biophysical journal*, 89(5):3203–3213, 2005.

[50] S.M. Mijailovich, M. Kojic, M. Zivkovic, B. Fabry, and J.J. Fredberg. A finite element model of cell deformation during magnetic bead twisting. *Journal of Applied Physiology*, 93(4):1429–1436, 2002.

[51] H. Huang, S. Delikanli, H. Zeng, D.M. Ferkey, and A. Pralle. Remote control of ion channels and neurons through magnetic-field heating of nanoparticles. *Nature nanotechnology*, 5(8):602–606, 2010.

[52] T.R. Polte, M. Shen, J. Karavitis, M. Montoya, J. Pendse, S. Xia, E. Mazur, and D.E. Ingber. Nanostructured magnetizable materials that switch cells between life and death. *Biomaterials*, 28(17):2783–2790, 2007.

[53] G. Li, V. Joshi, R.L. White, S.X. Wang, J.T. Kemp, C. Webb, R.W. Davis, and S. Sun. Detection of single micron-sized magnetic bead and magnetic nanoparticles using spin valve sensors for biological applications. *Journal of applied physics*, 93:7557, 2003.

[54] T. Thorsen, S.J. Maerkl, and S.R. Quake. Microfluidic large-scale integration. *Science*, 298(5593):580–584, 2002.

[55] S. Centi, S. Laschi, M. Fránek, and M. Mascini. A disposable immunomagnetic electrochemical sensor based on functionalised magnetic beads and carbon-based screen-printed electrodes (spces) for the detection of polychlorinated biphenyls (pcbs). *Analytica chimica acta*, 538(1):205–212, 2005.

[56] M. Strömberg, J. Göransson, K. Gunnarsson, M. Nilsson, P. Svedlindh, and M. Strømme. Sensitive molecular diagnostics using volume-amplified magnetic nanobeads. *Nano letters*, 8(3):816–821, 2008.

[57] Y. Lu, G.L. Liu, J. Kim, Y.X. Mejia, and L.P. Lee. Nanophotonic crescent moon structures with sharp edge for ultrasensitive biomolecular detection by local electromagnetic field enhancement effect. *Nano letters*, 5(1):119–124, 2005.

[58] A. Nomura, S. Shin, O.O. Mehdi, and J.M. Kauffmann. Preparation, characterization, and application of an enzyme-immobilized magnetic microreactor for flow injection analysis. *Analytical chemistry*, 76(18):5498–5502, 2004.

[59] M. Babincová, D. Leszczynska, P. Sourivong, P. Čičmanec, and P. Babinec. Superparamagnetic gel as a novel material for electromagnetically induced hyperthermia. *Journal of magnetism and magnetic materials*, 225(1):109–112, 2001.

[60] J.H. Park, G. von Maltzahn, L. Zhang, A.M. Derfus, D. Simberg, T.J. Harris, E. Ruoslahti, S.N. Bhatia, and M.J. Sailor. Systematic surface engineering of magnetic nanoworms for in vivo tumor targeting. *Small*, 5(6):694–700, 2009.

[61] G. Fonnum, C. Johansson, A. Molteberg, S. Mørup, and E. Aksnes. Characterisation of dynabeads¡ sup¿®¡/sup¿ by magnetization measurements and mössbauer spectroscopy. *Journal of magnetism and magnetic materials*, 293(1):41–47, 2005.

[62] E. Schäffer, S.F. Nørrelykke, and J. Howard. Surface forces and drag coefficients of microspheres near a plane surface measured with optical tweezers. *Langmuir*, 23(7):3654–3665, 2007.

[63] J.H. Pai, Y. Wang, G.T.A. Salazar, C.E. Sims, M. Bachman, GP Li, and N.L. Allbritton. Photoresist with low fluorescence for bioanalytical applications. *Analytical chemistry*, 79(22):8774–8780, 2007.

[64] E.A. Cowles, L.L. Brailey, and G.A. Gronowicz. Integrin-mediated signaling regulates ap-1 transcription factors and proliferation in osteoblasts. *Journal of biomedical materials research*, 52(4):725–737, 2000.

[65] D. Barberis, S. Artigiani, A. Casazza, S. Corso, S. Giordano, C.A. Love, EY Jones, PM Comoglio, and L. TAMAGNONE. Plexin signaling hampers integrin-based adhesion, leading to rho-kinase independent cell rounding, and inhibiting lamellipodia extension and cell motility. *The FASEB journal*, 18(3):592–594, 2004.

[66] N.P. Huang, R. Michel, J. Voros, M. Textor, R. Hofer, A. Rossi, D.L. Elbert, J.A. Hubbell, and N.D. Spencer. Poly (l-lysine)-g-poly (ethylene glycol) layers on metal oxide surfaces: surface-analytical characterization and resistance to serum and fibrinogen adsorption. *Langmuir*, 17(2):489–498, 2001.

[67] P.K. Mattila and P. Lappalainen. Filopodia: molecular architecture and cellular functions. *Nature Reviews Molecular Cell Biology*, 9(6):446–454, 2008.

[68] G.T. Charras and M.A. Horton. Single cell mechanotransduction and its modulation analyzed by atomic force microscope indentation. *Biophysical journal*, 82(6):2970–2981, 2002.

[69] C. Wei, X. Wang, M. Chen, K. Ouyang, L.S. Song, and H. Cheng. Calcium flickers steer cell migration. *Nature*, 457(7231):901–905, 2008.

[70] V. Vasioukhin, C. Bauer, M. Yin, and E. Fuchs. Directed actin polymerization is the driving force for epithelial cell–cell adhesion. *Cell*, 100(2):209–219, 2000.

[71] BJ Nolen, N. Tomasevic, A. Russell, DW Pierce, Z. Jia, CD McCormick, J. Hartman, R. Sakowicz, and TD Pollard. Characterization of two classes of small molecule inhibitors of arp2/3 complex. *Nature*, 460(7258):1031–1034, 2009.

[72] A. Steffen, J. Faix, G.P. Resch, J. Linkner, J. Wehland, J.V. Small, K. Rottner, and T.E.B. Stradal. Filopodia formation in the absence of functional wave-and arp2/3-complexes. *Molecular biology of the cell*, 17(6):2581–2591, 2006.

[73] E.A. Papakonstanti and C. Stournaras. Association of pi-3 kinase with pak1 leads to actin phosphorylation and cytoskeletal reorganization. *Molecular biology of the cell*, 13(8):2946–2962, 2002.

[74] S. Dharmawardhane, D. Brownson, M. Lennartz, and G.M. Bokoch. Localization of p21-activated kinase 1 (pak1) to pseudopodia, membrane ruffles, and phagocytic cups in activated human neutrophils. *Journal of leukocyte biology*, 66(3):521–527, 1999.

[75] N. Azuma, N. Akasaka, H. Kito, M. Ikeda, V. Gahtan, T. Sasajima, and B.E. Sumpio. Role of p38 map kinase in endothelial cell alignment induced by fluid shear stress. *American Journal of Physiology-Heart and Circulatory Physiology*, 280(1):H189–H197, 2001.

[76] E. Robles, S. Woo, and T.M. Gomez. Src-dependent tyrosine phosphorylation at the tips of growth cone filopodia promotes extension. *The Journal of neuroscience*, 25(33):7669–7681, 2005.

[77] C. Hahn and M.A. Schwartz. Mechanotransduction in vascular physiology and atherogenesis. *Nature Reviews Molecular Cell Biology*, 10(1):53–62, 2009.

[78] Y.C. Poh, S. Na, F. Chowdhury, M. Ouyang, Y. Wang, and N. Wang. Rapid activation of rac gtpase in living cells by force is independent of src. *PLoS One*, 4(11):e7886, 2009.

[79] E. Tzima, M.A. Del Pozo, W.B. Kiosses, S.A. Mohamed, S. Li, S. Chien, and M.A. Schwartz. Activation of rac1 by shear stress in endothelial cells mediates both cytoskeletal reorganization and effects on gene expression. *The EMBO journal*, 21(24):6791–6800, 2002.

[80] B. Wojciak-Stothard and A.J. Ridley. Shear stress–induced endothelial cell polarization is mediated by rho and rac but not cdc42 or pi 3-kinases. *The Journal of cell biology*, 161(2):429–439, 2003.

[81] H. Zhang, F. Landmann, H. Zahreddine, D. Rodriguez, M. Koch, and M. Labouesse. A tension-induced mechanotransduction pathway promotes epithelial morphogenesis. *Nature*, 471(7336):99–103, 2011.

[82] M.C. Parrini, J. Camonis, M. Matsuda, and J. de Gunzburg. Dissecting activation of the pak1 kinase at protrusions in living cells. *Journal of Biological Chemistry*, 284(36):24133–24143, 2009.

[83] V.D. Delorme-Walker, J.R. Peterson, J. Chernoff, C.M. Waterman, G. Danuser, C. Der-Mardirossian, and G.M. Bokoch. Pak1 regulates focal adhesion strength, myosin iia distribution, and actin dynamics to optimize cell migration. *The Journal of Cell Biology*, 193(7):1289–1303, 2011.

[84] T.H. Loo, Y.W. Ng, L. Lim, and E. Manser. Git1 activates p21-activated kinase through a mechanism independent of p21 binding. *Science's STKE*, 24(9):3849, 2004.

[85] K. Kaempchen, K. Mielke, T. Utermark, S. Langmesser, and C.O. Hanemann. Upregulation of the rac1/jnk signaling pathway in primary human schwannoma cells. *Human molecular genetics*, 12(11):1211–1221, 2003.

[86] S.W. Deacon, A. Beeser, J.A. Fukui, U.E.E. Rennefahrt, C. Myers, J. Chernoff, and J.R. Peterson. An isoform-selective, small-molecule inhibitor targets the autoregulatory mechanism of p21-activated kinase. *Chemistry & biology*, 15(4):322–331, 2008.

[87] J. Stastna, X. Pan, H. Wang, A. Kollmannsperger, S. Kutscheidt, V. Lohmann, R. Grosse, and O.T. Fackler. Differing and isoform-specific roles for the formin diaph3 in plasma membrane blebbing and filopodia formation. *Cell Research*, 2011.

[88] G. Livshits, A. Kobielak, and E. Fuchs. Governing epidermal homeostasis by coupling cell–cell adhesion to integrin and growth factor signaling, proliferation, and apoptosis. *Proceedings of the National Academy of Sciences*, 109(13):4886–4891, 2012.

[89] K.M. Eisenmann, E.S. Harris, S.M. Kitchen, H.A. Holman, H.N. Higgs, and A.S. Alberts. Dia-interacting protein modulates formin-mediated actin assembly at the cell cortex. *Current Biology*, 17(7):579–591, 2007.

[90] M. Théry, V. Racine, A. Pépin, M. Piel, Y. Chen, J.B. Sibarita, and M. Bornens. The extracellular matrix guides the orientation of the cell division axis. *Nature cell biology*, 7(10):947–953, 2005.

[91] M. Théry and M. Bornens. Cell shape and cell division. *Current opinion in cell biology*, 18(6):648–657, 2006.

[92] M. Théry, A. Jiménez-Dalmaroni, V. Racine, M. Bornens, and F. Jülicher. Experimental and theoretical study of mitotic spindle orientation. *Nature*, 447(7143):493–496, 2007.